Atmospheric / Topographic Correction for Satellite Imagery

(ATCOR-2/3, Version 9.1.1, February 2017)

Theoretical Background Document

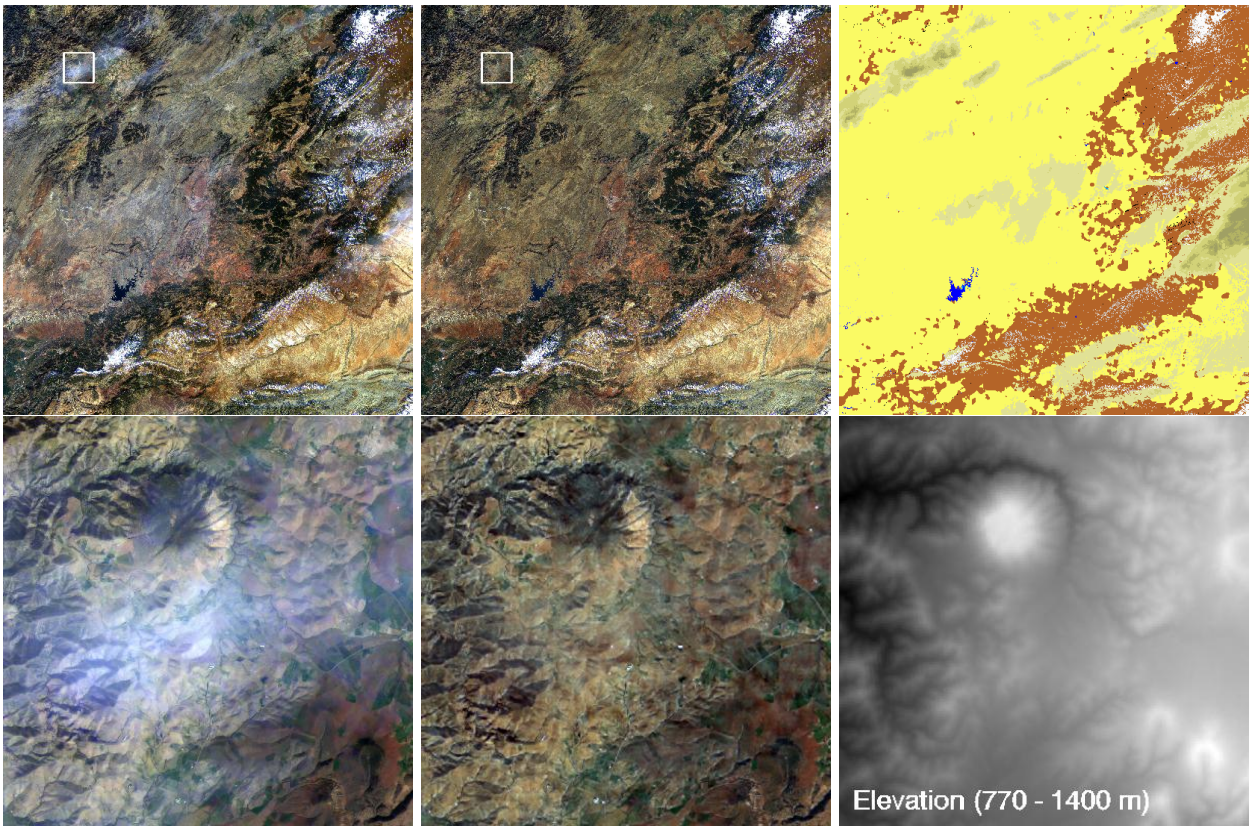

R. Richter[1] and D. Schläpfer[2]
[1] DLR - German Aerospace Center, D - 82234 Wessling, Germany
[2]ReSe Applications, Langeggweg 3, CH-9500 Wil SG, Switzerland
DLR-IB 565-01/2017

The contents of this document are taken from the 'Theoretical Background' and 'Value Added Products' chapters of the ATCOR User Guide.

The cover image shows a Sentinel-2 scene from Morocco, acquired March 15, 2016 (latitude=33.4°N, longitude=6.2°W, area 110 km x 110 km).
Top left to right: original scene (RGB = 665, 560, 443 nm), dehazed scene including cirrus removal, classification map.
Bottom left to right: subset (8 km x 8 km) of original scene, dehazed subset, digital elevation map (from the square area of the original scene).
The distinct hazy areas are due to cirrus clouds.
The yellow color in the classification map represents haze, darker yellow to green indicates cirrus, brown: clear, white: snow/ice.

ATCOR-2/3, Theoretical Background, February 2017

Authors:
R. Richter[1] and D. Schläpfer[2]
[1] DLR - German Aerospace Center, D - 82234 Wessling , Germany
[2] ReSe Applications, Langeggweg 3, CH-9500 Wil SG, Switzerland

Distribution:
ReSe Applications Schläpfer
Langeggweg 3, CH-9500 Wil, Switzerland

Updates: see ATCOR reference page: www.atcor.com/?page_id=53

Contents

List of Figures

List of Tables

Chapter 1

Value Added Products

As a "by-product" of atmospheric correction a number of useful quantities can readily be calculated. The first group of value added products include vegetation indices (based on surface reflectance instead of at-sensor radiance), simple parametrizations of the leaf area index, and wavelength-integrated reflectance (albedo). The second group comprises quantities relevant for surface energy balance investigations which are a useful supplement for studies in landscape ecology and related fields, e.g., as input for regional modeling of evapotranspiration. These include global radiation on the ground, absorbed solar radiation, net radiation, and heat fluxes. Emphasis is put on simple models based on the reflectance / temperature cube derived during the atmospheric correction. No additional data (with the exception of air temperature) is taken into account. All value added products are written to a file with up to 11 bands. The file structure is band sequential. If the input file name is "example.bsq", the output reflectance file name is "example_atm.bsq", and the value added file name is "example_atm_flx.bsq", the 'flx' indicating the most important part of the calculation, i.e., the radiation and heat fluxes.

1.1 LAI, FPAR, Albedo

Many vegetation indices have been introduced in the literature. Only two are presented here, because these are often used for simple parametrizations of the leaf area index (LAI), the fraction of absorbed photosynthetically active radiation (FPAR), and surface energy fluxes (Baret and Guyot 1991, Choudury 1994). The normalized difference vegetation index (NDVI) is defined as

$$NDVI = \frac{\rho_{850} - \rho_{650}}{\rho_{850} + \rho_{650}} \tag{1.1}$$

where ρ_{650} and ρ_{850} are surface reflectance values in the red (650 nm) and NIR (850 nm) region, respectively. The soil-adjusted vegetation index (SAVI) is defined as (Huete 1988, Baret and Guyot 1991, with L=0.5) :

$$SAVI = \frac{(\rho_{850} - \rho_{650}) * 1.5}{(\rho_{850} + \rho_{650} + 0.5)} \tag{1.2}$$

The leaf area index (LAI) can often be approximated with an empirical three-parameter relationship employing a vegetation index (VI=SAVI or VI=NDVI)

$$VI = a_0 - a_1 \; exp(-a_2 \; LAI) \tag{1.3}$$

Solving for LAI we obtain

$$LAI = -\frac{1}{a_2}\ ln(\frac{a_0 - VI}{a_1}) \tag{1.4}$$

Sample sets of parameters are a_0=0.82, a_1=0.78, a_2=0.6 (cotton with varied soil types), a_0=0.68, a_1=0.50, a_2=0.55 (corn), and a_0=0.72, a_1=0.61, a_2=0.65 (soybean) with VI=SAVI (Choudury et al. 1994).
Note: Since it is difficult to take into account the parameters for different fields and different seasons it is suggested to use a fixed set of these three parameters for multitemporal studies. Then, the absolute values of LAI may not be correct, but the seasonal trend can be captured.

Plants absorb solar radiation mainly in the 0.4 - 0.7 μm region, also called PAR region (photosynthetically active radiation, ASRAR 1989). The absorbed photosynthetically active radiation is called APAR, and the fraction of absorbed photosynthetically active radiation is abbreviated as FPAR. These terms are associated with the green phytomass and crop productivity. A three-parameter model can be employed to approxiate APAR and FPAR (Asrar et al. 1984, Asrar 1989, Wiegand et al, 1990, 1991).

$$FPAR = C[1 - A\ exp(-B\ LAI)] \tag{1.5}$$

Typical values are C=1, A=1, B=0.4. Again, since it is difficult to account for the crop- and seasonal dependence of these parameters, a constant set may be used for multitemporal datasets to get the typical FPAR course as a function of time.

The wavelength-integrated surface reflectance (in a strict sense the *hemispherical - directional reflectance*) weighted with the global flux on the ground E_g is used as a substitute for the surface albedo (*bi-hemispherical reflectance*). It is calculated as :

$$a = \frac{\int_{0.3\mu m}^{2.5\mu m} \rho(\lambda) E_g(\lambda) d\lambda}{\int_{0.3\mu m}^{2.5\mu m} E_g(\lambda) d\lambda} \tag{1.6}$$

Since most satellite sensors cover only part of the 0.3 - 2.5 μm region the following assumptions are being made for extrapolation. Extrapolation for the 0.30-0.40 μm region:

- $\rho_{0.3-0.4\mu m} = 0.8\ \rho_{0.45-0.50\mu m}$, if blue a band (0.45-0.50 μm) exists.
- $\rho_{0.3-0.4\mu m} = 0.8\ \rho_{0.52-0.58\mu m}$, green band, no blue band available.

Extrapolation for the 0.40-0.45 μm region:

- $\rho_{0.4-0.45\mu m} = 0.9\ \rho_{0.45-0.50\mu m}$, if a blue band (0.45-0.50 μm) exists.
- $\rho_{0.4-0.52\mu m} = 0.9\ \rho_{0.52-0.58\mu m}$, green band, no blue band available.

The reflectance reduction factors in the blue part of the spectrum account for the decrease of surface reflection for most land covers (soils, vegetation). The extrapolation to longer wavelengths is computed as:

- If a 1.6 μm band exists

  - $\rho_{2.0-2.5\mu m} = 0.5\ \rho_{1.6\mu m}$, if $\rho_{850}/\rho_{650} > 3$ (vegetation)
  - $\rho_{2.0-2.5\mu m} = \ \rho_{1.6\mu m}$, else

- If no bands at 1.6 μm and 2.2 μm are available the contribution for these regions is estimated as :

  - $\rho_{1.5-1.8\mu m} = 0.50\ \rho_{0.85\mu m}$, if $\rho_{850}/\rho_{650} > 3$ (vegetation)
  - $\rho_{2.0-2.5\mu m} = 0.25\ \rho_{0.85\mu m}$, if $\rho_{850}/\rho_{650} > 3$
  - $\rho_{1.5-1.8\mu m} = \rho_{0.85\mu m}$, (else)
  - $\rho_{2.0-2.5\mu m} = \rho_{0.85\mu m}$, (else)

At least three bands in the green, red, and near-infrared are required to derive the albedo product. Wavelength gap regions are supplemented with interpolation. The contribution of the 2.5 - 3.0 μm spectral region can be neglected, since the atmosphere is almost completely opaque and absorbs all solar radiation. The output "_flx" file contains the channels SAVI, LAI, FPAR, and albedo coded as 16 bit integer with the following scale factors:

- SAVI: range 0-1000, scale factor 1000, e.g., scaled SAVI=500 corresponds to SAVI=0.5 .
- LAI : range 0-10,000, scale factor 1000, e.g., scaled LAI=5000 corresponds to LAI=5.0 .
- FPAR: range 0-1000, scale factor 1000, e.g., scaled FPAR=500 corresponds to FPAR=0.5 .
- Albedo: range 0-1000, scale factor 10, e.g., scaled albedo=500 corresponds to albedo=50% .

The next section presents a simplified treatment of the radiation and heat fluxes in the energy balance.

1.2 Surface energy balance

Surface energy balance is an essential part of climatology. The energy balance equation applicable to most land surfaces can be written as (Asrar 1989) :

$$R_n = G \ + \ H \ + \ LE \tag{1.7}$$

where, R_n is the net radiant energy absorbed by the surface. The net energy is dissipated by conduction into the ground (G), convection to the atmosphere (H) and available as latent heat of evaporation (LE). The amount of energy employed in photosynthesis in case of vegetated surfaces is usually small compared to the other terms. Therefore, it is neglected here.
The terms on the right hand side of equation (1.7) are called heat fluxes. The soil or ground heat flux (G) typically ranges from 10% to 50% of net radiation. Convection to the atmosphere is called sensible heat flux (H). It may warm or cool the surface depending on whether the air is warmer or cooler than the surface. The energy available to evaporate water from the surface (LE) is usually obtained as the residual to balance the net radiation with the dissipation terms. Net radiation is expressed as the sum of three radiation components:

$$R_n = R_{solar} \ + \ R_{atm} \ - \ R_{surface} \tag{1.8}$$

where R_{solar} is the absorbed shortwave solar radiation (0.3 - 3 μm, or 0.3 - 2.5 μm), R_{atm} is the longwave radiation (3 - 14 μm) emitted from the atmosphere toward the surface, and $R_{surface}$ is the longwave radiation emitted from the surface into the atmosphere. Downwelling radiation is

counted with a positive sign, the upwelling thermal surface radiation has a negative sign. The absorbed solar radiation can be calculated as :

$$R_{solar} = \int_{0.3\mu m}^{2.5\mu m} \{1 - \rho(\lambda)\}\ E_g(\lambda)\ d\lambda \tag{1.9}$$

where $\rho(\lambda)$ is the ground reflectance, $1-\rho(\lambda)$ is the absorbed fraction of radiation, and $E_g(\lambda)$ is the global radiation (direct and diffuse solar flux) on the ground. The numerical calculation of equation (1.9) is based on the same assumptions regarding the extrapolation of bands and interpolation of gap regions as discussed in chapter 1.1 dealing with the surface albedo. If the satellite imagery contains no thermal band(s) from which a map of ground temperature can be derived, then R_{solar} is the only surface energy component that can be evaluated. In case of flat terrain with spatially varying visibility conditions or rugged terrain imagery, a map of the global radiation is included as an additional value added channel.

$$E_g = \int_{0.3\mu m}^{2.5\mu m} E_g(\lambda)\ d\lambda \tag{1.10}$$

For flat terrain imagery with constant atmospheric conditions the global radiation is a scalar quantity and its value can be found in the "*log" file accompanying each output reflectance file. For rugged terrain imagery, the global radiation accounts for the slope/aspect orientation of a DEM surface element.

With thermal bands a ground temperature or at least a ground brightness temperature image can be derived. Then the emitted surface radiation is calculated as

$$R_{surface} = \epsilon_s\ \sigma\ T_s^4 \tag{1.11}$$

where ϵ_s is the surface emissivity, $\sigma = 5.669\ \times 10^{-8}\ Wm^{-2}K^{-4}$ is the Stefan-Boltzmann constant, and T_s is the kinetic surface temperature. For sensors with a single thermal band such as Landsat TM an assumption has to be make about the surface emissivity to obtain the surface temperature. Usually, ϵ_s is selected in the range 0.95 - 1, and the corresponding temperature is a brightness temperature. A choice of $\epsilon_s = 0.97$ or $\epsilon_s = 0.98$ is often used for spectral bands in the 10 - 12 μm region. It introduces an acceptable small temperature error of about 1-2°C for surfaces in the emissivity range 0.95 - 1. Examples are vegetated or partially vegetated fields ($\epsilon = 0.96 - 0.99$), agricultural soil ($\epsilon = 0.95 - 0.97$), water ($\epsilon = 0.98$), and asphalt / concrete ($\epsilon = 0.95 - 0.96$). Emissivities of various surfaces are documented in the literature (Buettner and Kern 1965, Wolfe and Zissis 1985, Sutherland 1986, Salisbury and D'Aria 1992).

The atmospheric longwave radiation R_{atm} emitted from the atmosphere toward the ground can be written as

$$R_{atm} = \epsilon_a\ \sigma\ T_a^4 \tag{1.12}$$

where ϵ_a is the air emissivity, and T_a is the air temperature at screen height (2 m above ground), sometimes 50 m above ground are recommended. For cloud-free conditions, Brutsaert's (1975) equation can be used to predict the effective air emissivity :

$$\epsilon_a = 1.24\ \{\frac{p_{wv}}{T_a}\}^{1/7} \tag{1.13}$$

Here, p_{wv} is the water vapor partial pressure (millibars = hPa), and T_a is the air temperature (K). Figure 1.1 shows p_{wv} as a function of air temperature for relative humidities of 20 - 100%. The partial pressure is computed as :

$$p_{wv} = RH\ e_s\ /\ 100 \tag{1.14}$$

where RH is the relative humidity in per cent, and e_s is the water vapor partial pressure in saturated air (Murray 1967) :

$$e_s(T_a) = e_{s0}\ exp\{\frac{a(T_a - 273.16)}{T_a - b}\} \tag{1.15}$$

The constants are $a = 17.26939$, $b = 35.86$, and $e_{s0} = e_s(273.16K) = 6.1078\ hPa$. An alternative to equation (1.13) is the following approximation (Idso and Jackson 1969) which does not explicitly include the water vapor and holds for average humidity conditions, compare Figure 1.2.

$$\epsilon_a = 1 - 0.261\ exp\{-7.77 \times 10^{-4}\ (273 - T_a)^2\} \tag{1.16}$$

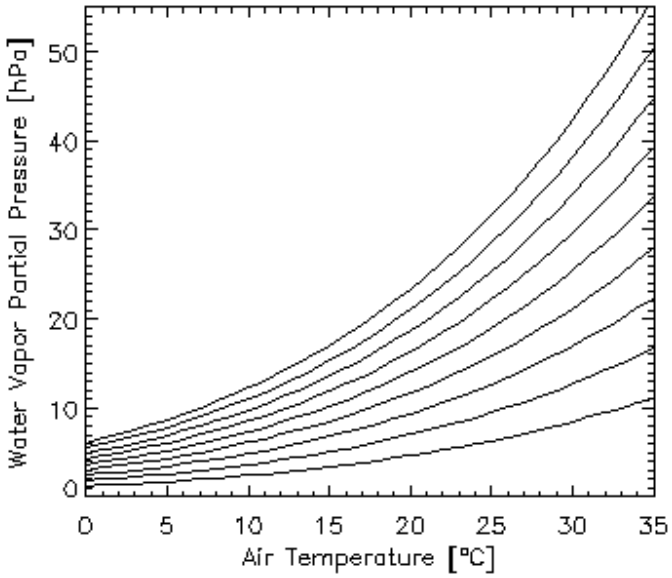

Figure 1.1: *Water vapor partial pressure as a function of air temperature and humidity. Relative humidities are 20% to 100% with a 10% increment, bottom to top curves, respectively (eq. 1.14).*

The calculation of the heat fluxes G, H, and LE on the right hand side of equation 1.7 requires different models for vegetated and man-made surfaces. For vegetated or partially vegetated surfaces, we employ a simple parametrization with the SAVI and scaled NDVI indices (Choudury 1994, Carlson et al. 1995) :

$$G = 0.4\ R_n\ (SAVI_m - SAVI)/SAVI_m \tag{1.17}$$

where $SAVI_m = 0.814$ represents full vegetation cover. The sensible heat flux is computed as :

$$H = B\ (T_s - T_a)^n \tag{1.18}$$

$$B = 286\ (0.0109 + 0.051\ NDVI^*) \tag{1.19}$$

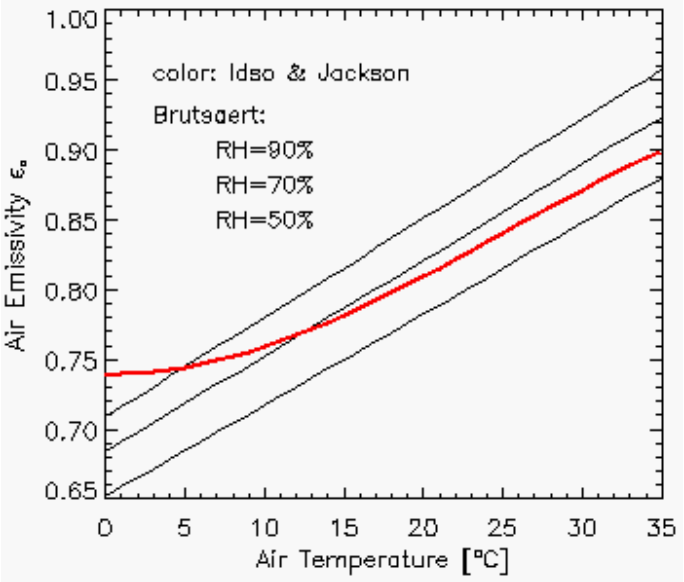

Figure 1.2: *Air emissivity after Brutsaert (eq. 1.13) and Idso/Jackson (eq. 1.16).*

$$n = 1.067 - 0.372\ NDVI^* \tag{1.20}$$

$$NDVI^* = \frac{\rho_{850} - \rho_{650}}{0.75 * (\rho_{850} - \rho_{650})} \tag{1.21}$$

Equation (1.18) corresponds to equation (1a) of Carlson et al. (1995), because G is neglected there, and so $R_n - G$ represents the energy left for evapotranspiration. The factor 286 in equation (1.19) converts the unit (cm/day) into (Wm^{-2}). $NDVI^*$ is the scaled NDVI ranging between 0 and 1, and truncated at 1 if necessary. Equation (1.21) corresponds to equation (3) of Carlson et al. (1995) with $NDVI_0 = 0$ (bare soil) and $NDVI_s = 0.75$ (full vegetation cover). The latent heat flux LE is computed as the residual:

$$LE = R_n\ -\ G\ -\ H \tag{1.22}$$

A different heat flux model is employed for urban areas with man-made surfaces (asphalt, concrete, roofs, etc.). These are defined here with the reflectance criteria

$$\rho_{650} \geq 0.10 \quad and \quad \rho_{850} \geq 0.10 \quad and \quad \rho_{650} > \rho_{850} * 0.7 \tag{1.23}$$

representing low vegetation indices with $NDVI < 0.176$. This simple spectral definition is not unambiguous, it might also apply to soils. For urban areas the latent heat is usually very small, and the fluxes G and H dominate. Therefore, the terms G, LE, and H are approximated by the following three equations (Parlow 1998):

$$G = 0.4\ R_n \tag{1.24}$$

$$LE = 0.15\ (R_n - G) \tag{1.25}$$

$$H = R_n\ -\ G -\ LE \tag{1.26}$$

For low vegetation indices ($SAVI < 0.1$) the ground heat flux G from equation (1.17), i.e., the vegetation model, agrees well with G from equation (1.24), i.e., the urban model. However, major

differences exist for the LE and H terms, see table 1.1. Parameters for this table are: $E_g = 800$, $R_n = 600$, $R_{atm} + R_{surface} = -100\ Wm^{-2}$, $T_s = 30°C$, and $T_a = 20°C$. The (veg) and (urb) indicate the heat fluxes derived from the vegetation and urban model, respectively. For the urban surfaces (asphalt, concrete) the G(veg), H(veg) and LE(veg) values are given in brackets for comparison, but the corresponding "urban" heat fluxes are valid because the "urban" criterion (equations 1.23, $\rho_{650} \geq 0.10$, $\rho_{850} \geq 0.10$, and $\rho_{650} > \rho_{850} * 0.7$) applies. The last row repeats the concrete case for $R_{solar} = 800 * (1 - 0.36) = 512, R_n = R_{solar} + R_{atm} + R_{surface} = 512 - 100 = 412\ Wm^{-2}$, a realistic reduced R_n value (compared to the asphalt where $E_g = 800, R_{solar} = 800 * (1 - 0.12) = 700, R_n = 700 - 100 = 600\ Wm^{-2}$).

surface	ρ_{650}	ρ_{850}	NDVI	G(veg)	H(veg)	LE(veg)	G(urb)	H(urb)	LE(urb)
full veget.	0.05	0.40	0.78	77	87	435	-	-	-
partial veget.	0.10	0.20	0.33	185	76	338	-	-	-
dark asphalt	0.11	0.13	0.09	(228)	(50)	(322)	240	306	54
bright concrete	0.35	0.40	0.07	(222)	(48)	(330)	240	306	54
bright concrete (*)	0.35	0.40	0.07	-	-	-	164	210	37

Table 1.1: *Heat fluxes for the vegetation and urban model. All fluxes in [Wm^{-2}].*

All radiation and heat fluxes are calculated in units of Wm^{-2}. They represent instantaneous flux values. For applications, where daily (24 h) LE values are required the following equation can be used for unit conversion:

$$LE\ [\frac{cm}{day}] = \frac{1}{286}\ LE\ [Wm^{-2}] \tag{1.27}$$

The latent heat flux LE is frequently called evapotranspiration (ET). Although LE and ET are used interchangeably the unit (cm/day) or (mm/day) is mostly employed for ET. For water surfaces the distribution of net radiation into G, LE, and H is difficult to determine, because it depends on several other parameters. Therefore, G and H are set to zero here, and so LE equals R_n.

Spatial maps (files) of air temperature and air emissivity can also be included in the processing. Usually, isolated point-like measurements of air temperature are available from meteorological stations. These have to be interpolated to generate a spatial map coregistered to the image prior to applying the ATCOR model. Data in the file containing the air temperature must have the Celsius unit, data of the air emissivity file must range between 0 and 1. Future improvements to the ATCOR model will include an air temperature map derived from the image ("triangle" or "trapezoidal" method employing the thermal band surface temperature and NDVI, Carlson et al. 1995; Moran et al. 1994).

In case of mountainous terrain, the air temperature $T_a(z_0)$ and water vapor partial pressure $p_{wv}(z_0)$ at a reference elevation z_0 have to be specified. The height dependence of air temperature is then obtained with linear extrapolation employing a user-specified adiabatic temperature gradient $\partial T/\partial z$:

$$T_a(z) = T_a(z_0)\ +\ \frac{\partial T}{\partial z}(z_0 - z) \tag{1.28}$$

where $\partial T/\partial z$ is typically in the range 0.65 - 0.9 (Celsius / 100 m). The water vapor partial pressure is extrapolated exponentially according to

$$p_{wv}(z) = p_{wv}(z_0)\ 10^{-(z-z_0)/z_s} \tag{1.29}$$

where z_s is the water vapor scale height (default 6.3 km). The list of all output channels of the value added *"*_flx.bsq"* file is :

1. Soil adjusted vegetation index (SAVI), scaled with factor 1000,
2. Leaf area index (LAI), scaled with 1000,
3. Fraction of photosynthetically active radiation FPAR, scaled with 1000,
4. Surface albedo (integrated reflectance from 0.3-2.5 μm), per cent * 10,
5. Absorbed solar radiation flux R_{solar} $[Wm^{-2}]$,
6. Global radiation E_g $[Wm^{-2}]$, omitted for constant visibility in flat terrain because it is a scalar which is put into the *"*log"* file .
   The next channels are only available in case of at least one thermal band:
7. Thermal air-surface flux difference $R_{therm} = R_{atm} - R_{surface}$ $[Wm^{-2}]$,
8. Ground heat flux G $[Wm^{-2}]$,
9. Sensible heat flux H $[Wm^{-2}]$,
10. Latent heat LE $[Wm^{-2}]$,
11. Net radiation R_n $[Wm^{-2}]$.

Chapter 2

Theoretical Background

Standard books on optical remote sensing contain an extensive presentation on sensors, spectral signatures, and atmospheric effects where the interested reader is referred to (Slater 1980 [95], Asrar 1989 [4], Schowengerdt 2007 [92]). This chapter contains a description of the concepts and equations employed for the atmospheric correction.
We start with the basic equations in the solar and thermal spectral region for clear sky conditions (standard case), then move on to non-standard conditions comprising bidirectional reflectance (BRDF) effects, hazy scenes, and a treatment of shadow areas caused by clouds or buildings. Standard atmospheric conditions include the option of a constant visibility (aerosol optical thickness) and water vapor content per scene, as well as the retrieval of a visibility and water vapor map if the required spectral bands are available for the specific sensor. Water vapor correction on a pixel-by-pixel basis is usually necessary for hyperspectral imagery.
The section on the non-standard conditions contains a short discussion on empirical correction methods for bidirectional effects. It continues with the description of a statistical haze removal method. The third section presents a technique to compensate shadow effects, i.e. cloud or building shadow areas are masked and de-shadowed. Then, an overview is presented of all major processing steps involved in the atmospheric correction.
After atmospheric correction, the surface reflectance cube can be used for classification. A simple automatic method is included here based on template reflectance spectra of different surface covers. Finally, the accuracy of the atmospheric correction is discussed.

Before going into details, a brief overview of the main processing steps during atmospheric correction is described in the next two flow charts. Figure 2.1 contains a compact summary of the main processing elements: after reading the sensor-specific LUTs a masking and preclassification is conducted to obtain land, water, haze, cloud, and shadow areas. Then an optional haze or cirrus removal is conducted followed by an optional shadow removal. The next step calculates the visibility or aerosol optical thickness map using the dense dark vegetation (DDV) method. This is followed by an update of the aerosol model (path radiance behavior in the blue to red bands) if a blue band exists and the update option (ratio_blu_red ¿ 0) is enabled. Otherwise the selected aerosol model is not changed. After calculation of the water vapor map the iterative surface reflectance retrieval is conducted accounting for adjacency and spherical albedo effects. After atmospheric correction, a spectral polishing (for hyperspectral instruments) and BRDF correction might be performed.
The visibility/ AOT(550 nm) retrieval flow chart describes the case with a SWIR band at 2.2 μm. It starts with a low reflectance threshold T1=0.05 and performs the masking in this SWIR band to obtain the darkest pixels, excluding water. If the number of reference pixels is less than 2% of the scene pixels then the threshold T1 is increased until threshold T2 = 0.12 is reached. If not

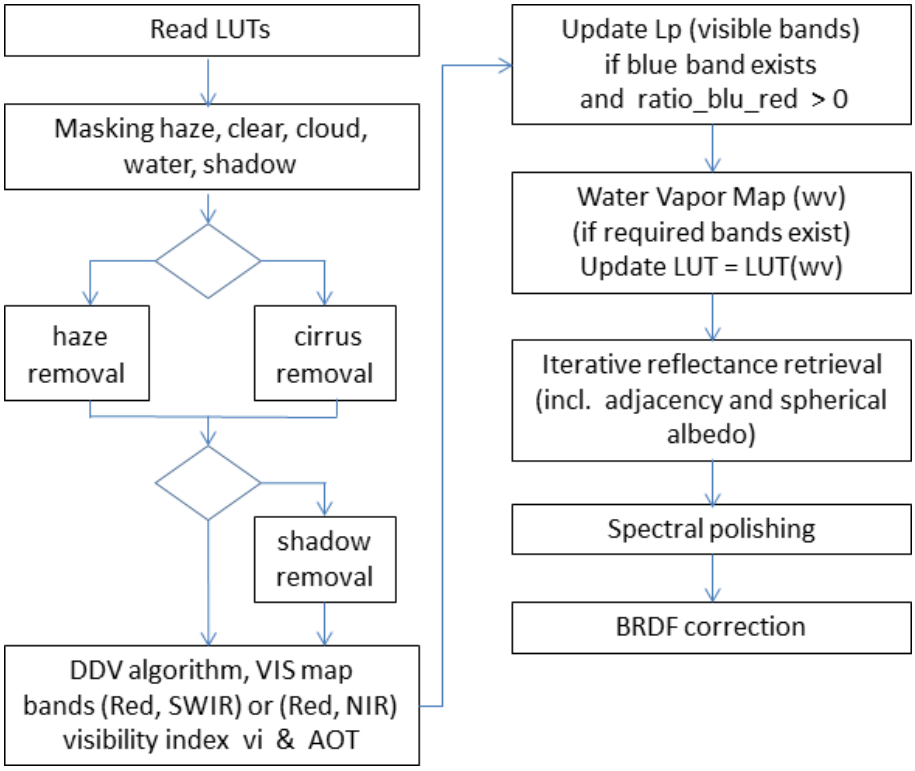

Figure 2.1: *Main processing steps during atmospheric correction.*

enough reference pixels are found then a constant VIS=23 km is used otherwise the visibility for each reference pixel is determined as the intersection of modeled and measured radiance in the red channel.
Then the NIR channel is checked concerning negative reflectance pixels (mainly water, shadow). If the percentage of negative reflectance pixels is higher tahn 1% of the scene pixels, then the visibility is iteratively increased up to 80 km. Finally, the visibility index and AOT(550nm) are calculated and the nn-reference pixels are assigned the average visibilty or optionally a spatial triangular interpolation can be performed. If the aerosol type (rural, urban, maritime, desert) is not fixed by the user, the flow chart is executed for these four types, and the type closest to the scene-estimated type is used, see chapter 2.5.2 for more details.

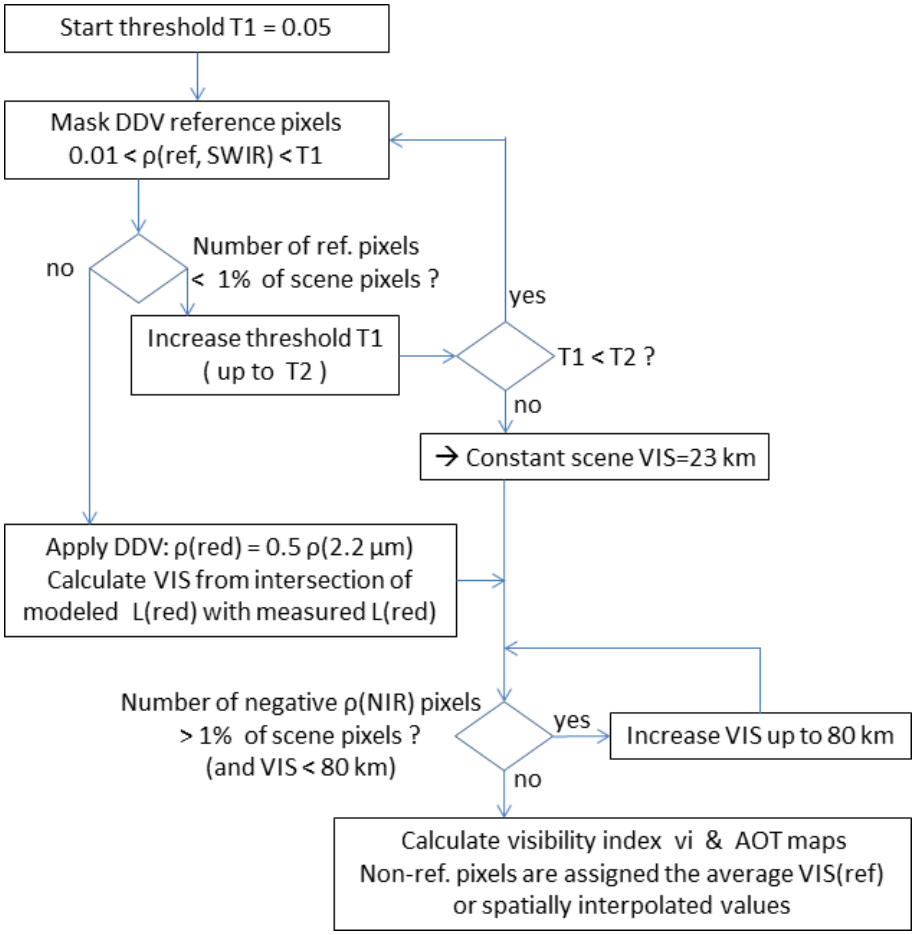

Figure 2.2: *Visibility / AOT retrieval using dark reference pixels.*

2.1 Basics on radiative transfer

This chapter presents the basic concepts and the terminology. The full set of equations is documented here as implemented in ATCOR. We start with the radiative transfer equation in the solar spectral region (0.4 - 2.5 μm) for a flat terrain under clear sky conditions. First, the equation for an infinite plane of uniform reflectance is presented. Then the case of a small uniform surface embedded in a large homogeneous background of different reflectance is discussed. We continue with the rugged terrain, and finally discuss the equations for the thermal spectral region (8-14 μm).

2.1.1 Solar spectral region

For a cloud-free sky and a uniform ground of reflectance ρ, the radiance signal received at the sensor consists of scattered solar radiation and ground reflected radiation. The scattered radiation component is also called path radiance. It depends on the solar and viewing geometry as sketched in Fig. 2.3. In case of a flat terrain, the at–sensor radiance L can be written as (Asrar 1989, chapter 9):

$$L = L_p(\Theta_v, \Theta_s, \phi) + \tau_v(\Theta_v)\frac{\rho}{\pi}\frac{E_g(0)}{1 - \rho_r s} \tag{2.1}$$

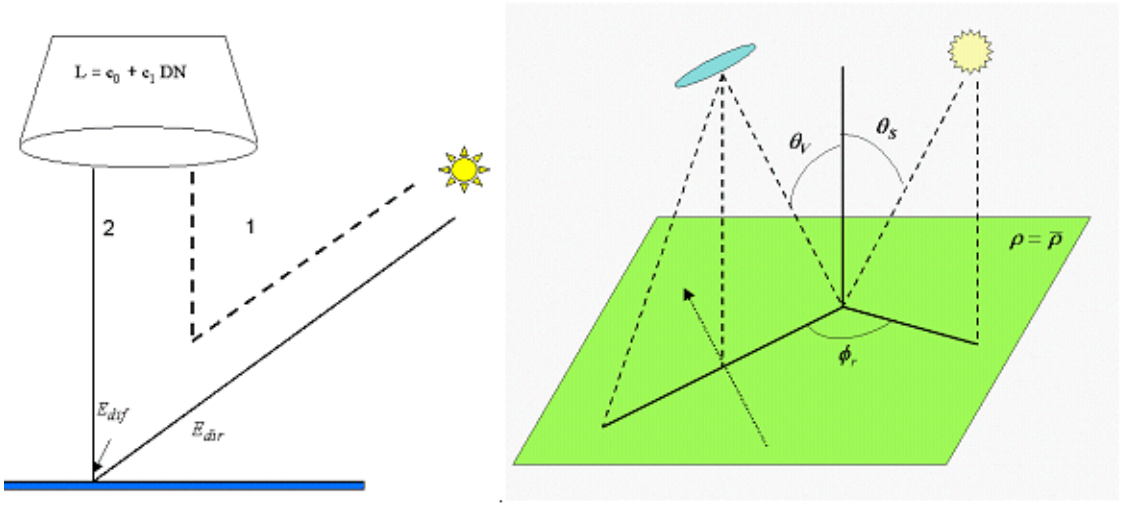

Figure 2.3: *Radiation components, illumination and viewing geometry.*

L	at-sensor radiance for surface reflectance ρ ;
L_p	path radiance ;
τ_v	total ground-to-sensor atmospheric transmittance, sum of direct τ_{dir} and diffuse τ_{dif} transmittance;
E_g	global flux on a horizontal surface, sum of direct (E_{dir}) and diffuse (E_{dif}) flux, $E_g(0)$ is calculated for a ground surface with $\rho = 0$;
ρ_r	large scale reference background reflectance determining the effective global flux (ρ_r=0.15 is used for ATCOR) ;
s	spherical albedo of the atmosphere, accounts for atmospheric backscattering to the ground.

The geometry is described by the angles Θ_v (view zenith), and Θ_s, ϕ (solar zenith and relative azimuth angles), compare figure 2.3. Since ρ and ρ_r are not known for image data and can vary within a scene, equation (2.1) has to be solved for ρ iteratively, compare equations (2.9 - 2.15).
In a strict sense, the reflectance ρ used here should be called *hemispherical-directional reflectance factor (HDRF)*, because most surfaces show an anisotropic reflectance behavior characterized by the bidirectional reflectance distribution function (BRDF, Nicodemus 1970, Slater, 1985). The ground is illuminated *hemispherically* by the direct and diffuse solar flux and the reflected radiation is recorded from a certain *direction*, i.e., *hemispherical* input radiation, *directional* reflected radiation. Since the reflected radiation is always measured in a small cone, the term *hemispherical-conical reflectance factor HCRF* is also used, but for small instantaneous field-of-view sensors, "directional" is a sufficiently accurate geometrical description. However, for simplicity we will use the abbreviation *reflectance* in this manual.

In spectral regions dominated by scattering effects, the terms of equation (2.1) are calculated with the scaled DISORT option (discrete ordinate radiative transfer [61]), in regions with strong

atmospheric absorption the more accurate correlated k algorithm is used in combination with DISORT [7]. The results are stored in look-up tables (LUT). Since MODTRAN calculates the path radiance including the diffuse reflected ground radiation in the form

$$L_{path}(\rho) = L_{path}(0) + \frac{\tau_{dif}\ E_g(0)\ \rho/\pi}{1-\rho s} = L_{path}(0) + \tau_{dif}\ E_g(\rho)\ \rho/\pi \tag{2.2}$$

two MODTRAN runs with surface reflectance $\rho = 0$ and $\rho_r = 0.15$ are required to calculate the diffuse ground-to-sensor transmittance τ_{dif} and spherical albedo s from equation (2.2)

$$\tau_{dif} = \frac{[L_{path}(\rho_r) - L_{path}(0)]\ \pi}{\rho_r\ E_g(\rho_r)} \tag{2.3}$$

$$E_g(\rho_r) = \frac{E_g(\rho = 0)}{1-\rho_r s} \tag{2.4}$$

$$s = [1 - \frac{E_g(0)}{E_g(\rho_r)}]/\rho_r \tag{2.5}$$

For image data, the pixel reflectance ρ may differ from the background reflectance $\bar{\rho}$. In this case the signal at the sensor consists of three components as sketched in Fig. 2.4:

- component 1: scattered radiance, path radiance,
- component 2: radiation reflected from pixel under consideration,
- component 3: radiation reflected from the neighborhood and scattered into the viewing direction ("adjacency" effect).

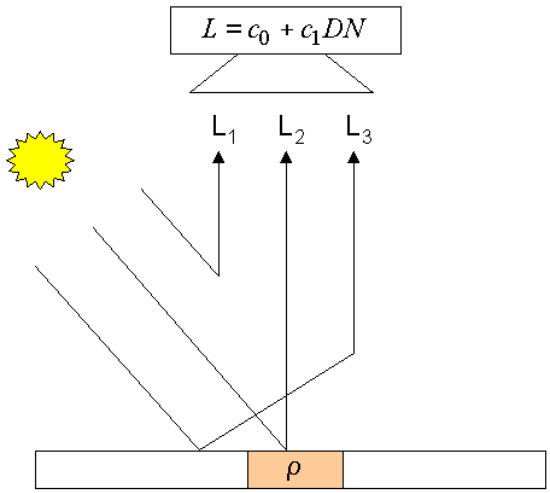

Figure 2.4: *Schematic sketch of solar radiation components in flat terrain.*

Only component 2 contains information on the surface properties of the pixel, the other components have to be removed during the atmospheric correction. As detailed in [75] the adjacency radiation L_3 consists of two components (atmospheric backscattering and volume scattering) which are combined into one component in Fig. 2.4.

The radiometric calibration assigns to each digital number (DN) the corresponding at-sensor radiance L

$$L(k) = c_0(k) + c_1(k)DN(k) \tag{2.6}$$

where k indicates the channel number, and c_0 , c_1 are the calibration coefficients (offset and slope). For sensors with adjustable gain settings the equation is

$$L(k) = c_0(k) + c_1(k)DN(k)/g(k) \tag{2.7}$$

where $g(k)$ is the gain setting in channel k. The atmospheric correction has to be performed iteratively, since the surface reflectance and large-scale (0.5-1 km neighborhood) background reflectance are not known. So three steps are employed in the ground reflectance calculation:
Step 1: The influence of the neighborhood (adjacency effect) is neglected and the surface reflectance is obtained from

$$\rho^{(1)} = \frac{\pi[d^2(c_0 + c_1 DN) - L_p]}{\tau_v E_g(\rho_r = 0.15)} \tag{2.8}$$

where the spectral band index is omitted for clarity. The factor d^2 takes into account the sun-to-earth distance (d is in astronomical units) since the LUTs with path radiance and global flux are calculated for d=1 in ATCOR.
Step 2: The second step calculates the average reflectance in a large neigborhood of each pixel (range R=0.5-1 km)

$$\bar{\rho} = \frac{1}{N^2} \sum_{i,j=1}^{N} \rho_{i,j}^{(1)} \tag{2.9}$$

where N corresponds to the number of pixels for the selected range R of the adjacency effect [68], [75]. The exact choice of R is not critical since the adjacency influence is a second-order effect. Instead of the range-independent weighting in eq. (2.9), a range-dependent function can be selected with an exponential decrease of the weighting coefficients [69]. The range-dependent case requires more execution time, of course. Except for special geometries, the difference between both approaches is small, because the average reflectance in a large neighborhood usually does not vary much and the influence is a second-order effect.

$$\rho^{(2)}(x,y) = \rho^{(1)}(x,y) + q\{\rho^{(1)} - \bar{\rho}(x,y)\} \tag{2.10}$$

The function q indicates the strength of the adjacency effect. It is the ratio of the diffuse to direct ground-to-sensor transmittance. The range-dependent version of eq. (2.10) is:

$$\rho^{(2)}(x,y) = \rho^{(1)}(x,y) + q\{\rho^{(1)}(x,y) - \int_0^R \rho^{(1)}(r)A(r)exp(-r/r_s)dr\} \tag{2.11}$$

Here, R is the range where the intensity of the adjacency effect has dropped to the 10% level (i.e. r=R=2.3x r_s, where r_s is a scale range, typically r_s=0.2-0.4 km, R=0.5-1 km), ρ(r) is the reflectance at range r from the (x,y) position and A(r) is the area of a circular zone from r to r+dr. Now we approximate the circular regions by square regions to obtain the discrete version of eq. (2.11) with exponentially decreasing weighting coefficients w_i:

$$\rho^{(2)}(x,y) = \rho^{(1)}(x,y) + q\{\rho^{(1)}(x,y) - \sum_{i=1}^{n_R} \bar{\rho}_i w_i\} \tag{2.12}$$

$$w_i = \frac{1}{\sum_{i=1}^{n_R} W_i} W_i \qquad and \qquad W_i = \int_{r_{i-1}}^{r_i} A(r) exp(-r) dr \approx \int_{r_{i-1}}^{r_i} (2r)^2 exp(-r) dr \tag{2.13}$$

ATCOR supports up to n_R=5 regions. Since the sequence of moving digital low pass filters works with square filters of size $2r_i$ * $2r_i$, the area A(r) is approximated as the corresponding square region $A(r) = (2r)^2$.
Step 3: it includes the spherical albedo effect on the global flux that was initially calculated with the reference background reflectance $\rho_r = 0.15$ and is finally adapted to the scene-dependent value $\bar{\rho}$ by correcting with the difference $\bar{\rho} - \rho_r$:

$$\rho^{(3)}(x, y) = \rho^{(2)}(x, y)[1 - (\bar{\rho}(x, y) - \rho_r)s] \tag{2.14}$$

Radiation components in rugged terrain :

Figure 2.5 shows a sketch of the radiation components in a rugged terrain [69]. Compared to the flat terrain one additional component is taken into account in the ATCOR model. It is an approximation of the terrain reflected radiation. It is obtained by weighting the reflected radiation in a 0.5 km surrounding of a pixel with the terrain view factor. The terrain view factor is $V_{terrain}(x, y) = 1 - V_{sky}(x, y)$, and the sky view factor $V_{sky}(x, y)$ is calculated from the DEM as explained below. The sky view factor is normalized to 1 for a flat terrain.
The reflectance is calculated iteratively. The first step neglects the adjacency effect and starts with a fixed terrain reflectance of $\bar{\rho}^{(0)}_{terrain} = 0.1$ [72] :

$$\rho^{(i)}(x, y) = \frac{\pi\ [d^2(c_0 + c_1 DN(x, y)) - L_p(z, \Theta_v, \phi)]}{\tau_v(z, \Theta_v)[b(x, y)E_s\tau_s(z)cos\beta(x, y) + E^*_d(x, y, z) + E^{i)}_t(z, \rho_r)\bar{\rho}^{(i-1)}_{terrain}V_{terrain}(x, y)]} \tag{2.15}$$

The terms are defined as :

x, y	horizontal coordinates, corresponding to the georeferenced pixel positions;
z	vertical coordinate, containing the elevation information from the DEM;
DN(x,y)	digital number of georeferenced pixel;
$L_p(z, \theta_v, \phi)$	path radiance, dependent on elevation and viewing geometry;
$\tau_v(z, \Theta_v)$	ground-to-sensor view angle transmittance, direct plus diffuse components;
$\tau_s(z)$	Sun-to-ground beam (direct) transmittance;
$\beta(x, y)$	angle between the solar ray and the surface normal (illumination angle);
b(x,y)	binary factor: b=1 if pixel receives direct solar beam, otherwise b=0;
E_s	extraterrestrial solar irradiance (earth-sun distance d=1 astronomical unit);
$E^*_d(x, y, z)$	diffuse solar flux on an inclined plane (see equation 2.18);
$E_g(z)$	global flux (direct plus diffuse solar flux on a horizontal surf. at elevation z);
$E_t(z)$	radiation incident upon adjacent slopes;
$\rho^{(0)}_{terrain}$	= 0.1, initial value of average terrain reflectance;
$\bar{\rho}^{(i)}_{terrain}(x, y)$	locally varying average terrain reflectance, calculated iteratively (i=1,2,3);
$V_{terrain}(x, y)$	terrain view factor (range 0-1).

The solar and DEM geometry is shown in figure 2.6 as well as the three solar radiation components taken into account for rugged terrain: direct and circumsolar irradiance, and diffuse hemispherical sky flux. It can be shown that these three components are equivalent to the direct and diffuse solar flux components in flat terrain. In case of a shadow pixel the direct and circumsolar components

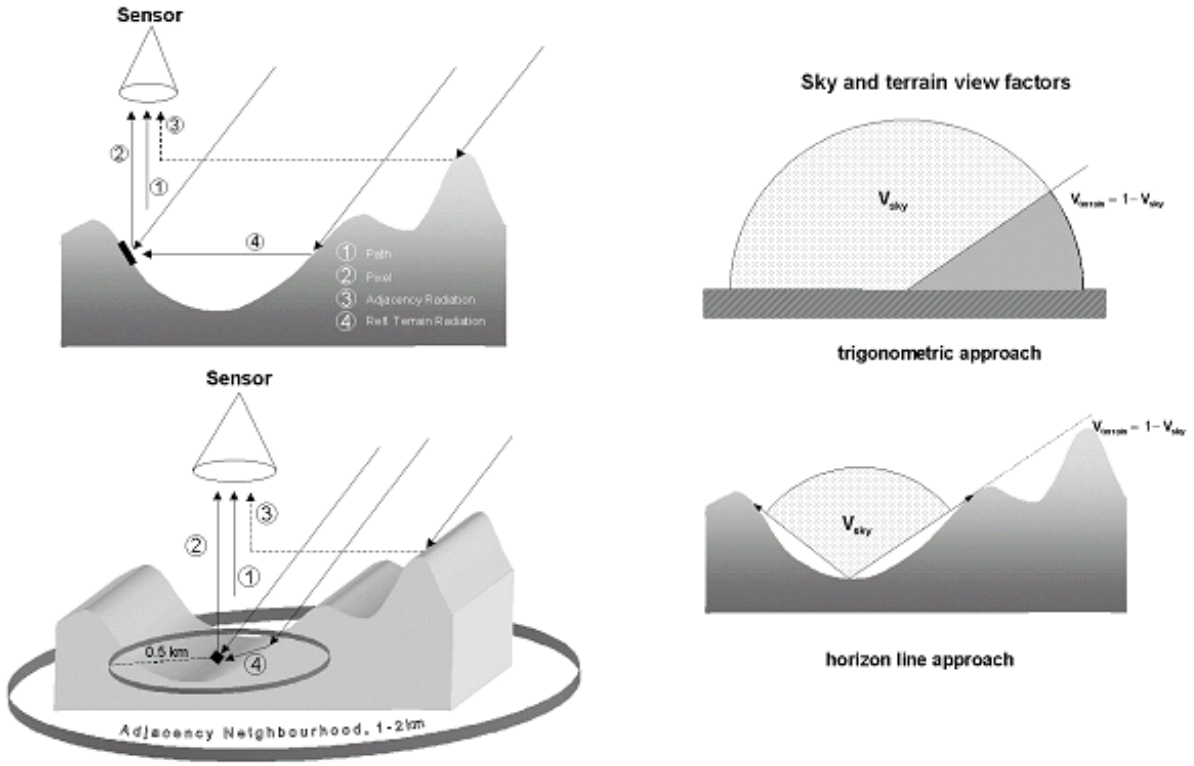

Figure 2.5: *Radiation components in rugged terrain, sky view factor.*
Left: schematic sketch of radiation components in rugged terrain; 1 : path radiance; 2 : pixel reflected radiance; 3 : adjacency radiance; 4 : reflected terrain radiance. Right: sky and terrain view factor.

are set to zero, i.e. the binary factor b=0.

The next step iterates eq. 2.15 averaging the reflected terrain radiation over a square box of 1.0 × 1.0 km. If equation (2.15) is used with $E_t = E_g$ then three iterations are usually sufficient to be independent of the start value of the terrain reflectance [69]. However, for highly reflective surfaces, e.g. snow, and high terrain view factors, more than three iterations are necessary, and a faster convergence of $\bar{\rho}^{(i)}_{terrain}$ can be achieved with a geometric series for the terrain reflected radiation E_t as proposed in [94] :

$$E_t^{(i)} = E_g \frac{\bar{\rho}^{(i-1)} V_{terrain}}{1 - \bar{\rho}^{(i-1)} \bar{V}_{terrain}} \tag{2.16}$$

The next steps include the adjacency correction (eq. 2.9, 2.10) and the spherical albedo effect (eq. 2.14).
If $\Theta_s, \Theta_n, \phi_s, \phi_n$ denote solar zenith angle, terrain slope, solar azimuth and topographic azimuth, respectively, the illumination angle β can be obtained from the DEM slope and aspect angles and the solar geometry:

$$cos\beta(x,y) = cos\Theta_s cos\Theta_n(x,y) + sin\Theta_s sin\Theta_n(x,y) cos\{\phi_s - \phi_n(x,y)\} \tag{2.17}$$

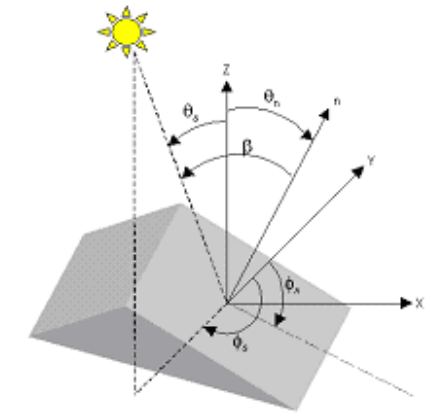

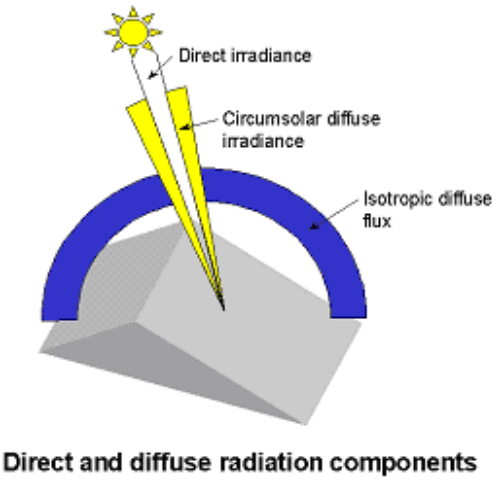

Figure 2.6: *Solar illumination geometry and radiation components.*

The illumination image $cos\beta(x, y)$ is calculated within ATCOR and stored as a separate map. The diffuse solar flux on an inclined plane is calculated with Hay's model (Hay and McKay 1985, also see Richter 1998 for the enhancement with the binary factor b):

$$E_d^*(x, y, z) = E_d(z)[b\tau_s(z)cos\beta(x, y)/cos\Theta_s + \{1 - b\tau_s(z)\}V_{sky}(x, y)] \tag{2.18}$$

The sky view factor can be computed from local information as $V_{sky}(x, y) = cos^2(\Theta_n(x, y)/2)$ based on the local DEM slope angle Θ_n. ATCOR uses the horizon algorithm that provides a more accurate value of the sky view factor by considering the terrain neighborhood of each pixel (Dozier et al. 1981). V_{sky} and $V_{terrain}$ are related by :

$$V_{sky}(x, y) = 1 - V_{terrain}(x, y) \tag{2.19}$$

2.1.2 Illumination based shadow detection and correction

For high resolution imagery, the correction of cast shadows and illumination on the basis of a surface model does not lead to useful results as the surface representation with respect to the radiometry is never accurate enough. Severe over- and under-correction artifacts are observed due to these inaccuracies in the resulting images.

The detection and correction of cast shadows has been widely studied, specifically for space borne high resolution instruments [3, 93]. A new method for cast shadow detection has been implemented for the ATCOR case. It produces a continuous shadow field and relies on the fact that all areas in cast shadows are illuminated by diffuse irradiance only. The diffuse illumination is caused by scattering and thus exhibits very specific spectral characteristics if compared to the direct irradiance. Specifically, the signal in the blue spectral band is significantly higher in cast shadow areas than in directly illuminated areas. For the shadow quantification, the brightness in the NIR spectral band is first calculated using the solar illumination. Secondly, two blue indices have been defined as the band ratios green/blue and red/blue, respectively. These three measures are combined such that a value equivalent to the illumination between 0 and 1 is created (0 being a cast shadow area). The shadow fraction parameter is then defined as:

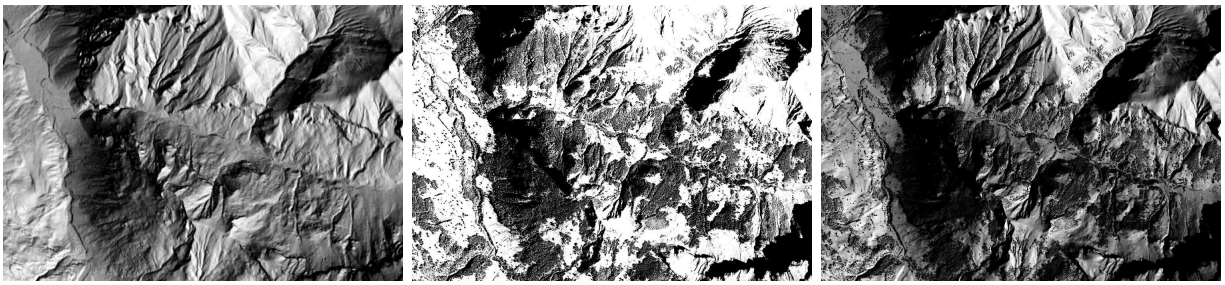

Figure 2.7: *Combination of illumination map (left) with cast shadow fraction (middle) into continuous illumination field (right).*

$$p_{shad} = max[5 \cdot (\frac{L_{red}}{L_{blue}} - 0.35), 8 \cdot (\frac{L_{green}}{L_{blue} + L_{red}} - 0.42), 6 \cdot \rho_{app,nir}] \tag{2.20}$$

where L_{blue}, L_{green}, and L_{red} are the at-sensor radiance values in the true color bands and $\rho_{app,nir}$ is the apparent at-sensor reflectance in the near infrared band. The scaling factors (here: 5,8, and 6) are chosen such that all three parameters are within the same range (i.e., a value range between 0 and 2 and optimized for full cast shadow at 0.5). The parameter p_{shad} is then scaled to a shadow fraction number f_{shad} between 0 (full cast shadow) and 1 (no cast shadow) using empirically found limits. These limits may be variable between sensors. In a second step, this map is combined with the standard geometrically derived illumination field (see Fig.2.7). The resulting illumination map serves as an input to the ATCOR method.

Skyview Factor Estimate

The skyview factor V_{sky} describes the relative amount of the unobstructed sky hemisphere. This factor is highly variable on small scales, e.g., in vicinity of forest borders. The skyview factor is approximated from the cast shadow fraction such that all areas in complete cast shadows get a reduced skyview factor as:

$$V_{sky} = (1 - \frac{\theta_s}{180°} + f_{shad}\frac{\theta_s}{180°}) \cdot 100\% < V_{sky,geom}, \tag{2.21}$$

where θ_s is the solar zenith angle and the geometrical skyview factor $V_{sky,geom}$ had been calculated based solely on the digital terrain model.

Application in ATCOR Workflow

In ATCOR-4, the local illumination angle φ is first calculated on the basis of the terrain model using an efficient vector algebra based method. The topographically corrected reflectance ρ_{topo} is then retrieved from the atmospherically corrected ground leaving excitance (M_g) using the direct irradiance I_{dir}, the diffuse illumination field I_{dif}, and the terrain illumination I_{ter}, as:

$$\rho_{topo} = \frac{M_g}{I_{dir}cos(\varphi) + 0.1I_{dif}cos(\varphi) + 0.9I_{dif}V_{sky} + I_{ter}}, \tag{2.22}$$

where the factors 0.1 and 0.9 account for the relative amount of circumsolar irradiance, estimated to be 10% of the total diffuse irradiance. The local illumination factor $cos(\varphi)$ is now enhanced by the cast shadow fraction, such that shaded areas are not affected by direct and circumsolar irradiance.

Figure 2.8: *Effect of combined topographic / cast shadow correction: left: original RGB image; right: corrected image (data source: Leica ADS, central Switzerland 2008, courtesy of swisstopo).*

After cast shadow correction, the border pixels of the shadows are often under/overcorrected, which is visible as black or bright borders in the cast shadow areas. A filter has to be applied to remove this artifact (compare Fig. 2.9). A simple approach to this problem is an interpolation of all border pixels. However, a considerable data loss may be the result of such a process. Thus a more sophisticated approach is required. As the border pixels are usually isolated, a filter approach has been used which compares the pixel brightness $\overline{\rho_{i,j}}$ to the brightness of its direct neighbors $\overline{\rho_{prox}}$ in a 3x3 or 5x5 box, respectively. The brightness of the shadow border pixel is then adjusted by the relative brightness difference of the whole spectrum such that:

$$\rho_{filt,i,j} = \rho_{i,j}\frac{\overline{\rho_{prox}}}{\overline{\rho_{i,j}}}. \tag{2.23}$$

This method proved to successfully remove shadow borders for high resolution imagery and an urban environment. However, for terrain shadows on a larger scale, the border pixels are not such clearly isolated and often can not be corrected using this method, or only after increasing the size of the border pixel filter significantly.

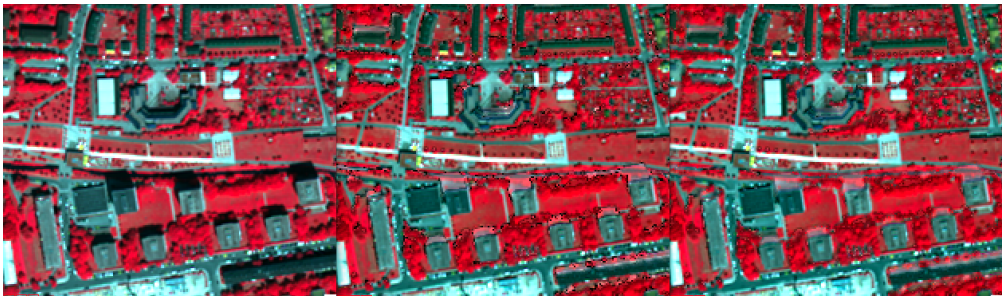

Figure 2.9: *Effect of cast shadow correction (middle) and shadow border removal (right) for building shadows.*

The updated processing leads to improved terrain correction as displayed in Fig.2.8. Advantages of this method are:

- terrain and forest cast shadows are corrected,
- water and cast shadows are discerned (in most cases),
- operational usability has been proven on large ADS data sets, and
- a consistent physically based method applicable to photogrammetry and imaging spectroscopy is implemented.

2.1.3 Integrated Radiometric Correction (IRC)

The IRC method was published by Kobayashi and Sanga-Ngoie [45, 46] to provide a combined atmospheric and topographic correction. The algorithm is briefly outlined here, more details can be found in the original papers.

The first step is the orthorectification of the scene using a digital elevation model (DEM). Then the slope and aspect maps are calculated. The next step is the calculation of the sky view factor, see chapter 2.1.1. The original paper uses the simple equation based solely on the slope angle, but with ATCOR a more accurate calculation based on a ray tracing can also be used in case of a steep terrain. Then the following quantities are computed (keeping the original notation of Kobayashi in most cases):

$$h_0 = \frac{(\pi + 2\theta_s)}{2\pi} \tag{2.24}$$

Here θ_s is the solar zenith angle in radian. IF s denotes the slope map (in radian) then the simple version of the skyview is obtained with

$$h = 1 - s/\pi \tag{2.25}$$

The cosine of the local solar zenith (illumination angle β) is given in eq. 2.17. Then the surface radiance for each channel L_s is calculated by subtracting the path radiance L_p from the at-sensor radiance L:

$$L_s(x, y) = L(x, y) - L_p(x, y, z) \tag{2.26}$$

In the ATCOR version of the IRC algorithm the path radiance varies spatially, particularly due to the DEM height variation, while a constant value (per channel) is used in the original IRC paper. Then a regression analysis (per channel) of L_s versus $cos\beta$ is applied to calculate the slope m and intercept b. After defining $C = m/b$ the topographic correction map A is calculated:

$$A(x,y) = \frac{cos\theta_s + C/h_0}{cos\beta(x,y) + C\ h(x,y)/h_0} \tag{2.27}$$

Finally, the surface reflectance ρ is computed according to:

$$\rho(x,y) = \frac{\pi\ L_s(x,y,z)\ A(x,y)}{T(x,y,z)\ \{E_{dir}(x,y,z)\ cos\theta_s + E_{dif}(x,y,z)\}} \tag{2.28}$$

where T is the total ground-to-sensor transmittance, and $E_{dir},\ E_{dif}$ are the direct irradiance and diffuse solar flux on the ground, respectively.

So the ATCOR version of IRC contains some improvements with respect to the original method: the path radiance varies spatially, mainly caused by terrain height variations, possibly also due to visibility variations, and the sky view factor can be provided from a ray tracing analysis instead of the local slope angle.

Note: the IRC method usually performs well. However, due to the statistical evaluation of the regression analysis unphysically large ($>$ 1 reflectance unit) or small ($<$ 0) surface reflectance values might happen for some pixels, usually in areas with topographic shadow or low local sun elevations.

2.1.4 Spectral solar flux, reflected surface radiance

The spectral solar fluxes on the ground can be calculated by setting the parameter *irrad0 = 1* in the *.inn* file or using the graphical user interface. The fluxes depend on solar geometry, terrain elevation, topography, and atmospheric conditions. All fluxes and the surface reflected radiance of this section are evaluated for the current earth-sun distance. For a flat terrain, ATCOR provides spectra of the direct, diffuse, and global flux for the selected visibility / water vapor. In case of variable visibility / water vapor the spectra are calculated for the average scene visibility / water vapor. The direct flux is just the beam irradiance on the ground times the cosine of the local solar zenith angle. The diffuse flux spectrum E_{dif} is evaluated for a surface reflectance of $\rho = 0$, and the global flux for $\rho = 0.15$, i.e., $E_g = (E_{dir} + E_{dif}(0))/(1 - s\ \cdot\ 0.15)$, where s is the spherical albedo. The spectral band index is omitted for brevity. For a flat terrain these fluxes are provided in the directory of the input file (e.g. *'scene.bsq'*):

- the direct spectral flux on the ground: *'scene_edir.dat'*
- the diffuse spectral flux on the ground: *'scene_edif.dat'* for surface reflectance $\rho = 0$.
- the global spectral flux on the ground: *'scene_eglo.dat'* for a typical average surface reflectance $\rho = 0.15$.

These spectra will already give a realistic description for a flat terrain, but they lack the dependence on the spectral reflectance variations in the scene. Therefore, an image of the global flux is also provided that accounts for the spatial reflectance and visibility / water vapor patterns (VIS, named *'scene_eglobal.bsq'*:)

$$E_g(x,y) = \frac{E_{dir}(VIS(x,y)) + E_{dif}(\rho = 0, VIS(x,y))}{1 - s(x,y)\ \bar{\rho}(x,y)} \tag{2.29}$$

Here, $\bar{\rho}$ indicates a spatial averaging with a filter size corresponding to the specified adjacency range. The unit of the global flux is $mWcm^{-2}\mu m^{-1}$ and it is stored as float data (32 bits/pixel). Therefore, its file size will be twice or four times the size of the input scene if the scene is encoded as 16bit/pixel and 8bits/pixel, respectively.

For a rugged terrain, images of the direct and diffuse fluxes will be calculated using the available DEM information on height (z), slope and aspect (i.e. local solar illumination angle β), and atmospheric conditions (visibility / water vapor VIS). The direct flux on the ground is :

$$E_{dir}(x,y) = b(x,y)\ E_0\ T_{sun}(VIS(x,y,z))\ cos\beta(x,y) \tag{2.30}$$

where E_0, T_{sun} are extraterrestrial solar irradiance and sun-to-ground transmittance, respectively, and b is the topographic shadow mask (0=shadow, 1=sunlit pixel).

The diffuse flux in mountainous terrain accounts for the adjacency effect and multiple reflection effects from the surrounding topography. Using the terrain view factor V_t from the last section and the effective terrain reflectance $\rho_t = V_t(x,y)\ \bar{\rho}(x,y)$ and $\bar{\rho}_t = \bar{V}_t(x,y)\ \bar{\rho}(x,y)$ the diffuse flux is approximated as:

$$\begin{aligned} E_{dif}(x,y) \quad = \quad & E_{dif,flat}\ \{b\ T_{sun}(x,y,z)\ cos\beta/cos\theta_s + \ [1 - b(x,y)\ T_{sun}(x,y,z)]\ V_{sky}(x,y)\} \\ & + \{E_{dir,flat}(x,y,z)\ +\ E_{dif,flat}(x,y,z)\}\ \rho_t(x,y)\ /\ (1 - \bar{\rho}_t(x,y)) \end{aligned} \tag{2.31}$$

The first line describes the anisotropic and isotropic components of the diffuse flux, the second line accounts for multiple terrain reflection effects.

Related quantities to the global spectral solar flux on the ground are the wavelength-integrated global flux and the absorbed solar flux (Wm^{-2}). These play a role in the surface energy balance and they are available as part of the value added channels, see [78].

Surface reflected radiance

The ground reflected (or ground leaving) radiance per band can be obtained in addition to the spectral solar fluxes by setting the parameter irrad0=2. It is calculated corresponding to the surface reflectance cube $\rho(x,y)$, named *'scene_surfrad.bsq'*. For a flat terrain it is:

$$L(surf,x,y) = E(global)\ \rho(x,y)\ /\ \pi \tag{2.32}$$

In case of a mountainous terrrain the direct and diffuse reflected radiation maps from the equations 2.30 and 2.31 are used:

$$L(surf,dir,x,y) = (E_{dir}\ +\ E_{dif})\rho(x,y)\ /\ \pi \tag{2.33}$$

Again, the same output file name is used (*'scene_surfrad.bsq'*).

2.1.5 Thermal spectral region

Similar to the solar region, there are three radiation components: thermal path radiance (L_1), i.e., photons emitted by the atmospheric layers, emitted surface radiance (L_2), and reflected radiance (L_3). The short form of the radiance equation in the thermal region can be written as [40] :

$$L = L_p + \tau\ \varepsilon\ L_{BB}(T) + \tau\ (1-\varepsilon)\ F/\pi \tag{2.34}$$

where

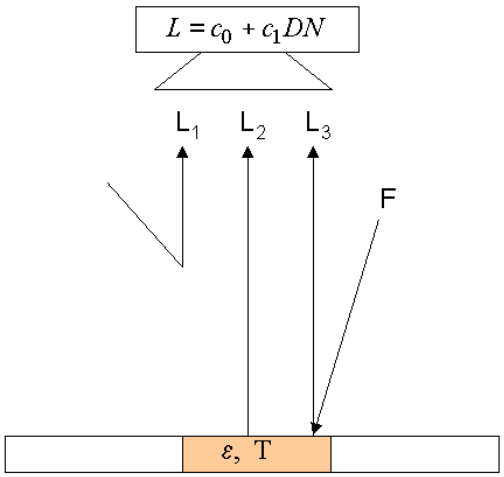

Figure 2.10: *Radiation components in the thermal region.*
$L_1 = L_P$, $L_2 = \tau\ \epsilon\ L_{BB}(T)$, $L_3 = \tau\ (1-\epsilon)\ F/\pi$.

L	at-sensor radiance,
$L_1 = L_P$	thermal path radiance,
τ	ground-to-sensor atmospheric transmittance,
ε	surface emissivity,
T	surface temperature,
L_{BB}	blackbody radiance at temperature T, weighted with the channel's filter curve,
F	thermal downwelling flux on the ground.

The second term on the right-hand side of equation (2.34) is emitted surface radiance reaching the sensor, the third term is the atmospheric radiance reflected at the surface and attenuated by the surface-to-sensor path. The spectral band index, elevation, and angular dependence is omitted for brevity.

The $L_{BB}(T)$ term is Planck's blackbody radiance $B(\lambda, T)$ weighted with the spectral channel response function $R(\lambda)$:

$$L_{BB}(T) = \frac{\int_{\lambda_1}^{\lambda_2} B(\lambda, T) R(\lambda) d\lambda}{\int_{\lambda_1}^{\lambda_2} R(\lambda) d\lambda} \tag{2.35}$$

For a discrete temperature interval $T = (T_1, T_2)$ and increment (e.g. $T_1 = 200\ K$, $T_2 = 350\ K$, increment 1 K) equation (2.35) is solved numerically. Temperature and radiance are then approximated by an exponential fit function function with channel dependent coefficients a_1, a_2:

$$L_{BB} = \frac{a_1}{exp(a_2/T - 1)} \tag{2.36}$$

$$T = \frac{a_2}{ln(a_1/L_{BB} + 1)} \tag{2.37}$$

For convenience, an offset a_0 is introduced with default $a_0 = 0$. The offset term can be used to adjust a temperature bias in a scene. Example: if scene temperatures are too low by 3K they can be raised by setting $a_0 = 3$.

$$T = a_0 + \frac{a_2}{ln(a_1/L_{BB} + 1)} \tag{2.38}$$

Remark:
The computer implementation of the channel-resampled radiance equations is coded to minimize spectral resampling effects [70], [71].

Temperature / emissivity separation

For a sensor with n thermal channels there are n equations of (2.34) with n+1 unknowns, namely the n surface emissivities plus a surface temperature. So, the system of equations (2.34) is always underdetermined. Several possibilities exist to address this problem (Gillespie et al. 1986, 1998 [29, 30]). Five options are offered by the satellite version of ATCOR, see [78]:

- a constant emissivity (default ϵ=0.98 independent of surface cover type, 10-12 μm region) for sensors with a single thermal channel. For user-defined sensors with multiple thermal bands the parameter *itemp_band* (see [78]) defines the channel employed for the surface temperature calculation.

- fixed emissivity values assigned for 3 classes for the selected surface temperature band (parameter *itemp_band*: $\epsilon(soil)$=0.96, $\epsilon(vegetation)$=0.97, else ϵ=0.98 (water and undefined class). The assignment to the vegetation / soil class is performed on-the-fly in memory employing the vegetation index (red and NIR bands required), and the 3-class emissivity map is available (file *'image_atm_emi3.bsq'*, see [78]. In the airborne ATCOR version [79] a pre-classification with more emissivity classes can be used as already suggested in [65].

- for multispectral thermal bands the normalized emissivity method (NEM) or adjusted NEM are also implemented. In the NEM [29], the surface temperature is calculated for all channels with a constant user-defined emissivity, and for each pixel the channel with the highest temperature is finally selected. In the adjusted NEM (ANEM) [15] the assigned emissivity is surface cover dependent. Here, we define four surface cover classes (water, vegetation, soil/dry vegetation, sand/asphalt) based on the following criteria:

  - vegetation: $\rho_{nir}/\rho_{red} > 2$ and $\rho_{nir} > 0.20$.

  - soil/dry vegetation: $\rho_{nir}/\rho_{red} \geq 1.4$ and $\rho_{nir}/\rho_{red} < 2.0$ and $\rho_{red} > 0.09$.

  - sand/asphalt : $\rho_{nir}/\rho_{red} < 1.4$ and $\rho_{red} > 0.09$.

  - water : $\rho_{nir} < 0.05$ and $\rho_{1.6\mu m} < 0.03$.

  To each class the user can assign an emissivity valid for the channel with the highest temperature. There is only one common emissivity class in case of night data or data from purely thermal channels.

The ANEM method provides accurate channel emissivities and surface temperatures if the classes are assigned correctly and the emissivity value assigned to the channel with the maximum temperature is close to the actual channel emissivity. Maximum surface emissivities usually lie in the 10.5 - 13 μm region. After calculating the surface temperature, the emissivities for all channels are computed.

- the ASTER TES algorithm is available for sensors with at least 5 channels in the thermal interval (λ_x, λ_y) with $\lambda_x - FWHM_x/2 \geq 8.08\ \mu m$ and $\lambda_y + FWHM_y/2 \leq 13.0\ \mu m$ to exclude channels in strong absorption regions. The TES algorithm implemented here consists of 3 major parts (Gillespie et al. 1998 [30]):
  - the NEM algorithm described above.
  - the ratio module:
    It calculates relative emissivities β_i (channel i) by ratioing the NEM emissivity values ε_i to their average:
    $$\beta_i = \frac{n\ \varepsilon_i}{\sum_{i=1}^{i=n} \varepsilon_i} \qquad (i = 1, n) \tag{2.39}$$
    Here n is the number of channels in the allowed thermal interval.
  - maximum minimum distance (MMD module) :
    The maximum and minimum values of the relative emissivities (β spectrum) are calculated to find the spectral contrast:
    $$MMD = max(\beta) - min(\beta) \tag{2.40}$$
    Then an empirical relationship is used to predict the actual emissivities ε_i from the MMD employing a regression with laboratory or field emissivity spectra:
    $$\varepsilon_{min} = a + b\ MMD^c \tag{2.41}$$
    For small values $MMD < 0.03$ (e.g. water, vegetation) the value ε_{min} is set to 0.983. The 3 parameters (a, b, c) of the regression can be specified by the user, the default values are taken from [30], i.e., a=0.994, b=-0.687, c=0.737 . The final step calculates the actual emissivities using the β spectrum and ε_{min}:
    $$\varepsilon_i = \beta_i\ \frac{\varepsilon_{min}}{min(\beta)} \qquad (i = 1, n) \tag{2.42}$$
- for thermal band imagery with at least 5 channels the ISAC (In-Scene Atmospheric Compensation) method is available. A detailed description is given by Young et al. [105]. The method does not require ancillary meteorological data or atmospheric modeling. It neglects the downwelling thermal flux and employs the equation
  $$L = L_p + \tau\ \varepsilon\ L_{BB}(T) = L_p + \tau\ L_{surface} \tag{2.43}$$
  This approximation is justified for pixels with a high emissivity close to 1, i.e. "blackbody" pixels. First, the highest brightness temperature T_{max}^{sensor} for each pixel in each channel is computed based on the at-sensor radiance L converted into brightness temperature. In the current implementation, only channels in the spectral region 8 - 13 μm are employed for the maximum brightness temperature search, because the spectral regions $\lambda < 8\ \mu m$ and $\lambda > 13\ \mu m$ are strongly affected by atmospheric water vapor absorption. Next, a reference

channel is defined where most pixels with maximum brightness temperature occur. Only those blackbody pixels are retained which have the maximum brightness temperature in this reference channel ("most hits" method). For these selected blackbody pixels the scatterplot of measured at-sensor radiance L versus blackbody radiance corresponding to $L_{BB}(T_{max}^{sensor})$ is computed for each channel. This means the surface radiance of eq. 2.43 is approximated as $L_{surface} = L_{BB}(T_{max}^{sensor})$. The final step is a least squares regression of the scatterplot data L versus $L_{surface}$, yielding the intercept (path radiance L_p) and slope (transmittance τ) of eq. 2.43. Care has to be taken to apply the regression only to the points near the top edge of all cluster points, but allow some margin, so the fitting line is allowed to sink by an amount of the sensor noise equivalent spectral radiance (NESR). The quality of the regression is significantly increased by allowing only those pixels in the scatterplot that had their maximum temperatures in the reference channel.

Two comments: first, because of the involved assumptions, the obtained intercept is not the physical path radiance, and the slope not the physical atmospheric transmittance. Both quantities may be negative in some channels, therefore they are referred to as unscaled path radiance $L_p^{(u)}$ and unscaled transmittance $\tau^{(u)}$. They might be rescaled to proper atmospheric path radiance and transmittance spectra, e.g. using a radiative transfer code. Second: the ISAC method requires an adequate spread in surface temperatures in the scene, and surface temperatures higher than the atmospheric radiation temperature. So, results for night-time imagery will likely be degraded.

The compensated unscaled surface radiance spectrum is calculated as

$$L_{surface}^{(u)}(\lambda) = \frac{L(\lambda) - L_p^{(u)}(\lambda)}{\tau^{(u)}(\lambda)} \tag{2.44}$$

and the unscaled ISAC surface emissivity can be obtained with

$$\epsilon_{isac}(\lambda) = L_{surface}^{(u)}(\lambda) \ / \ L_{BB}(\lambda, T_{ref}) \tag{2.45}$$

where T_{ref} is the brightness temperature image in the reference channel. The compensated surface radiance spectrum $L_{surface}^{(u)}(\lambda)$ can be converted into the equivalent compensated brightness temperature spectrum where most of the atmospheric absorption features are removed. Both the compensated surface radiance and compensated brightness temperature are spectrally consistent with the data and represent the best estimate for the spectral shape. The emissivity spectrum $\epsilon_{isac}(\lambda)$ may exceed the value 1 in certain channels if the maximum brightness temperature of a pixel does not occur in the selected reference channel. However, a common reference channel is needed in this method to obtain a consistent pixel-independent spectrum of unscaled path radiance $L_p^{(u)}$ and transmittance $\tau^{(u)}$.

Split-window covariance-variance ratio SWCVR

The method derives the water vapor map from thermal band imagery [44, 52, 39]. The water vapor content W can be retrieved as a function of the ratio $R_{j,i}$ of transmittances τ_i, τ_j in two thermal bands i and j:

$$W = a + b \ R_{j,i} \tag{2.46}$$

with

$$R_{j,i} = \frac{\epsilon_j \ \tau_j}{\epsilon_i \ \tau_i} = \frac{\sum_{k=1}^{N} (T_{i,k} - \bar{T}_i) \ (T_{j,k} - \bar{T}_j)}{\sum_{k=1}^{N} (T_{i,k} - \bar{T}_i)^2} \tag{2.47}$$

where N is the number of pixels in a moving window box centered at pixel k, $\bar{T}_i$ is the average brightness temperature in this box, and ϵ is the land surface emissivity. Equation 2.47 is the ratio of covariance to variance accounting for the abbreviation SWCVR. The two selected channels should be in the 10.5 - 12.5 μm region, where the emissivity of most land surfaces changes only slightly, yielding an emissivity ratio ϵ_j/ϵ_i close to 1 yielding $R_{j,i} = \tau_j/\tau_i$. Then the parameters "a" and "b" in eq. 2.46 can be calculated from a regression of channel transmittances versus water vapor content using the pre-calculated LUTs. The moving averaging window box is selected at 100 m $\times$ 100 m. The method requires moderate to high temperature contrasts in the moving window, otherwise results are not reliable. Therefore, it is preferable to retrieve the water vapor map from channels in the solar reflective region if possible.

2.2 Masks for haze, cloud, water, snow

A useful first step before executing an atmospheric correction is the calculation of a pixel map for haze, cloud, water snow, etc. Such a pre-classification has a long history in atmospheric correction methods [24, 42, 65, 66, 67, 43, 53]. It is also employed as part of NASA's automatic processing chain for MODIS [1] using the classes land, water, snow/ice, cloud, shadow, thin cirrus, sun glint, etc. A similar approach is taken here.
The calculation is done "on-the-fly" and if the scene is named "scene.bsq", then the corresponding map is named "scene_out_hcw.bsq". There is also the possibility to provide this information from an external source: if a file ""scene_hcw.bsq" exists in the same folder as the "scene.bsq" then this information is taken and the internal ATCOR calculations for this map are skipped. In this case, the coding of the surface types has to agree with the ATCOR class label definition, of course, see Table 2.1. This file is written if the corresponding flag is set to 1, see [78].

Depending on the available spectral channels, it may not be possible to assign certain classes. Table 2.1 contains one class for cloud (over land, meaning water cloud), whereas the low optical thickness cloud is put into the thin and medium thickness haze class. Thin and medium haze can often be corrected successfully. Of course, there is no clear distinction between thick haze and cloud. We take a pragmatic view, and if the haze removal is successful in areas with thick haze, then these pixels can be included in the haze mask. Since this is not clear at the beginning, it might be necessary to run the program twice, with and without haze removal. A check of the results will reveal whether the haze removal was successful. ATCOR contains a number of criteria to assess the probability of a successful haze removal, and will switch off the haze option if the chances are not good. This automatic haze termination works in most cases, but a success cannot always be guaranteed. There are 5 cirrus classes: thin, medium, thick, cirrus cloud, thick cirrus cloud. The two cirrus cloud classes are merged with the (normal) cloud class for the surface reflectance retrieval during the treatment of the adjacency effect: here the reflectance of the cloud pixels is replaced with the average reflectance of the non-cloud pixels to avoid an overestimation of the adjacency effect. The classes are currently defined with the following criteria:

label	class
0	geocoded background
1	shadow
2	thin cirrus over water
3	medium cirrus over water
4	thick cirrus over water
5	land
6	saturated (blue/green band)
7	snow / ice
8	thin cirrus over land
9	medium cirrus over land
10	thick cirrus over land
11	thin haze over land
12	medium haze over land
13	thin haze over water
14	medium haze over water
15	cloud over land
16	cloud over water
17	water
18	cirrus cloud
19	cirrus cloud thick

Table 2.1: *Class labels in the hcw file.*

Water class:

The following TOA reflectance thresholds are employed for water:

$$\rho^*(red) < 0.20 \quad and \quad \rho^*(green) > \rho^*(red)$$
$$\rho^*(NIR) < T_{NIR} \quad and \quad \rho^*_{SWIR1} < T_{SWIR1} \quad and \quad NDVI < 0.1 \tag{2.48}$$

where $T_{NIR} = max(0.07, T_{water,NIR})$ and $T_{water,NIR}$ is the user-defined threshold (in the 'preference_parameters.dat'). Similarly, $T_{SWIR1} = max(0.05, T_{water,SWIR1})$ and $T_{water,SWIR1}$ is the user-defined threshold in the 'preference_parameters.dat'.
Note: this requires a positive value of $T_{water,NIR}$, $T_{water,SWIR1}$. If these thresholds are negative, then the following criteria are employed:

$$\rho^*(red) < 0.20 \quad and \quad \rho^*(NIR) < |T_{water,NIR}| \quad and \quad NDVI < 0.1 \tag{2.49}$$

The relations 2.49 are applied for sensors without a SWIR band.

$$\rho^*(red) < 0.20 \quad and \quad \rho^*_{SWIR1} < |T_{water,SWIR1}| + 0.01 \quad and \quad NDVI < 0.1 \tag{2.50}$$

The relations 2.50 are applied for sensors with a SWIR1 (1.6 μm) band.

Saturated pixels:

These pixels fulfill the criterion

$$DN(blue) \geq T_{saturation} \tag{2.51}$$

where $DN(blue)$ is the digital number in a blue band (around 470 nm) and the threshold $T_{saturation}$ is defined in the preference parameter file. If a blue band does not exist, a green band (around 550 m) is used as a substitute. If a green band also does not exist, a red band (around 650 nm) is used. $T_{saturation} = b \cdot encoding$, default b=1.0, e.g. 1.0*255=255 for 8 bit sensors with encoding=255. A lower value, e.g. b=0.98, might be used because nonlinear effects might already occur ot lower radiance levels. This would provide some safety margin and indicate situations near saturation. Setting b=0.98 for an 8-bit sensor means that pixels exceeding DN = 0.98*255=250 will be marked as (nearly) saturated. For a 32 bit encoding (integer or float) no saturation threshold is defined. As saturation usually occurs in the blue-to-red part of the spectrum, channels in this region are checked and assigned to the class 'saturated', false color coded red in the *"*_out_hcw.bsq"* file. However, the *"*_atm.log"* file contains the percentage of saturated pixels for each channel.

Cloud over land:

Pixels must satisfy the conditions:

$$\begin{aligned} &\rho^*(blue) > T_c \quad and \quad \rho^*(red) > 0.15 \quad and \quad \rho^*(NIR) \;/\; \rho^*(red) < 2 \\ &\quad and \quad \rho^*(NIR) > 0.8\;\rho^*(red) \quad and \quad \rho^*(NIR) \;/\; \rho^*(SWIR1) > 1 \\ &\qquad\qquad and \quad NDSI < 0.7 \quad or \quad DN(blue) > T_{saturation} \end{aligned} \tag{2.52}$$

where $\rho^*(blue)$ is the apparent reflectance in a blue band, T_c is the cloud threshold as defined in the preference parameter file, and $DN(blue)$ is the corresponding digital number. If no blue band is available, a green band (around 550 nm) is taken as a substitute. If no green band exists, a red band (around 650 nm) is taken. NDSI is the normalized difference snow index:

$$NDSI = \frac{\rho^*(green) \;-\; \rho^*(SWIR1)}{\rho^*(green) \;+\; \rho^*(SWIR1)} \tag{2.53}$$

Note that saturated pixels in visible bands are automatically counted as cloud although they might be something else (e.g., snow, or a specular reflection from a surface). If a thermal band exists, the following cloud criterion must also be fulfilled:

$$(1 \;-\; \rho^*(SWIR1))\; T_{bb} < 225\;(Kelvin) \quad and\; exclude \quad T_{bb} > 300\;(Kelvin) \tag{2.54}$$

where T_{bb} is the at-sensor blackbody temperature in the selected thermal band.

Cloud over water:

The following criteria have to be fulfilled:

$$\begin{aligned} &0.20 < \rho^*(blue) < 0.40\;, \quad \rho^*(green) < \rho^*(blue) \\ &\rho^*(NIR) < \rho^*(green)\;, \quad \rho^*(SWIR1) < 0.15\;, \quad NDSI < 0.2 \end{aligned} \tag{2.55}$$

For optically thick clouds it is not possible to distinguish clouds over water from clouds over land if only spectral criteria are used.

Cloud shadow:

Pixels must satisfy the conditions:

$$\rho^*(red) < 0.06 \quad , \quad \rho^*(NIR) > \rho^*(red) + 0.04 \quad , \quad 0.02 < \rho^*(SWIR1) < 0.08 \tag{2.56}$$

and they should not belong to the water class. This may also include building shadow pixels.

Snow / ice:

Pixels must satisfy the conditions:

$$\rho^*(blue) > 0.22 \quad and \quad NDSI > 0.6 \quad and \quad DN(blue) < T_{saturation} \tag{2.57}$$

The condition $DN(blue) < T_{saturation}$ means that saturated pixels in the blue spectral band are not included in the snow mask, instead they are put into the cloud class. If no blue band exists, a green band (around 550 nm) is taken. However, if the blue or green band is saturated and $NDSI > 0.7$ then this pixel is assigned to the snow class because of the very high probability. If a green band and a SWIR2 band (around 2.2 μm) exist the following relationships are used:

$$\begin{aligned} &DN(blue) < T_{saturation} \quad and \quad (\ (\rho^*(blue) > 0.22 \ , \quad NDSI > 0.6) \\ &or \quad (\rho^*(green) > 0.22 \ , \quad NDSI > 0.25 \ , \quad \rho^*(SWIR2)/\rho^*(green) < 0.5 \ ) \ ) \end{aligned} \tag{2.58}$$

Again, if the blue or green band is saturated and $NDSI > 0.7$ then the snow class is assigned.

Cirrus over land and water:

The apparent cirrus reflectance is calculated in the cirrus band (1.38 μm). Cirrus classes are defined according to the apparent reflectance. Thin cirrus over land is calculated with

$$1.0\% < \rho^*(cirrus) < 1.5\% \tag{2.59}$$

employing the percent reflectance unit. Medium thickness cirrus is calculated as

$$1.5\% \geq \rho^*(cirrus) < 2.5\% \tag{2.60}$$

and the thick cirrus class consists of pixels with

$$2.5\% \geq \rho^*(cirrus) < 4.0\% \tag{2.61}$$

The same definition is used for cirrus over water if the land/water distinction is still possible based on the selected spectral criteria.

Still higher apparent reflectance values are defined as 'cirrus cloud' if

$$4.0\% \geq \rho^*(cirrus) < 5.0\% \tag{2.62}$$

and 'thick cirrus cloud' if

$$\rho^*(cirrus) \geq 5.0\% \tag{2.63}$$

and no distinction concerning land/water is made for the last two classes.
Cirrus detection is switched off in the following cases:

- no water vapor map available: if DEM height ¿ 2000 m
- water vapor map W available: if W ¡ 1 cm or W ¡ Twv where Twv is the water vapor threshold specified in the file *preference_parameters.dat*

Haze over land: see chapter 2.6.3

The the mean of the tasseled cap transformation (TC) is calculated. Clear pixels are those with $TC < mean(TC)$ and $\rho^*(blue) < T_c$ (cloud over land threshold) and $\rho^*(NIR) > T_{water}(NIR)$ (water reflectance threshold, defined in "preference_parameters.dat"). Next, the mean and standard deviation σ of the HOT transformation (HOT = Haze Optimized Transform) are calculated. Pixels are assigned to the compact haze mask if $HOT > mean(HOT)$, and to the large haze mask if $HOT > mean(HOT) - 0.5\ \sigma(HOT)$. Then the HOT histogram of all haze pixels is calculated. Pixels with values less than 40% of the cumulative histogram are assigned to thin-medium haze, pixels with higher values to medium-thick haze. This distinction is arbitrary and has no effect on the subsequent processing.

Haze over water:

Pixels must belong to the water mask, and the NIR apparent reflectance $\rho^*(NIR)$ must be greater than the NIR clear water threshold $T_{clear_water_NIR}$ defined in the preference parameter file, see [78]. Thin haze over water is defined as:

$$T_{clear_water_NIR} \geq \rho^*(NIR) \geq 0.06 \tag{2.64}$$

Medium haze over water is defined as:

$$0.06 < \rho^*(NIR) \leq T_2 \tag{2.65}$$

where T_2 (default=0.12) is another editable parameter in the preference file. The method of haze removal over water is described in chapter 2.6.4. The same technique is also employed to remove sun glint.

2.3 Quality layers

The previous section defined a coarse pixel classification which is useful for an atmospheric correction. In addition, it supports an assessment of the quality of the processing. For example, a large error in the radiometric calibration could cause a scene classification with all pixels labeled as water. In this case, a user can immediately identify the problem. Of course, a more detailed assessment is possible with an analysis of the reflectance spectra. Nevertheless, the classification map (land, water, haze, cloud, etc) is a useful product and the quality of the atmospheric correction may depend on the correct class assignment, at least for some classes.

The previous (haze, cloud, water, land) pixel classifyer is a binary decision: a pixel belongs to a certain class or not. In reality the decision is typically not unique and a class assignment has only a certain probability. As the absolute probability of a class assignment is very difficult to assess, we use a simple 1-parameter equation to estimate a relative probability (0 - 100%). Currently there are three quality layers: cloud, water, and snow/ice.

Cloud probability:
If a pixel belongs to the cloud class then the TOA reflectance of the red band is used together with a

linear scaling between the two reflectance thresholds $T_{c1} = 0.15,\ T_{c2} = 0.35$ and the corresponding probabilities p1=60% and p2=100%:

$$p(cloud) = p1 + (p2 - p1) * \frac{\rho^*(red) - T_{c1}}{T_{c2} - T_{c1}} \tag{2.66}$$

Probabilities higher than 100 are truncated to 100, values lower than 30 are reset to 30.

Water probability:
If a pixel belongs to the water class then the NDVI is used together with a linear scaling between the two NDVI thresholds $T_{w1} = -0.30,\ T_{w2} = 0.10$ and the corresponding probabilities p1=60% and p2=100%:

$$p(water) = p1 + (p2 - p1) * \frac{NDVI - T_{w1}}{T_{w2} - T_{w1}} \tag{2.67}$$

Probabilities higher than 100 are truncated to 100, values lower than 30 are reset to 30.

Snow /ice probability:
If a pixel belongs to the snow/ice class then the NDSI is used together with a linear scaling between the two NDVI thresholds $T_{s1} = 0.70,\ T_{s2} = 0.25$ and the corresponding probabilities p1=60% and p2=100%:

$$p(snow) = p1 + (p2 - p1) * \frac{NDSI - T_{s1}}{T_{s2} - T_{s1}} \tag{2.68}$$

Probabilities higher than 100 are truncated to 100, values lower than 30 are reset to 30.

2.4 Quality confidence layer

A quality confidence layer map ('scene_atm_qcl.bsq') for a file 'scene.bsq' is available indicating the overall relative quality of the surface reflectance product. The values range from 0 - 100, with 100 the best quality. The quality depends on the aerosol optical thickness at 550 nm (AOT550) and the solar zenith angle (SZA). In mountainous terrain, the local SZA is used. Figure 2.11 presents the functions Q(SZA) and Q(AOT550). The final quality confidence value is the product Q = Q(SZA) * Q(AOT550). No quality confidence file will be written for a flat terrain scene and constant visibility, because SZA and AOT550 do not vary (at least for small FOV imagery).

2.5 Standard atmospheric conditions

Standard conditions comprise scenes taken under a clear sky atmosphere. This means the visibility (aerosol optical thickness) can be assumed as constant over a scene, or it might vary within a certain range (excluding haze) and a visibility map can be calculated. It also includes situations with constant or spatially varying water vapor column contents.

2.5.1 Constant visibility (aerosol) and atmospheric water vapor

This is the easiest case for atmospheric correction. Still, it can often be applied if homogeneous atmospheric conditions exist. These might be encountered for small area scenes, i.e., high spatial resolution imagery. If the sensor has no channels in atmospheric water vapor regions, results of

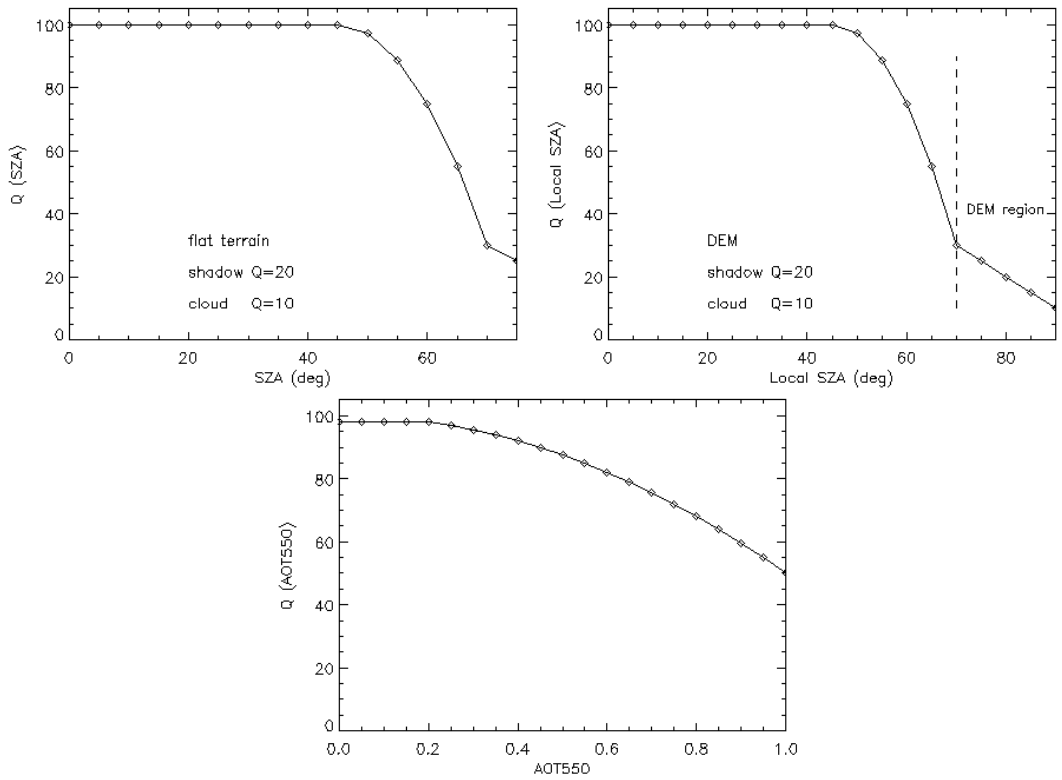

Figure 2.11: *Quality confidence Q(SZA) and Q(AOT550).*

atmospheric correction are not sensitive with respect to the selected water vapor content, and a climatological value (e.g., midlatitude summer, US standard, or tropical water vapor profile) is usually sufficient. For hyperspectral instruments, the processing has to include the image-derived pixel-by-pixel water vapor map.

The program performs a check whether the specified visibility leads to negative reflectance pixels for dark surfaces in the red band (660 nm, vegetation) and NIR band (850 nm, water). If this is the case, the visibility is iteratively increased (up to VIS=120 km) to reduce the percentage of negative reflectance pixels below 1% of the scene pixels. During an interactive ATCOR session the user is notified, and can continue with the recommended visibility update or with the initial visibility. During batch mode operation the program continues with the updated visibility (if the input visibility in the .inn file is positive). For a negative visibility (in the '*.inn' file) no visibility iterations are performed. A corresponding notice on the final visibility is given in the "*atm.log" output file. The set of visibility grid point is given in Table 2.2.

The iteration capability is most important for low visibility start values.

2.5.2 Aerosol retrieval and visibility map

If a sensor has the appropriate spectral bands the aerosol type and visibility or optical thickness of the atmosphere can be derived, provided the scene contains reference areas of known reflectance behavior (Kaufman and Sendra 1988, Kaufman et al. 1997). The minimum requirements are spec-

visibility [km]	vis. increment [km]
5	3
8	3
11	3
14	3
17	3
20	3
23	3
26	4
30	5
35	5
40	5
50	10
60	10
70	10
80	20
100	20
120	max VIS=120 km

Table 2.2: *Visibility iterations on negative reflectance pixels (red, NIR bands).*

tral bands in the red and near IR. If the scene contains dense dark vegetation (DDV, coniferous type) the reflectance values in the red band can be obtained from a correlation with the SWIR band reflectance as detailed below. The visibility of each reference pixel can then be calculated in the red band as the intersection of the modeled at-sensor radiance curve with the measured radiance, see figure 2.12.

The measured radiance for a reference pixel of digital number DN is $L = c_0 + c_1 DN$, which is a constant value indicated by the dashed line in figure 2.12. The curve indicates the modeled radiance. It employs the reflectance of the reference surface (e.g., $\rho_{ref} = 0.02$) and uses values of path radiance, atmospheric transmittance, and global flux for the current solar and viewing geometry stored in precalculated LUTs.

Automatic masking of reference areas (1.6 or 2.2 μm band required, or at least red/NIR bands)

If the sensor has a SWIR band (at 1.6 or 2.2 μm), then the scene can be searched for dark pixels in this band and a correlation of the SWIR reflectance with the reflectance in the red and blue band can be employed to estimate the visibility automatically (Kaufman et al. 1997). For this purpose, we use a modified version of the original idea for the following algorithm.
If a SWIR band exists the SWIR reflectance is calculated assuming a visibility of 23 km (instead of the original version of top of atmosphere reflectance). Then, water pixels are excluded by employing only those pixels with SWIR reflectance values above 1% and an NDVI > 0.1. For the 2.2 μm band the upper threshold of the reflectance of the dark pixels is selected as 5%. If the number of reference pixels is less then 1% of the image pixels, then the upper threshold is increased to 10% or finally 12%. If a 1.6 μm band exists, but no 2.2 μm band, the corresponding upper thresholds are selected as 10% and 15%, or finally 18%, respectively. The reflectance ratios for the red (near 0.66 μ) and

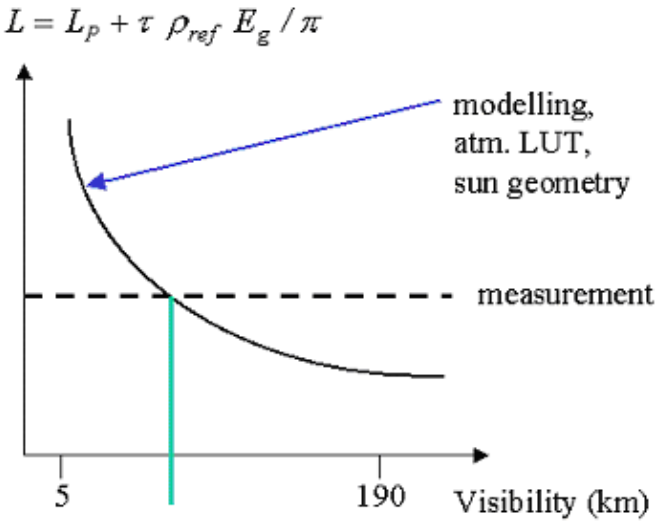

Figure 2.12: *Schematic sketch of visibility determination with reference pixel.*

blue (near 0.48 μm) band are then calculated as :

$$\rho_{red} = 0.5\ \rho_{2.2} \qquad and \qquad \rho_{0.48} = 0.5\ \rho_{0.66} + 0.005 \tag{2.69}$$

$$\rho_{red} = 0.25\ \rho_{1.6} \qquad and \qquad \rho_{0.48} = 0.5\ \rho_{0.66} + 0.005 \tag{2.70}$$

The offset 0.005 for the blue band yields a better correlation with ground measurements than a zero offset ([51]. Therefore, it is included starting with the 2013 release of ATCOR.

This situation is sketched in figure 2.13. The correlation factor of 0.5 between the 2.2 μm and the red region is not a universal constant, but may typically vary between 0.4 and 0.6. The correlation actually also works for dark soils. So the dark pixels may also include soil areas. For narrow band hyperspectral sensors a band close to 2.13 μm is used instead of a 2.20 μm band.
The red band is then used to calculate the visibility (compare figure 2.12) as the intersection of the measured radiance with the simulated visibility-dependent at-sensor radiance curve. Since the same visibility is employed for the blue spectral band this provides an opportunity to adjust the spectral behavior of the path radiance (which is essentially the aerosol path radiance, since the Rayleigh path radiance is known) in the blue spectral region.

$$L_{p,blue}^{update} = L_{blue} - \tau_{blue}\rho_{blue}E_{g,blue}/\pi \tag{2.71}$$

Deep blue channels

For most multispectral sensors a blue channel in the 470 - 490 nm region was the shortest wavelength channel in the past. However, with the availability of Worldview-2 and Landsat-8 OLI and hyperspectral data there is often a need to adjust the path radiance in the deep blue region $<$ 470 nm, because the limited set of discrete aerosol models might not be adequate. Therefore, an empirical approach is taken: the DDV surface reflectance at 400 nm is set to 0.6 times the

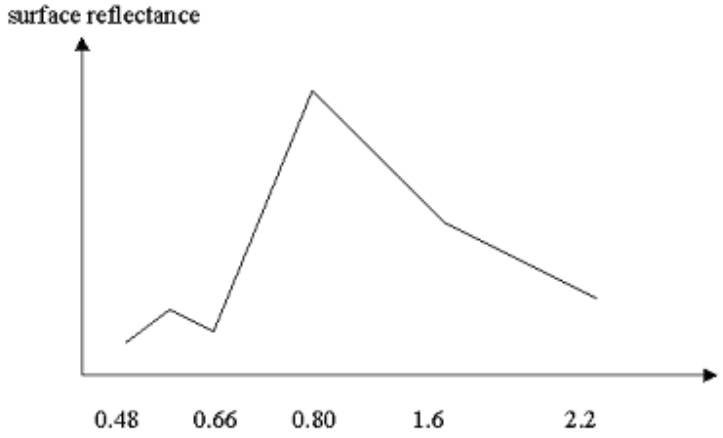

Figure 2.13: *Correlation of reflectance in different spectral regions.*

reflectance of the standard blue (480 nm) channel and the reflectance for channels in between is linearly interpolated:

$$\rho^{ddv}_{0.400} = 0.6\ \rho^{ddv}_{0.480} \tag{2.72}$$

$$\rho^{ddv}(\lambda) = \rho^{ddv}_{0.400} + \frac{\rho^{ddv}_{0.480} - \rho^{ddv}_{0.400}}{0.480 - 0.400}\ (\lambda - 0.400) \tag{2.73}$$

Multispectral sensors usually have only one or two channels in the 400 - 470 nm region. In case of hyperspectral instruments, the channels closest to 410 nm and 440 nm are selected as tie channels to calculate the corresponding path radiance, and exponential interpolation is used to obtain the path radiances for the remaining bands in the 400 - 480 nm region.

The question of an automatic aerosol type calculation is addressed next. It is restricted to the available number of aerosol models, and uses path radiance ratios of the 0.66, 0. 48 μm channels derived from the scene DDV pixels and the corresponding path radiance in the MODTRAN LUTs.

Aerosol type estimation

After calculation of the scene path radiance in the blue (0.48 μm) and red (0.66 μm) region (as total minus reflected radiance, using the average values obtained for the dark reference pixels) the ratio of $L_p(blue, scene)$ to $L_p(red, scene)$ can be compared to the corresponding ratio for the MODTRAN standard aerosols (rural, urban, maritime, desert) :

$$d_p = \frac{L_p(blue, scene)/L_p(red, scene)}{L_p(blue, MODTRAN)/L_p(red, MODTRAN)} \tag{2.74}$$

The aerosol type for which the double ratio (d_p) is closest to 1 is the best approximation for the scene. It approximates the corresponding MODTRAN aerosol type. However, some fine tuning is subsequently performed to be able to modify the wavelength behavior of the path radiance compared to the standard aerosol types. If $L_p(blue, scene)$ deviates more than 5% from $L_p(blue, MODTRAN)$ then $L_p(blue, scene)$ is used as the valid path radiance. In addition, the path radiance for any other bands in the blue to red region is linearly re-scaled with the factor

$L_p(blue, scene)/L_p(blue, MODTRAN)$, see Figure 2.14. Here, the path radiance in the red band is used as a fixed tie point. For wavelengths greater than 700 nm a posssible typical 10% difference in path radiance between the selected aerosol type (after fine tuning) and the actual aerosol is usually not important, because path radiance contributes only a small fraction to the total radiance.

If the sensor has no blue spectral band, but a green band, than the green band is substituted and for the dense dark vegetation the surface reflectance relationship is used:

$$\rho(green) = 1.3\ \rho(red) \tag{2.75}$$

Now eq. 2.71 is again employed for the green band instead of the blue band to calculate the path radiance, the best match to a MODTRAN aerosol type, and possibly a fine tuning of the path radiance.

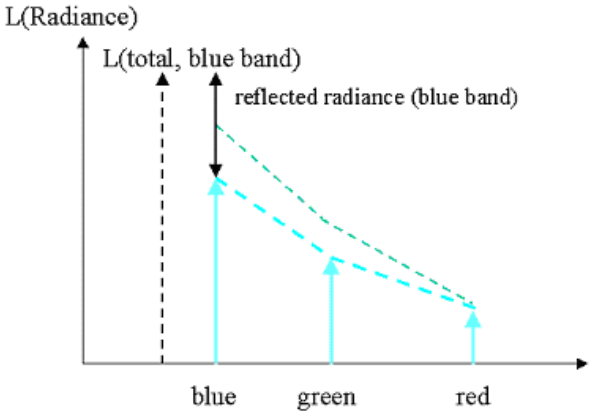

Figure 2.14: *Rescaling of the path radiance with the blue and red band.*
After subtraction of the reflected radiance from the total radiance in the blue band the remaining signal is the updated path radiance in the blue band. The path radiance of bands in the blue to red region is then rescaled with interpolation.

Aerosol retrieval for VNIR sensors

If no SWIR bands exist, but at least a red band (around 660 nm) and a NIR band (around 850 nm) a different approach has to be taken, see reference [74] for details. It starts with the assumption of average clear atmospheric conditions (visibility VIS=23 km) to calculate the surface reflectance in the red and NIR bands which is appropriate for situations of clear atmospheres (VIS = 15 - 40 km). The second step derives a mask of dark vegetation pixels using the ratio vegetation index rvi of the red and near-infrared surface reflectance, $rvi = \rho_{nir}/\rho_{red}$, and multiple reflectance thresholds:

- The mask pixels have to fulfill: $rvi \geq 3$ and $\rho_{nir} \geq 0.10$ and $\rho_{nir} \leq 0.25$ and $\rho_{red} \leq 0.04$.

Water pixels are automatically excluded from this mask because of the $\rho_{nir} \geq 0.10$ condition, and soil pixels are excluded with the combination of all four conditions. If the percentage of reference pixels is smaller than 2% of the scene the search is iterated with VIS=60 km (covering the very clear conditions of visibility = 40 - 60 km). Again, if the percentage is smaller than 2%, the search is iterated with VIS=10 km to cover higher aerosol loadings (VIS = 8 - 15 km). Each visibility iteration is supplemented with an iteration of the threshold ρ_{red} which is decreased in steps of 0.005 down to $\rho_{red} = 0.025$ to include only the darkest vegetation pixels (see [74] for details). Currently,

the algorithm terminates if less than 2% reference pixels are found after these two iterations. In this case, the user has to employ the constant visibility option specifying the value of the visibility for the scene. During batch mode operation the program takes the specified visibility (from the ".inn" file). Then a check for negative reflectance pixels is performed with dark pixels in the red band (660 nm, vegetation) and the NIR band (850 nm, water), and the visibility is iteratively increased (up to VIS=60 km) to reduce the percentage of negative reflectance pixels below 1% of the scene pixels. A corresponding notice is given in the "*atm.log" output file.
The third step calculates the surface reflectance in the red band as a fraction α of the NIR band reflectance:

$$\rho_{red} = \alpha * \rho_{nir} = 0.1 * \rho_{nir} \tag{2.76}$$

Similar to the empirical SWIR relationships the coefficient $\alpha = 0.1$ is an average empirical value yielding results in close agreement with the SWIR method in many cases. However, deviations from the nominal value $\alpha = 0.1$ can vary about 30% depending on biome. Before the final step of atmospheric correction takes place the visibility of non-reference pixels in the scene can be set to the average value of the reference pixels or a spatial interpolation can be applied.

If the percentage of dark reference pixels with eq. 2.76 is less than 2% and if a blue spectral band exists, then the atmospherically resistent vegetation index (ARVI) is employed to include somewhat brighter pixels as reference areas. The ARVI is defined as :

$$ARVI = \frac{\rho^*_{NIR} - \rho^*_{rb}}{\rho^*_{NIR} + \rho^*_{rb}} \tag{2.77}$$

The asterisk in ρ^* indicates a TOA reflectance with the Rayleigh contribution already subtracted, and

$$\rho^*_{rb} = \rho^*_{red} + 1.3\ (\rho^*_{red} - \rho^*_{blue}) \tag{2.78}$$

If A_1, A_2 are the lower and upper ARVI thresholds ($A_2 = 0.9$ is fixed) then additional dark reference pixels are searched which fulfill $A_1 < ARVI < A_2$. The inital value is $A_1 = 0.8$, and it is iteratively decreased to $A_1 = 0.64$ until at least 2% of these additional reference pixels are found or the iteration terminates. We use the following simple empirical equation for the surface reflectance in the red band:

$$\rho_{red} = 0.01 + 0.03\ \frac{ARVI - A_2}{A_1 - A_2} \tag{2.79}$$

In reality, this relationship is dependent on biome, season, and geography [87]. Corresponding maps have been developed for the MERIS sensor, using a coarse reolution of about 3 km x 3 km, but these are not appropriate for high spatial resolution instruments. Finally, the dark reference pixels from both VNIR approaches (eq. 2.76 and 2.79 are combined.

Visibility and aerosol optical thickness

The visibility calculated for each reference pixel (range 5 - 190 km in ATCOR) is converted into an integer, called visibility index vi, with range 0-182. The visibility index is closely related to the total optical thickness δ at 550 nm, the equidistant optical thickness spacing is 0.006 for a ground at sea level, and smaller for increasing elevations.

$$\delta = 0.185 + 0.006 * vi \tag{2.80}$$

It is easy to calculate the aerosol optical thickness (AOT) from a known total optical thickness by subtracting the Rayleigh optical thickness and a very small trace gas optical thickness, see [78]. With the MODTRAN code the AOT (at 550 nm) can be calculated from a given visibility VIS (km) as

$$AOT = exp\,(a(z) + b(z)\ ln(VIS)) \tag{2.81}$$

where z is the surface elevation, and a(z), b(z) are coefficients obtained from a linear regression of $ln(AOT)$ versus $ln(VIS)$.

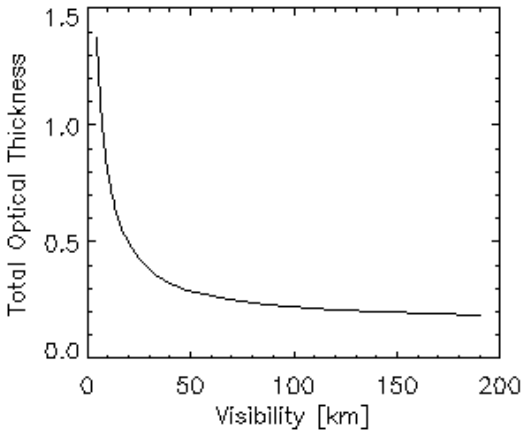

Figure 2.15: *Optical thickness as a function of visibility and visibility index.*

2.5.3 Water vapor retrieval

A water vapor retrieval can be included after the aerosol retrieval because the aerosol retrieval does not use water vapor sensitive spectral bands, but the water vapor algorithm (employing bands around 820 nm, 940 nm, or 1130 nm) depends on aerosol properties. The water vapor retrieval over land is performed with the APDA (atmospheric precorrected differential absorption) algorithm [88]. In its simplest form, the technique uses three channels, one in the atmospheric water vapor absorption region around 820 nm, 940 nm, or 1130 nm (the "measurement" channel), the others in the neighboring window regions ("reference" channels). The depth of the absorption feature is a measure of the water vapor column content, see figure 2.16.
In case of three bands the standard method calculates the water vapor dependent APDA ratio as :

$$R_{APDA}(\rho, u) = \frac{L_2(\rho_2, u) - L_{2,p}(u)}{w_1(L_1(\rho_1) - L_{1,p}) + w_3(L_3(\rho_3) - L_{3,p})} \tag{2.82}$$

where the index 1 and 3 indicates window channels (e.g. in the 850-890 nm region and 1010-1050 nm region), respectively. Index 2 indicates a channel in the absorption region (e.g., 910-950 nm). L and L_p are the total at-sensor radiance and path radiance, respectively. The symbol u indicates the water vapor column. The weight factors are determined from

$$w_1 = (\lambda_3 - \lambda_2)/(\lambda_3 - \lambda_1) \qquad and \qquad w_3 = (\lambda_2 - \lambda_1)/(\lambda_3 - \lambda_1) \tag{2.83}$$

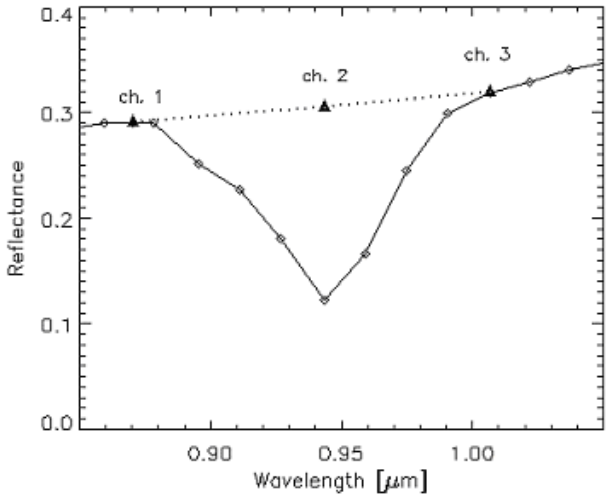

Figure 2.16: *Reference and measurement channels for the water vapor method. The at-sensor radiance is converted into an at-sensor reflectance.*

The problem is the estimation of the surface reflectance ρ_2 in the absorption band (eq. 2.82). The technique tries to estimate the reflectance ρ_2 with a linear interpolation of the surface reflectance values in the window channels (ch. 1, 3) that are not or only slightly influenced by the water vapor content: Therefore, the reflectance ρ_2 is calculated as

$$\rho_2 = w_1\rho_1 + w_3\rho_3 \tag{2.84}$$

Then equation (2.82) can be written as

$$R_{APDA}(u) = \frac{\rho_2\tau_2(u)E_{g2}(u)}{\rho_2\tau_2(u=0)E_{g2}(u=0)} = \frac{\tau_2(u)E_{g2}(u)}{\tau_2(u=0)E_{g2}(u=0)} \tag{2.85}$$

where $E_{g2}(u)$ is the global flux on the ground for the measurement channel (index 2). ATCOR employs 4 to 5 water vapor columns (u=0.4, 1.0, 2.0, 2.9, 4.0 cm, sea-level-to space geometry) to calculate an exponential fit function

$$R_{APDA}(u) = exp(-\alpha + \beta\sqrt{u}) \tag{2.86}$$

which can be solved for the water vapor column u , see Fig. 2.17, where the diamonds in the figure mark the calculated water vapor grid points (u= 0.4, 1.0, 2.0, 2.9 cm) :

$$u = (\frac{\alpha + lnR_{APDA}}{\beta})^2 \tag{2.87}$$

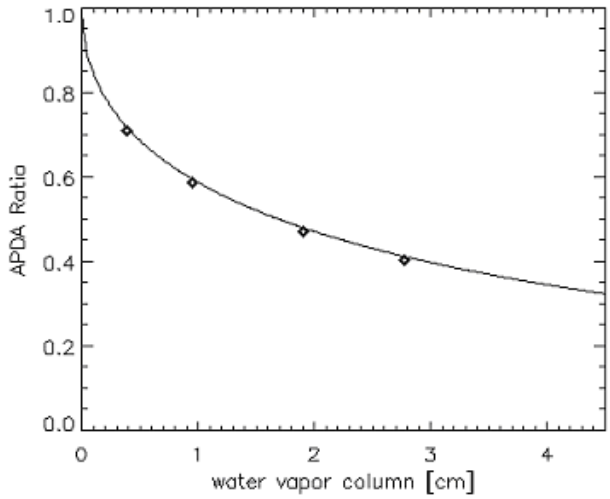

Figure 2.17: *APDA ratio with an exponential fit function for the water vapor.*

Equations (2.82, 2.84 to 2.87) are iterated, starting with u=1.0 cm, calculating R_{APDA}, updating u, $L_{i,p}(u)$, ρ_1, ρ_3 and repeating the cycle. A minimum of two channels (one reference, one measurement channel) is required. The advanced APDA method can take into account multiple absorption channels in the 810-820 nm, 910-960 nm and 1110-1150 nm regions. Two water vapor retrieval algorithms are available in ATCOR (see [78]).

1. The water vapor maps with the smallest standard deviation in the 940 nm and 1130 nm region are selected. Finally, if both regions are available, the average of these two water vapor maps is taken (parameter iwv_model=1 in the ".inn" file).

2. A linear regression ratio (LIRR) is applied to multiple bands (parameter iwv_model=2). This water vapor map might be more accurate, because the regression reduces sensor noise and may partially compensate calibration problems in lucky cases. Although the water vapor map might be less noisy, the retrieved surface reflectance spectrum will always retain any channel calibration problems.

Remarks:

1. The APDA algorithm is relatively fast. Its disadvantage is that it is not stable numerically for very low reflectance targets (water, shadow regions). The transmittance slope ratio method [83] might work better in these cases, so it is an interesting alternative water vapor algorithm. However, since the required processing time is much higher than for the APDA method, it is currently not implemented in the ATCOR environment. In addition, the method requires data with a very accurate spectral and radiometric calibration, otherwise its potential advantage will be lost.

2. Five water vapor grid points at 0.4, 1.0, 2.0, 2.9, and 4.0 cm are sufficient to cover the 0.5 - 5.0 cm range with an accuracy of about 5-10 % [76].

2.6 Non-standard conditions

The non-standard situations refer to scenes with a substantial amount of haze and shadow areas. The non-standard atmospheric conditions treat the haze removal and de-shadowing employing spectral and statistical algorithms. Although bidirectional surface reflectance effects are independent of the atmospheric conditions, the subject is included here, because the isotropic reflector is used for the standard conditions. We present some methods of BRDF correction in flat and rugged terrain.

2.6.1 Haze removal

In many cases of satellite imagery the scene contains haze and cloud areas. The optical thickness of cloud areas is so high that the ground surfaces cannot be seen, whereas in hazy regions some information from the ground is still recognizable. In ATCOR the scene is partitioned into clear, hazy, and cloud regions. Here we will treat the low altitude boundary layer (0 - 3 km) haze as opposed to high altitude cirrus. Thin boundary layer haze can be detected with broad-band multispectral instruments, while a detection of thin cirrus requires specific narrow bands around 1.38 μm or 1.88 μm, compare chapter 2.6.5. As a first approximation, haze is an additive component to the radiance signal at the sensor. It can be estimated and removed as described below. Cloud areas have to be masked to exclude them from haze areas and to enable a successful haze removal. The treatment of cloud shadow regions is discussed in chapter 2.6.6.

Two de-hazing algorithms are available: the first one is based on the HTM (Haze Thickness Map) [56], the second employs the HOT (Haze Optimized Transform) [106]. The first method can be submitted from a GUI (graphical user interface) or as a batch job and performs the de-hazing on the original digital number (DN) data. This is an optional pre-processing step to ATCOR. An atmospheric correction can be performed as an independent next step to obtain surface reflectance data. The second method performs a de-hazing embedded in ATCOR, so it is always combined with the atmospheric correction. It is available in the GUI and batch modes.

2.6.2 Haze removal with HTM

This method automatically detects and removes haze and cirrus in medium and high spatial resolution multispectral images. The dark-object subtraction algorithm is further developed to calculate a haze thickness map (HTM). The haze thickness is computed for each spectral band excluding very bright object, because these can be misinterpreted as hazy areas. The haze thickness for these bright object pixels is appoximated by a spatial interpolation. The first step is the search for dark pixels using a small local nonoverlapping window box (w=3 x 3 pixels) for the calculation of the

haze thickness map (HTM). For this purpopse a blue spectral channel is employed, because it is most sensitive to haze. If no blue band exists, the green band is taken. The next step calculates an additional HTM map with a moderately large window size (e.g. w= 21 x 21 pixels). It is used to label haze and haze-free regions by thresholding this HTM map. The third step calculates the correlation of the band-specific HTM(λ) maps, and re-scales these maps in the inteval (1,0.1) for $\lambda = (\lambda_{blue}, 2.2\mu m)$. More details can be found in the reference papers [56, 57].

2.6.3 Haze removal with HOT

The second haze removal algorithm (HOT = Haze Optimized Transform) runs fully automatic. It is a combination of the improved methods [67], [106] and consists of five major steps :

1. Masking of clear and hazy areas with the tasseled cap haze transformation [18].

$$TC = x_1 * BLUE + x_2 * RED \tag{2.88}$$

   where BLUE, RED, x_1, and x_2 are the blue band, red band, and weighting coefficients, respectively. The clear area pixels are taken as those pixels where TC is less than the mean value of TC.

2. Calculation of the regression between the blue and red band for clear areas ("clear line" slope angle α), see figure 2.18. If no blue band exists, but a green spectral band, then the green band is used as a substitute.

3. Haze areas are orthogonal to the "clear line", i.e., a haze optimized transform (HOT) can be defined as (Zhang et al. 2002):

$$HOT = BLUE * sin\alpha - RED * cos\alpha \tag{2.89}$$

4. Calculation of the histogram of HOT for the haze areas.

5. For bands below 800 nm the histograms are calculated for each HOT level j. The haze signal Δ to be subtracted is computed as the DN corresponding to HOT(level j) minus the DN corresponding to the 2% lower histogram threshold of the HOT(haze areas). The de-hazed new digital number is (see figure 2.18):

$$DN(new) = DN - \Delta \tag{2.90}$$

So the haze removal is performed before the surface reflectance calculation. Two options are available: the use of a large area haze mask (eq. 2.91), which is superior in most cases, or a compact smaller area haze mask (eq. 2.92).

$$HOT > mean(HOT) - 0.5 * stdev(HOT) \tag{2.91}$$

$$HOT > mean(HOT) \tag{2.92}$$

In addition, the user can select between haze removal of "thin / medium haze" or "thin to moderately thick haze", the last option is superior in most cases.

The algorithm only works for land pixels, so the near infrared band (NIR) is used to exclude water pixels. The current implementation provides a mask for haze-over-land (see the '*_out_hcw.bsq'

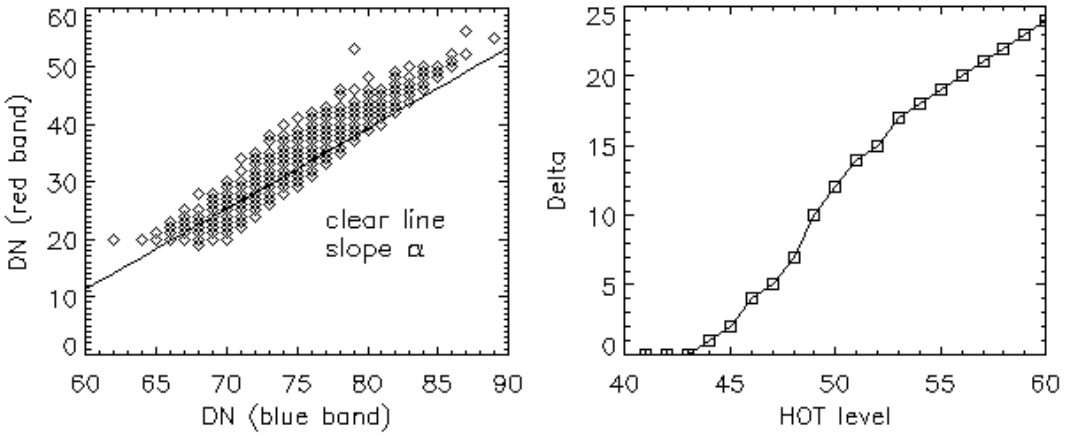

Figure 2.18: *Haze removal method. Left: regression between red and blue band for clear areas. Right: calculation of Delta=Δ as a function of the HOT haze level (example Landsat TM band 1).*

file). The haze-over-water mask is treated in the next section.

Figure 2.19 shows an example of a subset of an Ikonos scene of Dresden where the haze removal algorithm was applied. More images with the results of the haze removal method are shown on ATCOR's web page, http://www.rese.ch .

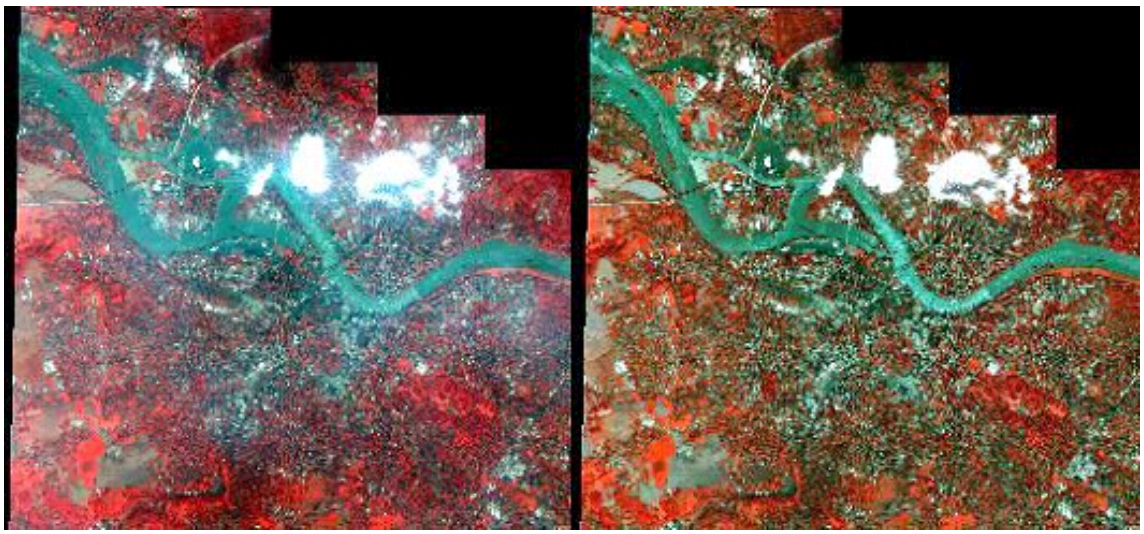

Figure 2.19: *Subset of Ikonos image of Dresden, 18 August 2002. ©Space Imaging Europe 2002. Left: original scene, right: after haze removal. Color coding: RGB=4/2/1 (NIR/Green/Blue bands)*

2.6.4 Haze or sun glint removal over water

The haze removal over water uses a near infrared (NIR) band to estimate the spatial distribution of haze. The principal method is described in [48]. We use a modified version of this approach without an interactive definition of haze polygons. First, the water pixels are masked either using spectral

criteria or taking an external water map. If the scene is named *"scene1.bsq"* the external map must be named *"scene1_water_map.bsq"*, a 1-channel 8-bit/pixel or 16-bit/pixel file where water is coded with an arbitrary positive number. The external map is automatically taken if it is placed in the same folder as the scene. The second step is the definition of clear water pixels using the apparent reflectance in the NIR band. Pixels are labeled as clear if

$$\rho^*(NIR) < T_1(clear) \qquad clear\ pixels \tag{2.93}$$

The default value is $T_1(clear) = 0.04$ (i.e. 4%). The value is one of the editable preference parameters (see [78]). Thin haze over water is defined as:

$$T_1(clear) \leq \rho^*(NIR) \leq 0.06 \qquad thin\ haze \tag{2.94}$$

Medium haze over water is defined as:

$$0.06 < \rho^*(NIR) \leq T_2(haze) \qquad medium\ haze \tag{2.95}$$

The default value is $T_2(haze) = 0.12$ (i.e. 12%). This value is also one of the editable preference parameters. The third step is a linear regression between haze pixels in the NIR band and each other (reflective) band. The regression is iterated with only those pixels deviating less than half a standard deviation from the average. If α_j and β_j denote offset and slope of the regression line, respectively, the de-hazed pixel for each channel j can be calculated as

$$DN(corrected, j) = DN(original, j) - (\alpha_j + \beta_j DN_{NIR} - DN(clear, j)) \tag{2.96}$$

where $DN(clear, j)$ is the average of all clear water pixels in channel j. The same technique is also employed to remove sun glint. The main problem is the specification of the clear water threshold. If the threshold is too low, clear water pixels are included in the haze mask, if it is set too high haze or sun glint pixels will be included in the clear pixel class. There is no unique solution, because sandy bottoms over shallow water can have a similar spectral reflectance behavior as haze, so the clear water threshold is scene-dependent. In addition, the upper threshold defining haze (or sun glint) might be scene-dependent. However, the default values usually provide good results and a solid basis for a possible iteration of these two parameters.
Figure 2.20 presents an example of haze removal over water with the two default values of $T_1(clear) = 0.04$ and $T_2(haze) = 0.12$. The de-hazing over water is successful to a large extent, however, some artifacts appear close to the land border (image center) where haze pixels over water are classified as land or cloud. This is due to a simple spectral classification of the land / water mask, an external water map would lead to better results.

2.6.5 Cirrus removal

On the first glance, images contaminated by cirrus appear similar to hazy scenes discussed in the previous section. However, haze usually occurs in the lower troposphere (0-3 km) while cirrus clouds exist in the upper troposphere and lower stratosphere (8 - 16 km). The effect of boundary layer haze can be observed in the visible region, but seldom in longer wavelength channels > 850 nm. However, cirrus also affects the NIR and SWIR spectral regions. Thin cirrus clouds are difficult to detect with broad-band multispectral satellite sensors in the atmospheric window regions, especially over land, because land scenes are spatially inhomogeneous and this type of cloud is partially transparent. On the other hand, water vapor dominates in the lower troposphere and usually 90% or more of the atmospheric water vapor column is located in the 0 - 5 km altitude layer. Therefore,

Figure 2.20: *Haze removal over water, ALOS-AVNIR2 true color image, northern Germany, 16 April 2007. Left: part of original scene, right: after haze removal.*

if a narrow spectral band is selected in a spectral region of very strong water vapor absorption, e.g., around 1.38 μm or 1.88 μm, the ground reflected signal will be totally absorbed, but the scattered cirrus signal will be received at a satellite sensor or a sensor in a high-altitude aircraft (e.g., 20 km AVIRIS scenes).

So a narrow channel at 1.38 μm is able to detect cirrus clouds, and if a correlation of the cirrus signal at this wavelength and other wavelengths in the VNIR and SWIR region can be found, then the cirrus contribution can be removed from the radiance signal to obtain a cirrus-corrected scene. The basic ideas of cirrus correction were presented in several papers ([25], [26], [28], [81]). The algorithm differs for water and land pixels. For water, a scatterplot of the 1.38 μm versus the 1.24 μm channel is used, for land the band-correlation is determined from a scatterplot of the 1.38 μm versus a red channel (around 0.66 μm). To obtain a high sensitivity, only vegetation pixels are taken because they have a low reflectance in the red spectral region, so the cirrus contribution is easily traced. The scatterplot is computed in terms of the apparent (TOA or at-sensor) reflectance of $\rho_{1.38}$ versus ρ_{red} where the apparent reflectance is defined as:

$$\rho^* = \frac{\pi L}{E_s \; cos\theta_s} \tag{2.97}$$

where L is the recorded radiance signal, E_s the extraterrestrial solar irradiance for the selected band, and θ_s is the solar zenith angle. Following [25] the method can be described by the following set of equations:

$$\rho^*(\lambda) = \rho_c(\lambda) \; + \; \frac{T_c(\lambda) \; \rho(\lambda)}{1 \; - s_c(\lambda) \; \rho(\lambda)} \tag{2.98}$$

Here, ρ_c is the reflectance of the cirrus cloud, T_c the two-way transmittance (direct plus diffuse) through the cloud, ρ the reflectance of the *"virtual"* surface (land or water surface including all effects of molecular and aerosol scattering below the cirrus), and s_c is the cloud base reflectance of upward radiation. Eq. 2.98 can be simplified, because of $s_c\ \rho << 1$, yielding

$$\rho^*(\lambda) = \rho_c(\lambda)\ +\ T_c(\lambda)\ \rho(\lambda) \tag{2.99}$$

With the assumption that the cirrus reflectance $\rho_c(\lambda)$ is linearly related to the cirrus reflectance at 1.38 μm in the 0.4 - 1.0 μm spectrum (small variation of single scattering properties of ice crystals, and single scattering albedo close to 1) we obtain

$$\rho^*(\lambda) = \rho_c(1.38\mu m)\ /\ \gamma\ /\ \gamma \qquad 0.4 < \lambda < 1.0\ \mu m \tag{2.100}$$

where γ is an empirical parameter derived from the scene scatterplot of $\rho_{1.38}$ versus ρ_{red} (land) or $\rho_{1.24}$ (water). It depends on the scene content, cirrus cloud height, and solar and viewing angles. Fig. 2.21 shows an example of such a scatterplot. The red line is the left-side boundary of data points that are not influenced by ground surface reflection, i.e. cirrus-contaminated pixels are clustered around this line, and its slope represents the correlation coefficient γ (the blue line represents the first of several iterations). In the SWIR region, the single scattering albedo of ice crystals is much smaller than 1 and depends on the effective particle size. Equation 2.100 is then applied by reducing γ by the factor 2, to avoid an overcorrection of the cirrus effect, see reference [81]. Substituting eq. 2.100 into eq. 2.99 yields

$$T_c(\lambda)\ \rho(\lambda) = \rho^*(\lambda)\ -\ \rho_c(1.38\mu m)\ /\ \gamma \tag{2.101}$$

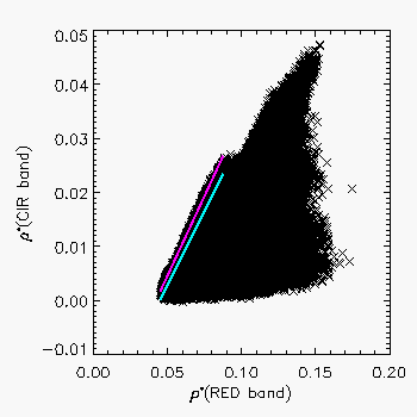

Figure 2.21: *Scatterplot of apparent reflectance of cirrus (1.38 µm) band versus red band.*

Neglecting the cirrus transmittance T_c (i.e., setting $T_c = 1$), we obtain the *"cirrus path radiance corrected"* apparent reflectance image (index 'cc'):

$$\rho^*_{cc}(\lambda) = \rho^*(\lambda)\ -\ \rho_c(1.38\mu m)\ /\ \gamma \tag{2.102}$$

As the cirrus is almost on top of the atmosphere we have $\rho_c(1.38\mu m) = \rho^*_c(1.38\mu m)$ and the apparent cirrus reflectance can be calculated with eq. 2.97.

Note

The calculation of gamma with the scatterplot of the TOA reflectance of the red/cirrus bands

is the standard method. The drawback is that the slope is not always well defined. Therefore, a numerically more stable method is used: the value of γ is calculated iteratively in the typical range (0.6 to 1.0) with an increment of 0.05. We define a cirrus class with $\rho_c^*(1.38) > 0.02$ (or $\rho_c^*(1.38) > 0.014$ if less than 10,000 pixels in this class), and a non-cirrus class with $\rho_c^*(1.38) < 0.008$, or $\rho_c^*(1.38) < 0.010$ or $\rho_c^*(1.38) < 0.011$ if not enough pixels. Then the mean value of the DN of 3 bands (around 440, 480, 550 nm) is computed for the cirrus-free areas $DN_{free}(i)$, i=1, 2, 3. It is also computed for the areas in the cirrus class as a function of γ_j, i.e. after cirrus removal $DN_{decirrus}(\gamma_j, i)$ with equation (2.102). Finally, the value of γ_j is selected which minimizes the difference $\Delta(\gamma_j)$:

$$\Delta(\gamma_j) = Min \{ \sum_{i=1}^{3} \mid DN_{free}(i) - DN_{decirrus}(\gamma_j, i) \mid \} \tag{2.103}$$

Cirrus removal is conducted as the first step during atmospheric correction, followed by the aerosol and water vapor retrievals. If the average water vapor column W of a scene is less than some threshold (default W=0.6 cm) then the cirrus removal algorithm is switched off, to avoid a misinterpretation of bright surfaces as cirrus in the 1.38 μm channel. Normally, atmospheric water vapor completely absorbs surface features in the 1.38 μm channel, but the channel might become partly transparent to surface features for very low water vapor values. This water vapor threshold can be set by the user.

The file *'xxx_out_hcw.bsq'* (haze, cloud, water) corresponding to a scene *'xxx.bsq'* contains three relative levels of cirrus optical thickness (thin, medium, and high). The corresponding thresholds are arbitrarily set depending on the statistics (mean, standard deviation) of the apparent reflectance $\rho_c^*(1.38\mu m)$ map. The file *'xxx_out_hcw.bsq'* is intended as a visual aid or quicklook, therefore, the cirrus level maps of different scenes cannot be compared quantitatively. As an example, a certain scene setting could be:

- thin cirrus thickness, color coded as light yellow, with $0.010 < \rho^*(cirrus) \leq 0.015$,
- medium thickness, color coded as darker yellow, with $0.015 < \rho^*(cirrus) \leq 0.025$,
- high thickness, color coded as bright yellow, with $\rho^*(cirrus) > 0.025$ (reflectance units).

In addition to the 1.38 μm cirrus channel, another channel (index w1) around 1.24 μm (or as a substitute a NIR channel from the 800 to 900 nm region) is employed with a ratio criterion to define cirrus pixels:

$$\rho^*(cirrus)/\rho^*(w1) > T(cir) \tag{2.104}$$

Reference [27] proposes a threshold of T(cir) = 0.3 to distinguish tropospheric aerosols due to dust storms from cirrus clouds. However, in the absence of dust storms, this threshold is too high and predicted no cirrus in a number of test scenes containing a lot of cirrus clouds. Therefore, we use much lower values of T(cir) ranging from 0.01 (for water vapor columns W > 1 cm) to T(cir)=0.15 (for W < 0.5 cm). So with these thresholds, tropospheric aerosols might be misclassified as cirrus in situations with dust storms, but this is a necessary trade-off. In any case, those cloud areas are excluded from the map of pixels employed for the aerosol retrieval, which is the main purpose.

The cirrus and (boundary layer) haze removal options are exclusive, i.e., only one of them can be selected per run.

2.6.6 De-shadowing with matched filter

Remotely sensed optical imagery of the Earth's surface is often contaminated with cloud and cloud shadow areas. Surface information under cloud covered regions cannot be retrieved with optical sensors, because the signal contains no radiation component being reflected from the ground. In shadow areas, however, the ground-reflected solar radiance is always a small non-zero signal, because the total radiation signal at the sensor contains a direct (beam) and a diffuse (reflected skylight) component. Even if the direct solar beam is completely blocked in shadow regions, the reflected diffuse flux will remain, see Figure (2.22). Therefore, an estimate of the fraction of direct solar irradiance for a fully or partially shadowed pixel can be the basis of a compensation process called de-shadowing or shadow removal. The method can be applied to shadow areas cast by clouds or buildings.

This section describes a de-shadowing method based on the matched filter approach, which is complementary to the scene-based method described in section 2.1.2.

The proposed de-shadowing technique works for multispectral and hyperspectral imagery over land acquired by satellite / airborne sensors. The method requires a channel in the visible and at least one spectral band in the near-infrared (0.8-1 μm) region, but performs much better if bands in the short-wave infrared region (around 1.6 and 2.2 μm) are available as well. The algorithm consists of these major components: (i) the calculation of the covariance matrix and zero-reflectance matched filter vector, (ii) the derivation of the unscaled and scaled shadow function, (iii) a histogram thresholding of the unscaled shadow function to define the core shadow areas, (iv) a region growing to include the surroundings of the core shadow areas for a smooth shadow/clear transition, and (v) the de-shadowing of the pixels in the final shadow mask. Details are published in [73].

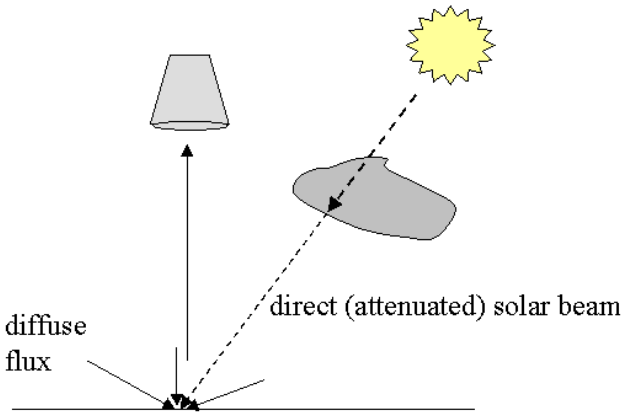

Figure 2.22: *Sketch of a cloud shadow geometry.*

The method starts with a calculation of the surface reflectance image cube $\rho_i = \rho(\lambda_i)$, where three spectral bands around $\lambda_i = 0.85$, 1.6, and 2.2 μm are selected. These bands from the near and shortwave infrared region are very sensitive to cloud shadow effects, because the direct part of the downwelling solar radiation flux at the ground level is typically 80% or more of the total downwelling flux. Channels in the blue-to-red region (0.4-0.7 μm) are not used for the detection of shadow regions because they receive a much larger diffuse radiation component, making them less

sensitive to partial shadow effects. Instead, visible channels serve to define a potential cloud mask.

The surface reflectance is first computed with the assumption of full solar illumination, i.e., the global flux on the ground consists of the direct (E_{dir}) and diffuse (E_{dif}) component. If DN denotes the digital number of a pixel, L_P the path radiance, and τ the atmospheric transmittance (ground-to-sensor) the surface reflectance can be obtained as:

$$\rho_i(x,y) = \frac{\pi(d^2\{c_0(i) + c_1(i)DN_i(x,y)\} - L_{p,i})}{\tau_i\{E_{dir,i} + E_{dif,i}\}} \tag{2.105}$$

Here, d is the Earth-Sun distance at the image acquisition time in astronomical units, c_0 and c_1 are the radiometric calibration coefficients (offset and slope) to convert the digital number into the corresponding at-sensor radiance L, i.e., $L = c_0 + c_1 DN$, and i is the channel index.

The proposed de-shadowing algorithm consists of a sequence of eight processing steps as sketched in Fig. 2.23. It starts with the atmospheric correction. The next step is the masking of water bodies and cloud areas with simple spectral criteria as detailed below. Water pixels have to be excluded as far as possible to avoid their assignment as shadow pixels.
Step 3 calculates the covariance matrix $C(\rho)$ where ρ is the surface reflectance vector comprising only the non-water and non-cloud pixels. For each pixel, this vector holds the reflectance values in the 3 selected channels (around 0.85, 1.6, 2.2 μm). The matched filter is a vector tuned to a certain target reflectance spectrum ρ_t to be detected [2] :

$$V_{mf} = \frac{C^{-1}(\rho_t - \bar{\rho})}{(\rho_t - \bar{\rho})^T C^{-1}(\rho_t - \bar{\rho})} \tag{2.106}$$

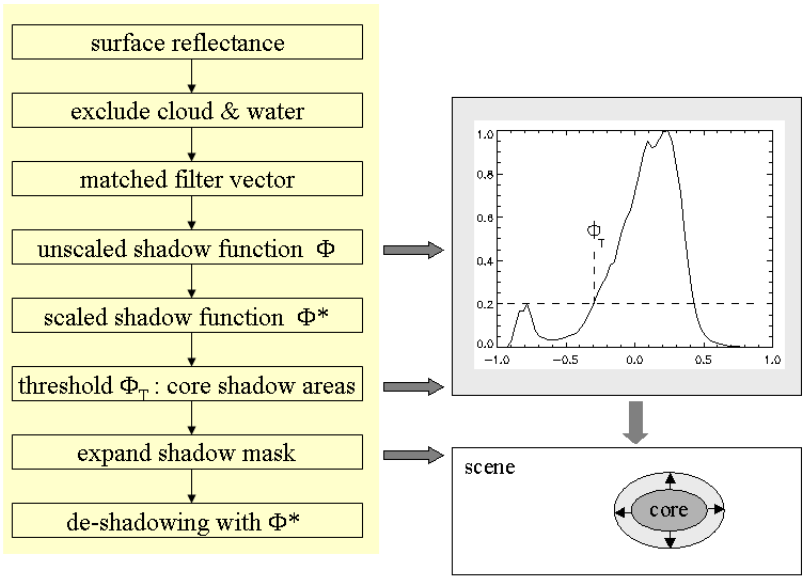

Figure 2.23: *Flow chart of processing steps during de-shadowing.*

Here, $\bar{\rho}$ is the scene-average spectrum, without the water/cloud pixels. Selecting $\rho_t = 0$ for a shadow target yields a special simplified form of the matched filter, where the 'sh' index symbolizes shadow:

$$V_{sh} = -\frac{C^{-1}\bar{\rho}}{\bar{\rho}^T C^{-1}\bar{\rho}} \tag{2.107}$$

The shadow matched filter vector is then applied to the non-water/non-cloud part of the scene and yields the still un-normalized values ϕ that are a relative measure of the fractional direct illumination, also called *unscaled shadow function* here:

$$\Phi(x,y) = V_{sh}^T(\rho(x,y) - \bar{\rho}) \tag{2.108}$$

The matched filter calculates a minimum RMS shadow target abundance for the entire (non-water/non-cloud) scene. Therefore, the values of Φ are positive and negative numbers. The arbitrary, image-depending range of Φ has to be rescaled to the physical range from 0 to 1, where 0 indicates no direct illumination (full shadow), and 1 means full direct illumination. The histogram of Φ is used to rescale the image data. Fig. 2.24 shows a schematic sketch of such a histogram with a smaller peak (at Φ_2) representing the shadow pixels and the main peak (at Φ_{max}) representing the majority of the fully illuminated areas. The statistical assumption is used that full direct solar illumination is already obtained for pixels with $\Phi(x,y) = \Phi_{max}$. Then the values Φ are linearly mapped from the unscaled (Φ_{min}, Φ_{max}) interval onto the physically scaled (0,1) interval, where the *scaled shadow function* is named Φ^*:

$$\Phi^* = \frac{\Phi - \Phi_{min}}{\Phi_{max} - \Phi_{min}} \qquad if \quad \Phi \leq \Phi_{max} \tag{2.109}$$

$$\Phi = 1 \qquad if \quad \Phi > \Phi_{max} \tag{2.110}$$

The smallest value of the scaled shadow function is $\Phi^*_{min} = 0$, which means no direct illumination. However, to avoid overcorrection and to cope with scenes containing merely partial shadow areas, it is advisable to set Φ^*_{min} at a small positive value. This value of Φ^*_{min}, i.e., the minimum fractional direct illumination (deepest shadow in a scene, typically ranging between 0.05 and 0.10) is scene-dependent, see the detailed discussion below.

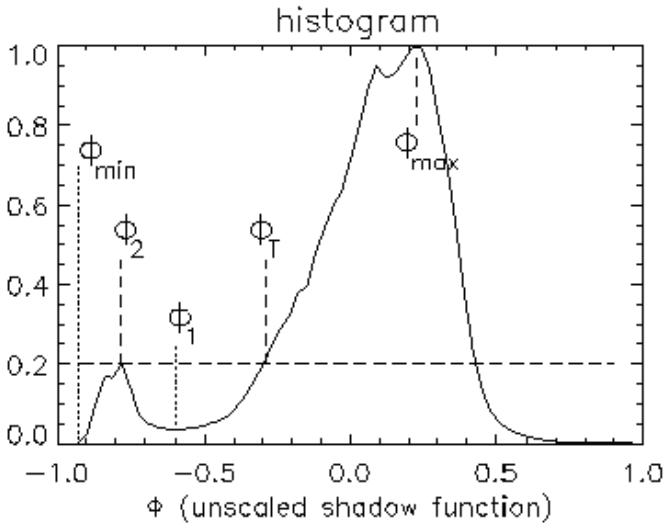

Figure 2.24: *Normalized histogram of unscaled shadow function.*

In principle, the de-shadowing could now be performed with the physically scaled function Φ^*, which represents the fraction of the direct illumination for each pixel in the ρ vector, i.e., the complete scene without cloud and water pixels. However, since the matched filter is not a perfect shadow transformation, it is much better to restrict its application to the potential, most-likely

shadow areas. This is an important processing step to reduce the number of mis-classifications or false-alarms. If omitted it will cause strange 'shadow' pixels scattered all over the image. An example can be found in the central part of Fig. 2.25 where the standard shadow map contains a lot of artifact shadow areas.

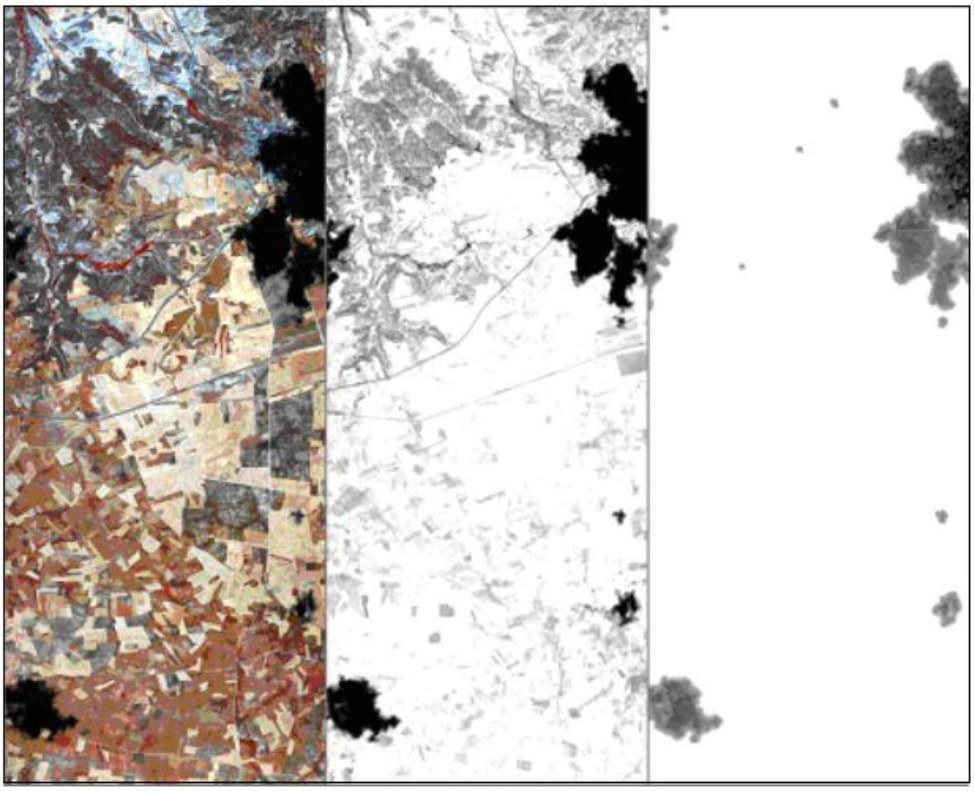

Figure 2.25: *Cloud shadow maps of a HyMap scene.*
Left: surface reflectance image of HyMap at Chinchon, Spain, 12 July 2003. Colour coding: RGB=878, 646, 462 nm channels. Center: standard shadow map showing a lot of artifact shadow areas (grey patches) which do not appear with the core shadow approach (right part). Right: improved cloud shadow map derived from core shadow regions.

Therefore, the proposed method tries to find the core shadow areas in a scene, and subsequently expands the core regions to obtain the final mask that includes a smooth shadow/clear transition. The physically scaled shadow function Φ^* is then applied only to the pixels in the final mask.

The histogram of the unscaled shadow function Φ can be employed to separate regions of low values of Φ from the moderate-to-high values, compare Fig. 2.24. A threshold Φ_T can be set in the vicinity of the local histogram minimum (Φ_1) and the core shadow mask is defined by those pixels with $\Phi(x, y) < \Phi_T$. The details of the choice of Φ_T are discussed below. As always with thresholding, some arbitrariness is involved in the final selection.
Once the core shadow mask has been defined, it is expanded to include the surrounding shadow / clear transition zone of 100 m width. De-shadowing with the scaled shadow function Φ^* is then exclusively applied to the pixels in this final mask. This means the direct solar flux (E_{dir} term in

eq. 2.105) has to be multiplied with $\Phi^*(x,y)$:

$$\rho_i(x,y) = \frac{\pi(d^2\{c_0(i) + c_1(i)DN_i(x,y)\} - L_{p,i})}{\tau_i\{E_{dir,i}\Phi^*(x,y) + E_{dif,i}\}} \tag{2.111}$$

In equations (2.105, 2.111) the aerosol optical thickness or visibility required for the atmospheric terms (path radiance, transmittance, direct and diffuse flux) can be derived from the image provided the necessary bands in the visible and shortwave infrared region exist and the scene contains dark reference areas [43]. Otherwise, the user has to specify an estimated visibility. The second important atmospheric parameter is the water vapour column. For instruments with bands in the atmospheric water vapour regions this information can be derived from the image data [88], otherwise an estimate has to be provided by the user. In summary, three channels (around 0.85, 1.6, and 2.2 μm) are used to define a matched filter vector with three elements per pixel. For each image pixel the surface reflectance in these three channels and the scene-average reflectance of these channels are calculated to obtain the unscaled shadow function, and finally the scaled shadow function. The same shadow function is employed to de-shadow the imagery not only in the initial three channels but for all channels of the sensor (eq. 2.111).

Details of the method:

One of the most important parameters is the available number of spectral channels during the covariance matrix and matched filter part of the algorithm. The minimum requirement is a band in the near-infrared region (0.8 - 1.0 μm). The performance usually increases significantly if two additional bands (at 1.6 μm and at 2.2 μm) are available, i.e., a Landsat TM type of multispectral sensor. Even for hyperspectral imagery these three bands (around 0.85, 1.6, 2.2 μm) are sufficient for the matched filter calculation. The usage of a hundred bands would not be helpful, but only cause numerical problems during the inversion of the covariance matrix (eq. 2.107).
Spectral channels from the visible region are merely employed for the masking of cloud regions, not for the matched filter part, because water, vegetation, dark soils, and shadowed pixels all range within a few percent reflectance. In addition, the visible region is not very sensitive to partial shadow effects, because of its larger fraction of diffuse radiation component as compared to wavelengths longer than 0.8 μm.

The distinction of water bodies from cloud shadow areas may be difficult or impossible if it is based merely on spectral reflectance shape and amplitude information. Water bodies should be excluded as far as possible to improve the performance of the de-shadowing algorithm. Currently, water and cloud pixels are masked with the spectral criteria defined in the file 'preference_parameters.dat', see [78] e.g.,

$$\rho(0.85\mu m) \leq 5\% \quad and \quad \rho(1.6\mu m) \leq 3\% \quad (water) \tag{2.112}$$

$$\rho(0.48\mu m) \geq 25\% \quad and \quad \rho(1.6\mu m) \geq 25\% \quad (cloud) \tag{2.113}$$

If no channel in the blue region is available, a channel in the green (0.5-0.6 μm) or red part of the spectrum (0.6-0.68 μm) could be used as a substitute. Both criteria do not uniquely define the corresponding class. The water criteria allow some margin for turbid water in the NIR region. The more restrictive criterion $\rho(0.85\ \mu m) < 3\%$ would perform better for clear water bodies. However, it would fail for moderately turbid or muddy waters. Other common water classification criteria such as average reflectance over all bands $\bar{\rho} \leq 3\%$ or $\rho(0.4-0.6\mu m) < 6\%$ may also fail. So one has to compromise and tolerate a certain amount of misclassification for a fully automatic algorithm.

The scaled shadow map $\Phi^*(x, y)$ is written to an output file.

The histogram of the unscaled shadow function Φ (Fig. 2.24) typically has a main peak at Φ_{max}, a smaller secondary peak (at Φ_2) due to shadow pixels, and a local minimum (at Φ_1). The secondary peak can be determined by level-slicing the normalized histogram. We arbitrarily define a threshold Φ_T as the intersection of this slice line at the level of $h(\Phi_2)$ with the normalized histogram h(Φ) for $\Phi_1 < \Phi < \Phi_{max}$. The approach with a main peak and a smaller secondary peak is restricted to cases where the percentage of shadow pixels in the scene is less than about 25%. This applies to the fully automatic processing mode. If the secondary peak at Φ_2 is not clearly defined numerically, i.e., no local minimum found at Φ_1, or histogram difference $h(\Phi_2) - h(\Phi_1) < 0.03$, then Φ_T is defined as the intersection of the slice level 0.10 with h(Φ) for $\Phi < \Phi_{max}$. More flexibility exists in the interactive mode, see [78].

Masking of the core shadow areas with $\Phi < \Phi_T$ (Fig. 2.24) is critical like any thresholding process: a large threshold could potentially include non-shadow areas, a low threshold could miss shadow areas. The current automatic algorithm has the three user-selectable options of a small, medium, or large core shadow mask corresponding to thresholds set at $\Phi_T - 0.1, \Phi_T$, and $\Phi_T + 0.1$, respectively. The default value for the fully automatic algorithm is the medium-size mask. In addition, an interactive mode for adjusting the threshold is also available.

A second tunable parameter is the minimum fractional direct illumination Φ^*_{min}, also called depth of shadow. Theoretically, it can be zero, i.e., a completely shadowed pixel receiving only diffuse solar illumination. However, a too low estimate close to zero will boost the surface reflectance, especially for channels in the 1.5 - 2.5 μm region (eq. 2.111), since the diffuse solar radiation term E_{dif} is very small. Therefore, small positive values of Φ^*_{min} are recommended. The range of Φ^*_{min} is typically from 0.05 to 0.1, with the default set at $\Phi^*_{min} = 0.08$. The third tunable parameter is Φ_{max} providing the range of stretching of the unscaled shadow function into the scaled function. The default of Φ_{max} is the location of the maximum of the histogram of Φ, but it could be set at a greater value if the corrected image is too dark in the expanded shadow regions, which indicates the histogram maximum does not represent fully illuminated areas.

The advantage of the presented method is its fast processing performance, because it relies exclusively on spectral calculations and avoids time-consuming geometric cloud/shadow pattern considerations. The drawback is that useful geometric information is neglected.

In some cases it is useful to have the de-shadowed digital number (DN) image in addition to the surface reflectance product. This facilitates a comparison with the originally recorded DN imagery. The conversion from reflectance to the corresponding at-sensor radiance is performed with eq. (2.1). Then eq. (2.6) is employed to compute the de-shadowed DN image for channel k:

$$DN(k) = \frac{L(k) - c_0(k)}{c_1(k)} \tag{2.114}$$

Figure 2.26 shows an example of de-shadowing. More images with the results of the de-shadowing method can be found on ATCOR's web page, http://www.rese.ch or http://www.op.dlr.de/atcor .

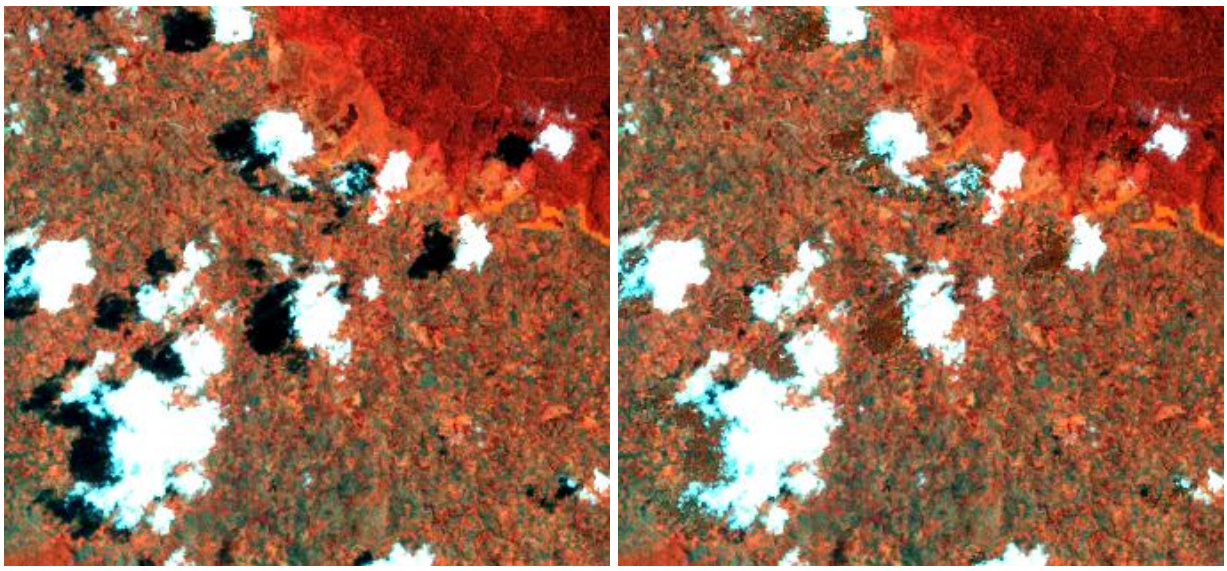

Figure 2.26: *De-shadowing of a Landsat-7 ETM+ scene.*
Subset of a Landsat-7 ETM+ scene from Kenia, 10 April 2001. Color coding: RGB = bands 4/2/1 (830, 560, 480 nm). Left: original scene, right: after de-shadowing.

2.7 Correction of BRDF effects

The bottom of atmosphere reflectance as retrieved after standard ATCOR atmospheric compensation is highly variable due to the influence of the bidirectional reflectance distribution function (BRDF, [62]). The observed reflectance value may deviate from the average spectral albedo by up to 30%, specifically for vegetation and man made surfaces.

ATCOR offers three different methods of correcting BRDF effects: The first method is mainly intended for flat terrain and normalizes the off-nadir reflectance values to the corresponding nadir values.

The second method is exclusively dedicated to rugged terrain imagery and corrects for BRDF effects due to the variability of the solar incidence angle. The reflectance values of areas with low local solar elevation angles, i.e.. large local solar zenith angles, are often overcorrected by the assumption of isotropically reflecting surfaces. The method reduces these high, overcorrected values depending on the illumination and/or viewing angles.

The third method corrects the observation BRDF effects by fitting a physical BRDF model to a number of images and surface cover classes in order to obtain a generic BRDF correction function. This function is used to calculate a per-pixel anisotropy factor which corrects for the deviation from an averaged spectral albedo.

In some cases of rugged terrain imagery it is useful to apply both, incidence and observation angle correction methods of BRDF correction.

2.7.1 Nadir normalization method

A simple algorithm was implemented as part of the ATCOR package to normalize the scan angle dependent brightness values to the nadir value. It is recommended to apply the method to imagery

after atmospheric correction, i.e., to reflectance data. However, if only the across-track illumination gradients shall be removed without any further atmospheric correction, the algorithm can also be applied to radiance (DN) data. In this case, the brightness gradient may be caused by a combination of surface BRDF and atmospheric BRDF (left/right asymmetry in path radiance).

The algorithm is intended for large field-of view sensors (minimum FOV=20^o). It computes the column means with a certain angular sampling interval (1^o or 3^o). The input image may be geocoded, or not. If it is not geocoded the total field-of-view FOV corresponds to the number n of across-track image pixels per line. If geocoded, the scan angle for each pixel must be provided in a separate file ("_sca"). It contains the scan angle in degree scaled with a factor of 100, and coded with 16 bits per pixel. This definition is taken from the airborne ATCOR/PARGE interface (Schläpfer and Richter 2002). Scan angles on the right hand side with respect to flight heading are defined as negative, those on the left side as positive, e.g., a value of -2930 represents a scan angle of 29.3°on the right side.

The nadir region is defined here as the $\pm 3^o$ scan angle range. Usually, a 3^o angular sampling interval, from $+3^o$ to +FOV/2 on the left side and -3^o to -FOV/2 on the right side, is adequate, except for geometries close to the hot spot geometry. In the latter case, a 1^o sampling interval can be selected.

If $\bar{b}_{nadir}$ denotes the averaged brightness value for the nadir region, i.e., reflectance or radiance, then the nadir normalized brightness value of a pixel with column number j is calculated as:

$$b_{norm}(j) = b(j)\frac{\bar{b}_{nadir}}{f_2(j)} \tag{2.115}$$

where the function f_2 is obtained with three processing steps:

- The first step is the averaging over each interval (3°or 1°). It yields a function f_1 with m+1 grid points for the m off-nadir intervals plus the nadir interval.
- Two cases are distinguished now: if the image is not geocoded, an interpolation from function $f_1(m+1)$ to a function $f_2(ncols)$ is performed where ncols is the number of column pixels of the image. If the image is geocoded, an interpolation from the 3° grid to the 1° grid is performed (no hot spot case).
- The third step is a filter with a moving average window applied to the f_2 function. The following cases are distinguished: if the image is not geocoded the window is 9 pixels (without hot spot) and 3 pixels (with hot spot option). If the image is geocoded, the moving window extends over a 5° angular interval (no hot spot) and over a 3° interval (with hot spot option).

Figure 2.27 shows part of a HyMap image (acquired 3 June 1999, Barrax, Spain, 12:09 UTC) containing the hot spot geometry. The solar azimuth was 181^o and the sensor scan line azimuth was 179^o, almost exactly pointing into the solar azimuth. The left image shows HyMap band 30 at 868 nm after atmospheric correction. The right image is the result after nadir normalization with a 1^o sampling interval. In this example, the column means were calculated globally, i.e. surface cover independent. The algorithm also contains an option to compute the column means separately for 4 surface covers. It can currently only be selected if the input imagery is reflectance data and not geocoded. The processing time is much larger than for the global, cover-independent method. The four surface classes are:

- bright vegetation (ratio vegetation index NIR/RED > 10);

- medium/dark vegetation (6 < ratio vegetation index < 10);
- dry vegetation or mixed vegetation/soil (3 < vegetation index < 6);
- soil (vegetation index < 3).

The reflectance of off-nadir water pixels (criterion: near infrared reflectance < 5 %) is not modified.

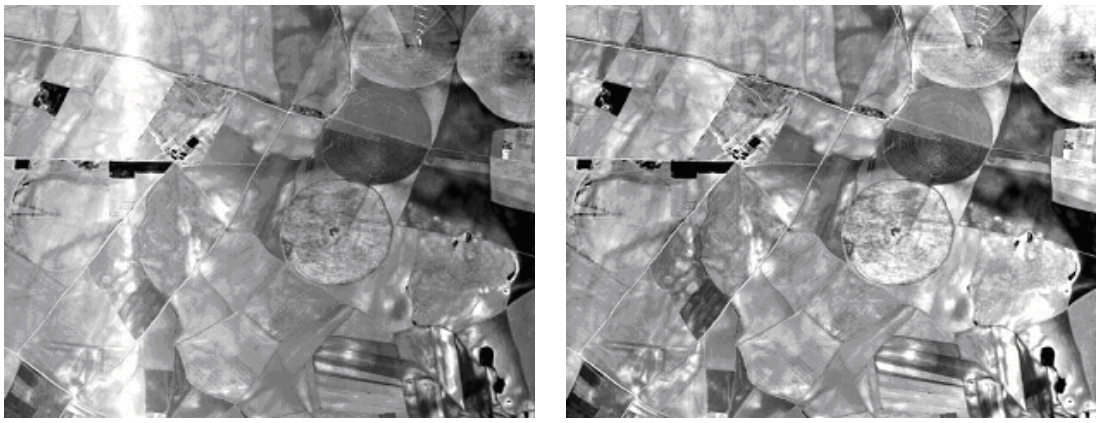

Figure 2.27: *Nadir normalization of an image with hot-spot geometry.*
Left: reflectance image without BRDF correction. Right: after empirical BRDF correction.

2.7.2 Empirical incidence BRDF correction in rugged terrain

For many surface covers the reflectance increases with increasing solar zenith and / or viewing angle [50]. Scenes in mountainous regions often exihibit a large variation of terrain slopes, and thus bidirectional brightness variations for a certain surface cover, e.g., meadow or forest. This behavior cannot adequately be eliminated with the Lambertian assumption of equation (2.15). This equation leads to overcorrected reflectance values in faintly illuminated areas (having small values of $cos\beta$).

Background

Several approaches have been pursuit to solve this problem in the past :

- an empirical coefficient C is calculated based on a regression of brightness values and the local ilumination angle derived from the DEM. The coefficient depends on scene content and wavelength ([100], [64]).
- the sun-canopy-sensor (SCS) geometry is employed in forested terrain instead of the solely terrain-based geometry [31].
- the SCS method is coupled with the C-correction [98].

These approaches produced good results on sample scenes with uniform cover types presented in the above papers. When applying the methods to a wider range of areas, some of the practical problems are:

- mountainous scenes often contain a number of different covers, e.g., deciduous forest, coniferous forest, mixed forest, shrubs, meadow, rocks, etc.

- the computation of the C coefficients for different surface covers would require a pre - classification.
- the correlation obtained for the C coefficients is often less than 0.7, yielding unreliable results with this method.

These remarks are supported by reference [64]. These authors applied different correction approaches to a TM scene containing different cover types and noted that there is no optimum method for all cover types. A drawback of the Minnaert and empirical C-methods is that they do do not distinguish between the direct and diffuse solar illumination as opposed to the physically based approach of ATCOR. Nevertheless, the latter approach also cannot avoid problems in faintly illuminated areas.

Correction method

The methods described in the above section are supplemented by an empirical method with three adjustable parameters (β_T, b, and g) as explained below. This approach was tested on different rugged terrain scenes with vegetated and arid landscapes and usually yields satisfactory results. It reduces overcorrected reflectance values starting at a threshold local solar zenith angle β_T greater than the scene's solar zenith angle Θ_s. Equation (2.116) defines the implemented basic geometric correction function which depends on the local solar incidence angle (solar illumination β_i) and the threshold angle β_T. The exponent b (= 1/3, 1/2, 3/4, or 1) is the second parameter and can be selected by the user. Some guidelines on the choice of b are are discussed below. The third adjustable parameter is the lower bound g of the correction function, see Figure 2.28.

$$G = \{cos\beta_i / cos\beta_T\}^b \qquad \geq g \tag{2.116}$$

The threshold illumination angle β_T should have some margin to the solar zenith angle to retain the original natural variation of pixels with illumination angles close to the solar zenith angle. The threshold angle can be specified by the user and the following empirical rules are recommended:

- $\beta_T = \theta_s + 20°$ if $\theta_s < 45°$
- If $45 \leq \theta_s \leq 55°$ then $\beta_T = \theta_s + 15°$
- If $\theta_s > 55°$ then $\beta_T = \theta_s + 10°$

These rules are automatically applied if $\beta_T = 0$, e.g., during batch processing.

The geometric function G needs a lower bound g to prevent a too strong reduction of reflectance values. Values of G greater than 1 are set to 1, and values less than the boundary g are reset to g. This means the processing works in the geometric regime from β_T to 90°and the updated reflectance is:

$$\rho_g = \rho_L G, \tag{2.117}$$

where ρ_L is the isotropic (Lambert) value.

Figure 2.28 shows a graphical presentation of equation (2.116). The left part displays the function G for different values of the exponent b. For b=1 the decrease with β_i is strong with a constant gradient. For smaller values of b the decrease with β_i is moderate initially, but the gradient increases with larger β_i. Currently, different functions G for soil/sand and vegetation can be selected in ATCOR (see [78]. The function G for soil / sand is applied with a wavelength - independent exponent b. After testing a large number of vegetated mountainous scenes two vegetation modes were finally selected because of their good performance:

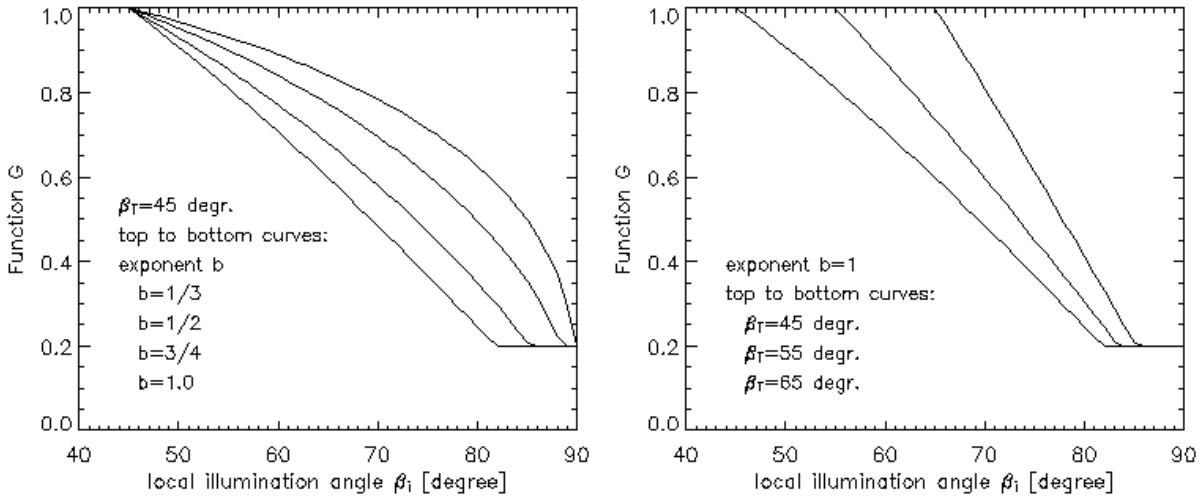

Figure 2.28: *Geometric functions for empirical BRDF correction. Left: Functions G eq. (2.116) for different values of the exponent b. Right: Functions G of eq. (2.116) for b=1 and different start values of β_T. The lower cut-off value is g=0.2.*

1. b=0.75 for channels with $\lambda < 720$ nm and b=0.33 for $\lambda > 720$ nm ("weak" correction),
2. b=0.75 ($\lambda < 720$ nm) and b=1 ($\lambda > 720$ nm), ("strong" correction).

In most of the tested cases, the first mode was appropriate. A simple criterion (vegetation index $\rho_{850nm}/\rho_{660nm} > 3$) is used to distinguish soil/sand and vegetation.
The right part of Figure 2.28 shows the effect of shifting the threshold illumination angle β_T. For larger values of β_T the decline of function G starts later with a larger gradient, and the lower bound g is met at slightly higher values of β_i. In most cases, g=0.2 to 0.25 is adequate, in extreme cases of overcorrection g=0.1 should be applied.

Practical considerations

The angle β_T can actually be calculated from the imagery as demonstrated by the following example. When processing the scene with ATCOR the map of local solar zenith angles is stored in a separate file "*ilu". If the output file after atmospheric / topographic correction contains bright overcorrected areas this file should be linked to the "*ilu" file using any available standard image processing software. The "*ilu" file contains the illumination map β_i scaled as byte data:

$$ilu = 100 * cos\beta_i \tag{2.118}$$

$$\beta_i = arccos(ilu/100) \tag{2.119}$$

Let us assume an example:

A pixel in a dark area of the "*ilu" image has the value ilu=32, i.e., $\beta_i = 71°$. The overcorrected reflectance value be $\rho_L = 80\%$ and this value shall be reduced to 40%, a value typical for the flat-terrain neighborhood. Then the threshold angle has to be specified such that $cos\beta_i/cos\beta_T = 0.5$ (with exponent b=1 in equation (2.116), in this case $\beta_T = 50°$. So, if the desired reflectance

reduction factor is G then the required threshold angle can be calculated from eq. (2.116 with b=1):

$$\beta_T = arccos(\frac{cos\beta}{G}) = arccos\frac{ilu}{100G} \tag{2.120}$$

In many cases a separate treatment of BRDF effects for soil/rock and vegetation provides better results. For this purpose, several modes of BRDF correction are available, see [78].

Reference [77] contains a comparison of different topographic correction methods for several Landsat-TM, ETM+, and SPOT-5 scenes from different areas. The proposed empirical ATCOR approach performed best in most of these cases, but no method ranked first in all cases.

2.7.3 BRDF effect correction (BREFCOR)

A generic BRDF effects correction routine (BREFCOR, [91])) has been included in ATCOR. The idea is to apply a scaling of the volume scattering and the geometric scattering component within a well accepted BRDF model. A fuzzy surface cover index of the complete image image is used for this purpose, which covers all surface types from water to asphalt and concrete, soils, sparse vegetation and dense vegetation.

The Ross-Li-sparce reciprocal BRDF model has been selected as basis for the correction of reflectance anisotropy [35]. This model is mainly developed for vegetation, but we use it in a scaled way for all kind of surfaces. Literature mainly related to MODIS atmospheric correction routines showed the superior performance of this model if compared to others. However, for high spatial resolution instruments also other models may be applicable.

Selected BRDF kernels

The BRDF correction scheme is based on the Ross-Thick Li-Sparse Model (RTLS), potentially enhanced by the Hot-Spot function as proposed by Maignan et al. [55]. For the correction, a formulation of the model for the Bidirectional Reflectance Factor (BRF) is used. The BRF is well suited for correction of the HDRF, as both quantities are defined as 1.0 for a 100% reflecting target at the same observation geometry, and as only the second dimension (observation direction) relative variation of the BRF is used for the correction. The generic RTLS-equation of the BRF for each pixel and spectral band is given as:

$$\rho_{BRF} = \rho_{iso} + f_{vol}K_{vol} + f_{geo}K_{geo}, \tag{2.121}$$

where ρ_{iso} is the isotropic reflectance defined at nadir for both illumination and observation angle. The kernel factors f_{vol} and f_{geo} are weighting coefficients for the respective kernels. They depend on the ground coverage BRDF, whereas the kernels are fixed functions which define a fully bi-directional reflectance property. The kernels have been selected according to the findings of BRDF literature [101]. For the volume scattering, the Ross-Thick kernel is modified to include the hot-spot extension by Maignan, i.e.:

$$K_{vol} = \frac{4}{3\pi}\frac{1}{\cos\theta_i + \cos\theta_r}\left[\left(\frac{\pi}{2} - \zeta\right)\cos\zeta + \sin\zeta\right] - \frac{1}{3}, \tag{2.122}$$

where $\zeta = \arccos(\cos\theta_i\cos\theta_r + \sin\theta_i\sin\theta_r\cos\phi)$.

The angle θ_i is the incident solar zenith angle, θ_r is the observation zenith angle, and ϕ is the relative azimuth angle $\phi = \phi_i - \phi_r$ (i.e., the difference between incidence and observation azimuth). The extension of this volumetric kernel by Maignan is given as:

$$K_{vol} = \left(K_{vol} + \frac{1}{3}\right)\left(1 + \frac{1}{1 + \zeta/1.5^o}\right). \tag{2.123}$$

The reciprocal Li-Sparse kernel is used for the geometric part. It is defined as:

$$K_{geo} = \frac{1}{\pi}(t - \sin t \cos t)\left(\frac{1}{\cos\theta_i} + \frac{1}{\cos\theta_r}\right) \quad - \left(\frac{1}{\cos\theta_i} + \frac{1}{\cos\theta_r}\right) + \frac{1 + \cos\zeta}{2\cos\theta_i \cos\theta_r}, \tag{2.124}$$

where
$t = \arccos\left(\frac{\sqrt{\tan^2\theta_i + \tan^2\theta_r - 2\tan\theta_i \tan\theta_r \cos\phi + (\tan\theta_i \tan\theta_r \cos\phi)^2}}{\frac{1}{\cos\theta_i} + \frac{1}{\cos\theta_r}}\right)$.

2.7.4 BRDF cover index

A continuous BRDF cover index (BCI) function is used for characterization of the surface. It is calculated on the HDRF of four standard bands: blue at 460nm, green at 550nm, red at 670 nm, and near infrared at 840nm. This reduced selection of spectral bands makes the index applicable for most current optical remote sensing systems. The BCI function characterizes the image based on intrinsic BRDF properties from strong forward scatterers (water) to neutral targets (asphalt) to backward scatterers (soils and vegetation types). The index implementation is using the normalized difference vegetation index (NDVI) as a first input for vegetation density quantification due to its known relation to the leave area index (LAI), which has a significant influence on the BRDF [54].

The NDVI is increased in Equation (2.125) by a value of up to 0.5 using the fact that dense agricultural vegetation shows higher green reflectance than dense forests; i.e., the NDVI is increased by C_{forest} for dense forests having a green reflectance in a range below 7%. In a further step, the BCI is decreased for soils by C_{soils} using the effect that soils show a relatively low blue at-sensor radiance. A last adaption C_{water} is made for water such that clear water areas are always set to a minimum value:

$$BCI = (NDVI + C_{forest} - C_{soils} - C_{water}) > -1.2. \tag{2.125}$$

Note: the ">" -sign denotes a maximum operator between the left and the right side of the term.

The three correction functions in Equation 2.125 are given as follows, first for forests using the absolute HDRF value in the green ρ_{green}:

$$C_{forest} = \frac{0.5}{0.04 \cdot 0.2} \cdot \left([0.07 - \rho_{green}]_{0.00}^{0.04}\right) \cdot \left([NDVI - 0.55]_{0.00}^{0.20}\right). \tag{2.126}$$

The upper and lower values at the square brackets indicate a truncation at these values. The upper values could be adapted for better representation of biome types. For surface covers having a BCI below 0.1 (i.e., mostly soils), a reduction factor is found from the relation between blue and red HDRF as:

$$C_{soils} = \frac{\rho_{blue}}{\rho_{red}}\left([1 - 10 \cdot (NDVI + C_{forest})]_{0.00}^{1.00}\right). \tag{2.127}$$

This factor accounts for the variability of non-vegetated areas in the visible. Finally, a summand to account for water is added, starting with $BCI_{soil} = NDVI + C_{forest} - C_{soils}$. It takes into

account the relatively higher reflectance of water in the green spectral band in relation to the blue for discrimination to other surface targets such as shadows and dark asphalt:

$$C_{water} = \left(\left(\frac{\rho_{green}}{2\rho_{blue}} - 0.8 \right) > 0 \right) \cdot \left(-3 \left((BCI_{soil} + 0.5) < 0 \right) \right). \tag{2.128}$$

The range of the final BCI function is defined between values of -1.20 and 1.50. The BCI-index calculated in each image pixel can then be used for BRDF model calibration and subsequently for image correction.

Model calibration

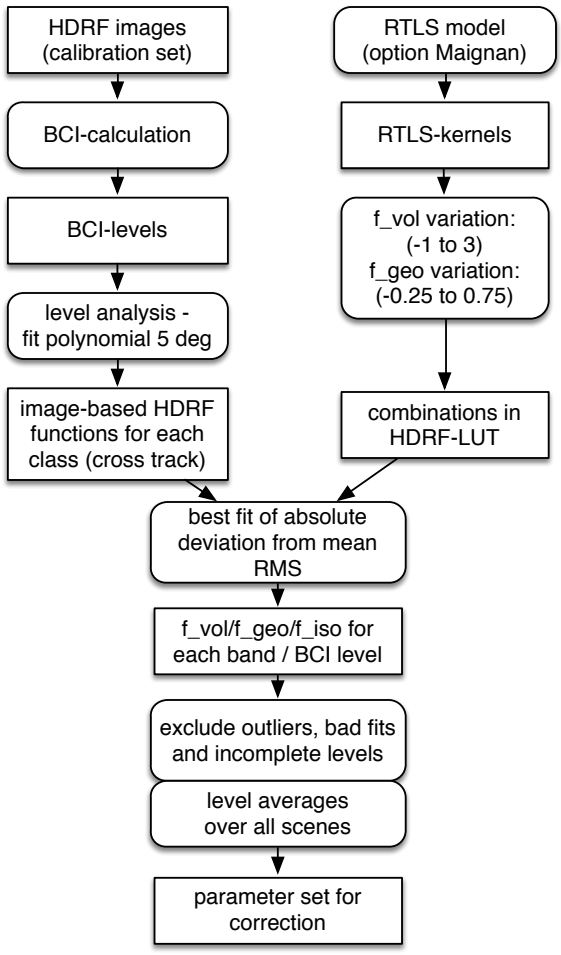

Figure 2.29: *BRDF model calibration scheme*

For the calibration of the model, the BCI is divided into a number of 4-6 discrete classes. The evaluation has shown that increasing the number of classes often leads to worse fitting results and less stable BRDF correction whereas keeping the number of classes small is more stable. A second outcome was that it is hardly feasible to define generic class limits for any kind of data acquisition and sensor. The calibration follows the scheme shown in Figure 2.29.

Differences in limits can be attributed to the fact that the higher resolution images allows for a more accurate and statistically more relevant calibration of the model whereas for lower resolution, the number of classes should be reduced. The classes can be denominated as: water, artificial materials, soils, sparse vegetation, grassland, and forests. For each of the classes, the optimum kernel weights are calculated and stored for each image of a campaign. All weights are then averaged while bad fitting classes (with relative errors greater than 10%) are excluded from averaging. No BRDF correction is applied for classes without any fitting parameters (i.e. if less than 3 bands out of 4 within the class could be calibrated). The averaged model is stored for later application to the imagery.

Image correction

Finally, the derived BRDF model calibration data are to be applied to the image data. For application on the imagery, the BCI has to be calculated from each image and is used to get a continuous correction function.

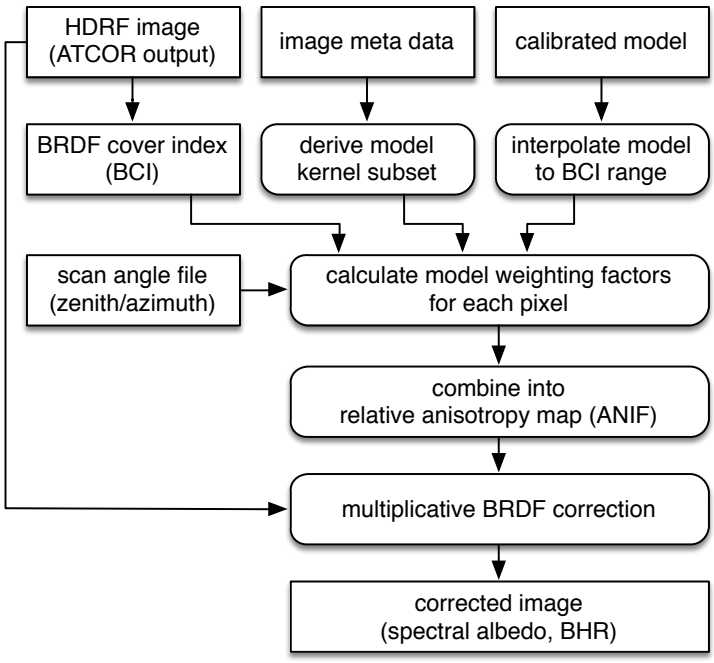

Figure 2.30: *Image correction scheme.*

The image processing procedure is following the below steps (compare Figure 2.30):

- calculate the BCI from image,
- calculate the scene-specific angular kernels subsets,
- interpolate the calibration data from BCI levels to a continuous BRDF model,
- calculate an anisotropy map by scaling the kernels using the BCI, the scan angles (observation zenith and azimuth angle), and the interpolated BRDF model, and

- apply the anisotropy map on a per-pixel basis.

The anisotropy factor is derived as relation of the directional model for each pixel to the same model averaged over all angles (i.e., to a good approximation of the spectral albedo BHR).

$$ANIF = \frac{\rho_{iso} + f_{geo}K_{geo,\theta_i,\theta_r,\phi} + f_{vol}K_{vol,\theta_i,\theta_r,\phi}}{\rho_{iso} + f_{geo}\overline{K_{geo}} + f_{vol}\overline{K_{vol}}} \approx \frac{\rho_{BRF}}{\rho_{BHR}}. \quad (2.129)$$

The bihemispherical reflectance is described by the two hemispherical averages $\overline{K_{geo}}$ and $\overline{K_{vol}}$ weighted by the respective factors and added to the constant isotropic reflectance ρ_{iso}. Alternatively, the anisotropy with respect to nadir BRF would be an option as done in earlier BRDF research [85]. This option is currently not supported in BREFCOR, as the BHR is the more generic spectral albedo definition for surface object characterization.
The corrected bihemispherical reflectance is finally calculated as $\rho_{BHR} = \frac{\rho_{HDRF}}{ANIF}$, where ρ_{HDRF} is the bottom of atmosphere (directional) reflectance after standard ATCOR-4 atmospheric compensation, as described above.

Sample result

The BREFCOR correction is most appropriate for wide FOV sensors, i.e., with FOV values larger than approx. 20 degrees, typically found for airborne imagery. For satellite imagery, the BREFCOR correction is typically applied for mosaicking a number of images, acquired in the same area at varying illumination and sensor observation angle conditions. A sample result for RapidEye imagery is displayed in Figure 2.31. The image is a chessboard of a false-color composite of two scenes acquired with a relative observation angle difference, where the first had a observation zenith of 1.4° and a solar zenith of 18.7°, whereas the second scene was 8 days later and had angles of 14.7° and 14.3°, respectively. The lower image is the correction result based on the calibrated Ross-Li-sparse BRDF model. Some of the BRDF effects can be removed by this method as long as the image statistics are sufficient. However, not all effects can be fully removed - this could also be attributed to changing atmospheric conditions between the two dates.

2.8 Summary of atmospheric correction steps

Although the case of a flat terrain could be treated as a special case of a rugged terrain with the same elevation everywhere this is not an efficient solution, because the rugged terrain algorithm runs 3 to 4 times slower than the flat terrain code. Therefore, the coding is done in separate modules as discussed below.

2.8.1 Algorithm for flat terrain

The complete sequence of processing for sensors with water vapor bands and a short wave IR band (1.6 or 2.2 μm region) consists of the following steps:

- masking of haze, cloud, water, and clear pixels
- haze removal or cirrus removal
- de-shadowing

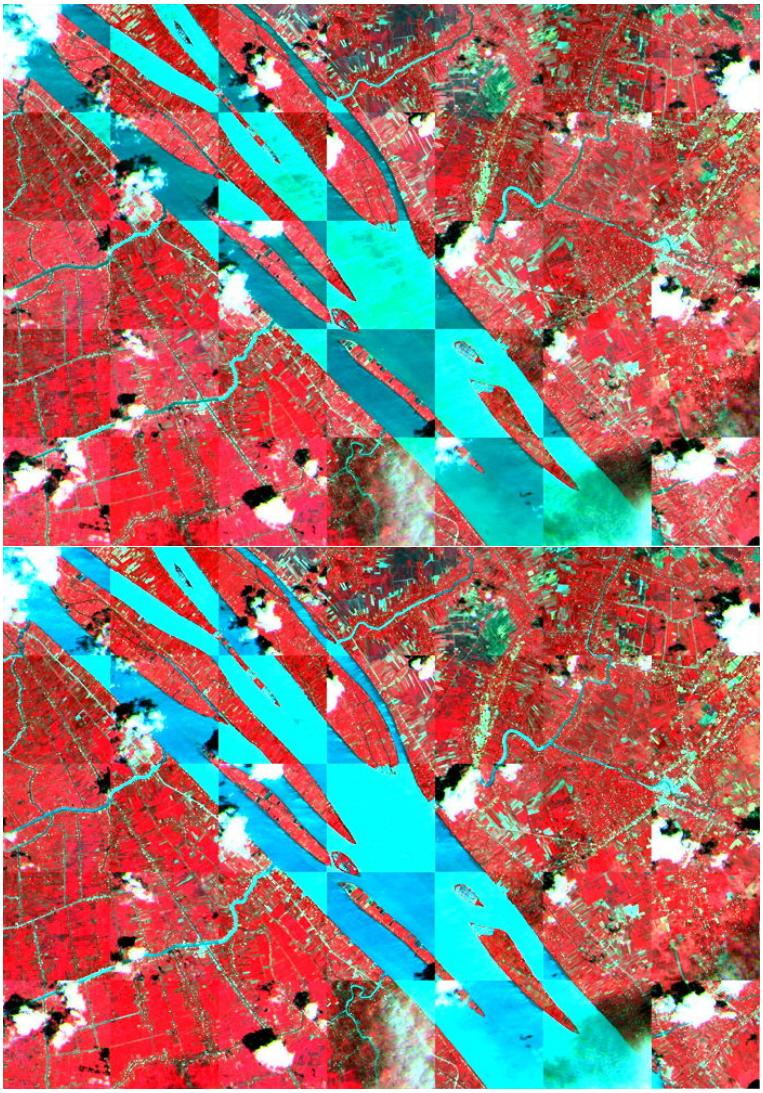

Figure 2.31: *BREFCOR mosaic correction: Top: uncorrected, Bottom: corrected (RapidEye chessboard image mosaic, (c) DLR).*

- masking of reference pixels
- calculation of visibility, visibility index, and aerosol optical thickness for reference pixels. For an efficient faster processing, the float visibility range 5 - 190 km is converted into a discrete integer visibility index (vi), ranging from 0 - 182, where the vi increment 1 corresponds to an aerosol optical thickness increment (at 550 nm) of 0.002. The lowest vi = 0 corresponds to visibility = 190 km, and vi = 182 to visibility = 5 km. The visibility / visibility index of the non-reference pixels can be defined as the average of the reference pixels or or a spatial (triangular) interpolation can be employed to fill the gaps. Then a moving low pass window with a box size of 3 $km \times 3$ km (or the minimum of ncols/2 and nlines/2, ncols=image columns, nlines=lines) is applied to smooth sensor noise and small scale variations of the spectral correlation coefficient of the DDV reference pixels. Finally, the aerosol optical thickness (AOT at 550 nm) is calculated with eq. 2.81. The visibility index and AOT(550nm) maps are stored

as separate files. The visibility calculation based on the reference pixels has to account for the adjacency effect, because reference areas are embedded in non-reference areas, see the sketch below. Since the weighting fraction of reference to non-reference area within the adjacency range is not known for each pixel, the visibility calculation is performed with an average adjacency weighting factor of 0.5 q :

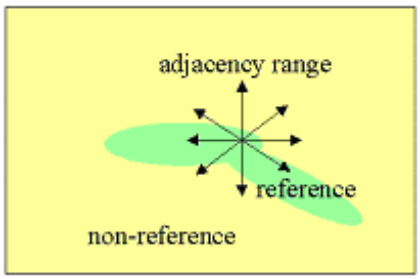

Figure 2.32: *Weighting of q function for reference pixels.*

$$L_{adj.cor} = c_0 + c_1 DN + 0.5q(DN - DN_{av,clear}) \tag{2.130}$$

$$L(VIS) = L_p + \tau \rho_{ref} E_g / \pi = L_{adj.cor} \tag{2.131}$$

Next the visibility is converted into the nearest visibility index vi (range 0-182), compare Fig. 2.15, to store the visibility index map as byte data. Spatial interpolation is performed to fill the gaps for non-reference pixels or the average vi value can be taken to close the gaps. A moving average window of 3 km × 3 km is employed to reduce the influence of noise. The cloud / building shadow map is stored separately ("fshd.bsq" file, containing the fraction of direct solar irradiance per pixel, scaled with the factor 1000). The scaled value 1000 indicates full solar irradiance, smaller values a corresponding fractional value.

- an update of the path radiance in the blue-to-red spectral region is performed, if required, provided a blue spectral band exists.
- water vapor retrieval using the previously calculated visibility map. If the scene contains no reference areas the user has to specify a constant visibility that enters the water vapor calculation.
- reflectance spectrum retrieval with pixel-based water vapor and visibility map. Iterations for adjacency effect and spherical albedo are included. For the adjacency correction, the reflectance of cloud pixels is replaced with the scene average reflectance to avoid an overcorrection of the adjacency effect.
- temperature / emissivity retrieval if thermal bands exist.

2.8.2 Algorithm for rugged terrain

The algorithm for rugged terrain basically consists of the same processing step as in the flat terrain, but every step has to take into account some or all DEM information:

- During the calculation of the visibility index map the DEM information (elevation, slope, aspect, skyview factor) is taken into account.

- The retrieval of the water vapor map has to include the terrain elevation.
- The empirical BRDF correction is based on the local illumination map (local solar zenith angle) derived from the slope, aspect and shadow channels.
- The retrieval of the spectral reflectance cube consists of the steps
  1. three iterations for terrain reflectance,
  2. empirical BRDF correction depending on illumination map, if enabled,
  3. adjacency correction, including proper treatment of cloud areas,
  4. spherical albedo correction.
- The retrieval of surface temperature and emissivity includes the maps of visibility index, water vapor (if water vapor bands exist), elevation, and scan angle. No slope/aspect correction is performed in the thermal region.

2.9 Accuracy of the method

There is not a single figure that can be given to summarize the accuracy for all situations, because the radiometric accuracy of the method depends on several factors: the calibration accuracy of the sensor, the quality of geometric co-registration of the spectral bands, the algorithm for ortho-rectification relying on auxiliary information such as attitude and GPS/DGPS, the accuracy of the radiative transfer code (MODTRAN 5), the correct choice of atmospheric input parameters, the terrain type (flat or rugged), and the surface cover.

Solar region:
In the solar region (wavelength < 2.5 μm), assuming a flat terrain, and avoiding the specular and backscattering regions, an accuracy of the retrieved surface reflectance of $\pm 2\%$ (for reflectance $< 10\%$) and $\pm 4\%$ reflectance units (for reflectance $> 40\%$) can be achieved [72]. For rugged terrain, the most important parameter is an adequate spatial resolution of the DEM or DSM (digital surface model) and the exact ortho-rectification of the imagery. It would be desirable to have a DEM of a quarter of the sensor's spatial resolution or at least the resolution of the sensor's footprint which is seldom available [69]. Even in the latter case, errors in the matching of imagery and DEM can lead to large relative reflectance errors exceeding 100% for critical geometries (principal plane, e.g. a mountain ridge with half a pixel offset between imagery and DEM [69]). Thus, the quality of the required DEM will limit the final accuracy of the geo-atmospheric image product in many cases. For a flat terrain and larger off-nadir view angles, BRDF effects may have to be accounted for, and the appropriate surface-cover dependent BRDF model will influence the accuracy.

Thermal region:
In the thermal wavelength region beyond 8 μm, the surface temperature retrieval additionally depends on the correct choice of the surface emissivity. In the ATCOR model the emissivity in one thermal band is based on a classification of the reflective bands if the sensor collects co-registered reflective and thermal band data. Depending on the surface cover classification (vegetation, soil, sand, asphalt, water, etc.), a typical emissivity value is assigned to each class [84]. If the deviation of the true surface emissivity to the assumed emissivity is less than 0.02 (a typical error margin), then the temperatures will be accurate to about 1-1.5 K. A rule of thumb is a surface temperature error of about 0.5-0.8 K per 0.01 emissivity error if the surface temperature is much higher than

the boundary layer air temperature [95]. An accuracy of 1-2 K can be achieved if the emissivity estimate is better than 2% [15].

Bibliography

[1] Ackerman, S. A., Strabala, K. I., Menzel, W. P., Frey, R. A., Moeller, C. C., and Gumley, L. E., "Discriminating clear sky from clouds with MODIS", *J. Geophys. Res.*, Vol. 103, D24, 32,141-32,157 (1998).

[2] Adler-Golden, S.M., Matthew, M. W., Anderson, G. P., Felde, G. W., and Gardner, J. A., 2002, An algorithm for de-shadowing spectral imagery, *Proc. 11th JPL Airborne Earth Science Workshop, 5-8 March 2002*, JPL-Publication 03-04, Pasadena, U.S.A.

[3] Asner, G., "Canopy shadow in IKONOS satellite observations of tropical forests and savannas." Remote Sensing of Environment, 87(4), 521533. doi:10.1016/j.rse.2003.08.006 (2003).

[4] Asrar, G., Fuchs, M., Kanemasu, E. T., and Hatfield, J. L., "Estimating absorbed photosynthetically active radiation and leaf area index from spectral reflectance in wheat", *Agron. J.*, Vol. 76, 300-306, (1984).

[5] Asrar, G. "Theory and Applications of Optical Remote Sensing", J. Wiley, New York, (1989).

[6] Baret, F., and Guyot, G., 1991, "Potentials and limits of vegetation indices for LAI and APAR assessment", *Remote Sensing of Environment*, Vol. 35, 161-173, (1991).

[7] Berk, A., Bernstein, L.S., Anderson, G.P., Acharya, P.K., Robertson, D.C., Chetwynd, J.H., and Adler-Golden, S.M., "MODTRAN cloud and multiple scattering upgrades with application to AVIRIS", *Remote Sensing of Environment*, Vol. 65, 367-375 (1998).

[8] Berk, A., Anderson, G.P., Acharya, P.K., and Shettle, E.P., "MODTRAN5.2.0.0 User's Manual", Spectral Sciences Inc., Burlington MA, Air Force Research Laboratory, Hanscom MA (2008).

[9] Brutsaert, W., "On a derivable formula for long-wave radiation from clear skies", *Water Resources Research*, Vol. 11, 742-744, (1975).

[10] Buettner, K. J. K., and Kern, C. D., "The determination of infrared emissivities of terrestrial surfaces, *Journal of Geophysical Research*, Vol. 70, 1329-1337, (1965).

[11] Carlson, T. N., Capehart, W. J., and Gillies, R. R., "A new look at the simplified method for remote sensing of daily evapotranspiration", *Remote Sensing of Environment*, Vol. 54, 161-167, (1995).

[12] Chander, G., Markham, B. L., and Helder, D. L., "Summary of current radiometric calibration coefficients for Landsat MSS, TM, ETM+, and EO-1 ALI sensors", *Remote Sens. Environm.*, Vol. 113, 893-903 (2009).

[13] Choudhury, B. J., "Synergism of multispectral satellite observation for estimating regional land surface evaporation", *Remote Sensing of Environment*, Vol. 49, 264-274, (1994).

[14] Choudhury, B. J., Ahmed, N. U., Idso, S. B., Reginato, R. J., and Daughtry, C. S. T., "Relations between evaporation coefficients and vegetation indices studied by model simulations", *Remote Sensing of Environment*, Vol. 50, 1-17, (1994).

[15] Coll, C., Caselles, V., Rubio, E., Sospreda, F., and Valor, E., "Temperature and emissivity separation from calibrated data of the Digital Airborne Imaging Spectrometer", Remote Sens. Environm., Vol. 76, 250-259, (2001).

[16] Coll, C., Richter, R., Sobrino, J. A., Nerry, F., Caselles, V., Jimenez, J. C., Labed-Nachbrand, J., Rubio, E., Soria, G., and Valor, E., "A comparison of methods for surface temperature and emissivity estimation", In *Digital Airborne Spectrometer Experiment*, ESA- SP-499 p. 217-223, Nordwijk, Netherlands (2001).

[17] Corripio, J. G., "Vectorial algebra algorithms for calculating terrain parameters from DEMs and the position of the sun for solar radiation modelling in mountainous terrain", Int. J. of Geographical Information Science, Vol. 17, 1-23 (2003).

[18] Crist, E. P., and Cicone, R. C., "A physically-based transformation of Thematic Mapper data - the Tasseled Cap", *IEEE Trans. Geosci. Remote Sensing*, Vol. GE-22, 256-263 (1984).

[19] Dozier, J., Bruno, J., and Downey, P., "A faster solution to the horizon problem", *Computers & Geosciences*, Vol. 7, 145-151 (1981).

[20] Dell'Endice, F., Nieke, J., Schläpfer, D., and Itten, K. I., "Scene-based method for spatial misregistration detection in hyperspectral imagery", *Applied Optics*, Vol. 46, 2803-2816 (2007).

[21] ERSDAC. "ASTER User's Guide, Part II, (Vers. 3.1)", (2001).

[22] Fontenla, J. M., Curdt, W and Haberreiter, M., Harder J., and Tian, H.,"Semiempirical Models of the Solar Atmosphere. III. Set of Non-LTE Models for Far-Ultraviolet/Extreme-Ultraviolet Irradiance Computation *The Astrophysical Journal*, 707:482-502 (2009).

[23] Fontenla, J. M., Harder, J., Livingston, W., Snow, M., and Woods, T., "High-resolution solar spectral irradiance from extreme ultraviolett to far infrared", J. Geophys. Res., Vol. 116, D20108, 31pp., (2011).

[24] Fraser, R. S., Bahethi, O.P., and Al-Abbas, A. H., "The effect of the atmosphere on classification of satellite observations to identify surface features", *Remote Sens. Environm.*, Vol. 6, 229-249 (1977).

[25] Gao, B.-C., Kaufman, Y.J., Han, W., and Wiscombe, W.J., "Correction of thin cirrus path radiances in the 0.4 - 1.9 μm spectral region using the sensitive 1.375 μm cirrus detecting channel", *J. Geophys. Res.*, Vol. 103, D24, 32,169-32,176 (1998).

[26] Gao, B.-C., Yang, P., Han, W., Li, R.-R., and Wiscombe, W.J., "An algorithm using visible and 1.38 μm channels to retrieve cirrus cloud reflectances from aircraft and satellite data", *IEEE Trans. Geosci. Remote Sens.*, Vol. 40, 1659-1668 (2002).

[27] Gao, B.-C., Kaufman, Y. J., Tanre, D., and Li, R. R., "Distinguishing tropospheric aerosols from thin cirrus clouds for improved aerosol retrievals using the ratio of $1.38-\mu m$ and $1.24-\mu m$ channels", *Geophys. Res. Letters*, Vol. 29, No. 18, 1890, 36-1 to 36-4 (2002).

[28] Gao, B.-C., Meyer, K., and Yang, P., "A new concept on remote sensing of cirrus optical depth and effective ice particle size using strong water vapor absorption channels near 1.38 and 1.88 μm", *IEEE Trans. Geosci. Remote Sens.*, Vol. 42, 1891-1899 (2004).

[29] Gillespie, A. R., "Lithologic mapping of silicate rocks using TIMS", *In Proc. TIMS Data User's Workshop*, JPL Publ. 83-38 (Pasadena, CA), pp. 29-44 (1986).

[30] Gillespie, A., et al., "A temperature and emissivity separation algorithm for Advanced Spaceborne Thermal Emission and Reflection Radiometer (ASTER) images", *IEEE Trans. Geosc. Remote Sensing*, Vol. 36, 1113-1126 (1998).

[31] Gu, D., and Gillespie, A., "Topographic normalization of Landsat TM images of forest based on subpixel sun - canopy - sensor geometry", *Remote Sensing of Environment*, Vol. 64, 166-175 (1998).

[32] Guanter, L., Richter, R., and Moreno, J., "Spectral calibration of hyperspectral imagery using atmospheric absorption features", *Applied Optics*, Vol. 45, 2360-2370 (2006).

[33] Guanter, L., Richter, R., and Kaufmann, H., "On the application of the MODTRAN4 atmospheric radiative transfer code to optical remote sensing", *Int. J. Remote Sensing*, Vol. 30, 1407-1424 (2009).

[34] Hay, J. E., and McKay, D. C., "Estimating solar irradiance on inclined surfaces: a review and assessment of methodologies", *Int. J. Solar Energy*, Vol. 3, 203-240 (1985).

[35] Hu B., Lucht W., Li X., and Strahler A.H., Validation of kernel-driven semiempirical models for the surface bidirectional reflectance distribution function of land surfaces, *Remote Sens. Environ.*, vol. 62, no. 3, pp. 201214, 1997.

[36] Huete, A. R., "A soil adjusted vegetation index (SAVI)", *Remote Sensing of Environment*, Vol. 25, 295-309, (1988).

[37] Idso, S. B., and Jackson, R. D., "Thermal radiation from the atmosphere", *J. Geophysical Research*, Vol. 74, 5397-5403, (1969).

[38] Isaacs, R. G., Wang, W-C., Worsham, R. D., and Goldberg, S., "Multiple scattering LOWTRAN and FASCODE models", *Applied Optics*, Vol. 26, 1272-1281, (1987).

[39] Jimenez-Munoz, J. C., and Sobrino, J. A., "Atmospheric water vapour content retrieval from visible and thermal data in the framework of the DAISEX campaign", *Int. J. Remote Sensing*, Vol. 26, 3163-3180 (2005).

[40] Kahle, A. B., et al., "Middle infrared multispectral aircraft scanner data analysis for geological applications", *Applied Optics*, Vol. 19, 2279-2290 (1980).

[41] Kamstrup, N., and Hansen, L. B., "Improved calibration of Landsat-5 TM applicable for high-latitude and dark areas", *Int. J. Remote Sensing*, Vol. 24, 5345-5365 (2003).

[42] Kaufman, Y. J., and Sendra, C., "Algorithm for automatic atmospheric corrections to visible and near-IR satellite imagery", *Int. J. Remote Sensing*, Vol. 9, 1357-1381 (1988).

[43] Kaufman, Y. J., et al. "The MODIS 2.1 μm channel - correlation with visible reflectance for use in remote sensing of aerosol", *IEEE Transactions on Geoscience and Remote Sensing*, Vol. 35, 1286-1298 (1997).

[44] Kleespies, T. J., and McMillin, L. M., "Retrieval of precipitable water from observations in the split window over varying surface temperature", *J. Applied Meteorology*, Vol. 29, 851-862 (1990).

[45] Kobayashi, S., and Sanga-Ngoie, K., "The integrated radiometric correction of optical remote sensing imageries" *Int. J. Remote Sensing*, Vol. 29, 5957-5985 (2008).

[46] Kobayashi, S., and Sanga-Ngoie, K., "A comparative study of radiometric correction methods for optical remote sensing imagery: the IRC vs. other image-based C-correction methods", *Int. J. Remote Sensing*, Vol. 30, 285-314 (2009).

[47] Irish, R. R., Barker, J. L., Goward, S. N., and Arvidson, T., "Characterization of the Landsat-7 ETM+ automated cloud-cover assessment (ACCA) algorithm", *Photogr. Eng. Remote Sens.* Vol. 72, 1179-1188 (2006).

[48] Yi, C. Y., "Haze reduction from the visible bands of Landsat TM and ETM+ images over a shallow water reef environment", *Remote Sens. Environm.*, Vol. 112, 1773-1783 (2008).

[49] Krause, K., "Radiance conversion of QuickBird data", Technical note RS_TN_radiometric_radiance_4002, http://www.digitalglobe.com, Digital Globe, 1900 Pike Road, Longmont, CO 80501, USA (2003).

[50] Kriebel, K. T., "Measured spectral bidirectional reflection properties of four vegetated surfaces", *Applied Optics*, Vol. 17, 253-259 (1978).

[51] Levy, R.C. et al., "Algorithm for remote sensing of troposheric aerosol over dark targets from MODIS: collections 005 and 051, Revision 2; Feb 2009" (2009).

[52] Li. Z. L., et al., "A new appooach for retrieving precipitable water from ATSR2 split-window channel data over land area", *Int. J. Remote Sensing*, Vol. 24, 3163-3180 (2003).

[53] Liang, S., Falla-Adl, H., Kalluri, S., Jaja, J., Kaufman, Y. J., and Townshend, J. R. G., "An operational atmospheric correction algorithm for Landsat Thematic Mapper imagery over the land", *J. Geophys. Res.*, Vol. 102, D14, 17,173-17,186 (1997).

[54] Luo. Y., "Surface bidirectional reflectance and albedo properties derived using a land cover-based approach with Moderate Resolution Imaging Spectroradiometer observations", *J. Geophys. Res.*, vol. 110, no. 1, p. D01106, (2005).

[55] Maignan F., Br¡8e¿on F. M. , and Lacaze R. , "Bidirectional reflectance of Earth targets: evaluation of analytical models using a large set of spaceborne measurements with emphasis on the Hot Spot",

[56] Makarau, A., Richter, R., Müller, R., and Reinartz, P., "Haze detection and removal in remotely sensed multispectral imagery", *IEEE TGRS*, Vol. 52, 5895-5905 (2014).

[57] Makarau, A., Richter, R., Schläpfer, D, and Reinartz, P., "Combined haze and cirrus removal for multispectral imagery", *IEEE GRSL*, Vol. 13, 379-383 (2016).

[58] Mouroulis, P., Green, R. O., and Chrien, T. G., "Design of pushbroom imaging spectrometers for optimum recovery of spectroscopic and spatial information", *Applied Optics*, Vol. 39, 2210-2220 (2000).

[59] Moran, M. S., Clarke, T. R., Inoue, Y., and Vidal, A., "Estimating crop water deficit using the relation between surface-air temperature and spectral vegetation index", *Remote Sensing of Environment*, Vol. 49, 246-263 (1994).

[60] Murray, F. W., "On the computation of saturation vapor pressure", *J. Applied Meteorology*, Vol. 6, 203-204, (1967).

[61] Stamnes, K., Tsay, S. C., Wiscombe, W. J., and Jayaweera, K., "Numerically stable algorithm for discrete-ordinate-method radiative transfer in multiple scattering and emitting layered media", *Applied Optics*, Vol. 27, 2502-2509 (1988).

[62] Nicodemus, F. E., "Reflectance nomenclature and directional reflectance and emissivity", *Applied Optics*, Vol. 9, 1474-1475 (1970).

[63] Parlow, E., "Net radiation of urban areas", Proc. 17th EARSeL Symposium on Future Trends in Remote Sensing, Lyngby, Denmark, 17-19 June 1997, pp. 221-226, Balkema, Rotterdam (1998).

[64] Riano, D., Chuvieco, E., Salas, J., and Aguado, I., "Assessment of different topographic corrections in Landsat-TM data for mapping vegetation types", *IEEE Trans. Geoscience and Remote Sensing*, Vol. 41, 1056-1061 (2003).

[65] Richter, R., "Derivation of temperature and emittance from airborne multispectral thermal infrared scanner data", *Infrared Phys. Technol.*, Vol. 35, 817-826 (1994).

[66] Richter, R., "A spatially adaptive fast atmospheric correction algorithm", *Int. J. Remote Sensing*, Vol. 17, 1201-1214 (1996).

[67] Richter, R., "Atmospheric correction of satellite data with haze removal including a haze/clear transition region", *Computers & Geosciences*, Vol. 22, 675-681 (1996).

[68] Richter, R., "On the in-flight absolute calibration of high spatial resolution spaceborne sensors using small ground targets", *Int. J. Remote Sensing*, Vol. 18, 2827-2833 (1997).

[69] Richter, R., "Correction of satellite imagery over mountainous terrain", *Applied Optics*, Vol. 37, 4004-4015 (1998).

[70] Richter, R., "Bandpass-resampling effects on the retrieval of radiance and surface reflectance", *Applied Optics*, Vol. 39, 5001-5005 (2000).

[71] Richter, R., and Coll, C., "Bandpass-resampling effects for the retrieval of surface emissivity", *Applied Optics*, Vol. 41, 3523-3529 (2002).

[72] Richter, R., and Schläpfer, D., "Geo-atmospheric processing of airborne imaging spectrometry data. Part 2: atmospheric / topographic correction.", *Int. J. Remote Sensing*, Vol. 23, 2631-2649 (2002).

[73] Richter, R., and Müller, A., "De-shadowing of satellite/airborne imagery", *Int. J. Remote Sensing*, Vol. 26, 3137-3148 (2005).

[74] Richter, R., Schläpfer, D., and Müller, A., "An automatic atmospheric correction algorithm for visible/NIR imagery", *Int. J. Remote Sensing*, Vol. 27, 2077-2085 (2006).

[75] Richter, R., Bachmann, M., Dorigo, W., Mueller, A., "Influence of the adjacency effect on ground reflectance measurements", *IEEE Geoscience Remote Sensing Letters*, Vol. 3, 565-569 (2006).

[76] Richter, R., and Schläpfer, D., "Considerations on water vapor and surface reflectance retrievals for a spaceborne imaging spectrometer", *IEEE Trans. Geoscience Remote Sensing*, Vol. 46, 1958-1966 (2008).

[77] Richter, R., Kellenberger, T., and Kaufmann, H., "Comparison of topographic correction methods", *Remote Sensing*, Vol. 1, 184-196 (2009).

[78] Richter, R., and D. Schläpfer, "Atmospheric / topographic correction for satellite imagery: ATCOR-2/3 User Guide", DLR IB 565-01/17, Wessling, Germany (2017).

[79] Richter, R., and D. Schläpfer, "Atmospheric / topographic correction for airborne imagery: ATCOR-4 User Guide", DLR IB 565-02/17, Wessling, Germany (2017).

[80] Richter, R., Schläpfer, D., and Müller, A., "Operational atmospheric correction for imaging spectrometers accounting the smile effect", *IEEE Trans. Geoscience Remote Sensing*, Vol. 49, 1772-1780 (2011).

[81] Richter, R., Wang, X., Bachmann, M., and Schläpfer, D., "Correction of cirrus effects in Sentinel-2 type of imagery", *Int. J. Remote Sensing*, Vol.32, 2931-2941 (2011).

[82] Richter, R., Heege, T., Kiselev, V., and Schläpfer, D., "Correction of ozone influence on TOA radiance", *Int. J. Remote Sensing*, Vol.35, 8044-8056 (2014).

[83] Rodger, A., and Lynch, M. J., "Determining atmospheric column water vapour in the 0.4-2.5 μm spectral region", Proceedings of the AVIRIS Workshop 2001, Pasadena, CA (2001).

[84] Salisbury, J. W., and D'Aria, D. M., "Emissivity of terrestrial materials in the 8-14 μm atmospheric window", *Remote Sensing of Environment*, Vol. 42, 83-106 (1992).

[85] Sandmeier, S.T., and Deering, D. W. , "Structure analysis and classification of boreal forests using airborne hyperspectral BRDF data from ASAS", *Remote Sensing of Environment* vol. 69, no. 3, pp. 281295, 1999.

[86] Santer, R., et al., "SPOT Calibration at the La Crau Test Site (France)", *Remote Sensing of Environment*, Vol. 41, 227-237 (1992).

[87] Santer, R., et al., "A surface reflectance model for aerosol remote sensing over land", *Int. J. Remote Sensing*, Vol. 28, 737-760 (2007)

[88] Schläpfer, D., Borel, C. C., Keller, J., and Itten, K. I., "Atmospheric precorrected differential absorption technique to retrieve columnar water vapor", *Remote Sensing of Environment*, Vol. 65, 353-366 (1998).

[89] Schläpfer, D., and Richter, R., "Geo-atmospheric processing of airborne imaging spectrometry data. Part 1: parametric orthorectification.", *Int. J. Remote Sensing*, Vol. 23, 2609-2630 (2002).

[90] Schläpfer, D. "PARGE, User Guide, Version 3.1", ReSe Applications Schläpfer, Wil, Switzerland, (2011).

[91] Schläpfer, D., Richter R., and Feingersh T., "Operational BRDF Effects Correction for Wide-Field-of-View Optical Scanners (BREFCOR)", *IEEE Trans. Geoscience and Remote Sensing*, vol. 53, no. 4, pp. 18551864, (2014).

[92] Schowengerdt, R. A., "Remote Sensing, Models and Methods for Image Processing", 3rd Edition, Elsevier (Academic Press), (2007).

[93] Shao, Y., Taff, G. N., and Walsh, S. J. , "Shadow detection and building-height estimation using IKONOS data", International Journal of Remote Sensing, 32(22), 69296944. doi:10.1080/01431161.2010.517226 (2011).

[94] Sirguey, P., "Simple correction of multiple reflection effects in rugged terrain", *Int. J. Remote Sensing*, Vol. 30, 1075-1081 (2009).

[95] Slater, P. N., "Remote Sensing, Optics and Optical Systems", Addison-Wesley, London (1980).

[96] Slater, P. N., "Radiometric considerations in remote sensing", *Proc. IEEE*, Vol. 73, 997-1011 (1985).

[97] Slater, P. N., et al., "Reflectance and radiance-based methods for the in-flight absolute calibration of multispectral sensors", *Remote Sensing of Environment*, Vol. 22, 11-37 (1987).

[98] Soenen, S., A., Peddle, D. R.,and Coburn, C. A., "SCS+C: a modified sun - canopy - sensor topographic correction in forested terrain", *IEEE Trans. Geoscience and Remote Sensing*, Vol. 43, 2148-2159 (2005).

[99] Sutherland, R. A., "Broadband and spectral emissivities (2-18 μm) of some natural soils and vegetation, *Journal of Atmospheric and Oceanic Technology*, Vol. 3, 199-202, (1986).

[100] Teillet, P. M., Guindon, B., and Goodenough, D.G., "On the slope-aspect correxion of multispectral scanner data", *Canadian J. Remote Sensing*, Vol. 8, 84-106, (1982).

[101] Wanner W., A. H. Strahler, B. Hu, P. Lewis, J.-P. Muller, X. Li, C. L. B. Schaaf, and M. J. Barnsle, "Global retrieval of bidirectional reflectance and albedo over land from EOS MODIS and MISR data: Theory and algorithm", J. Geophys. Res., vol. 102, no. 14, pp. 17143D17161, (1997).

[102] Wiegand, C. L., Gerbermann, A. H., Gallo, K. P., Blad, B. L., and Dusek, D., "Multisite analyses of spectral-biophysical data for corn", *Remote Sensing of Environment*, Vol. 33, 1-16, (1990).

[103] Wiegand, C. L., Richardson, A. J., Escobar, D. E., and Gerbermann, A. H., "Vegetation indices in crop assessments", *Remote Sensing of Environment*, Vol. 35, 105-119, (1991).

[104] Wolfe, W. L., and Zissis, G. J., "The Infrared Handbook", Office of Naval Research, Washington, DC., (1985).

[105] Young, S. J., Johnson, B. R., and Hackwell, J. A., "An in-scene method for atmospheric compensation of thermal hyperspectral data", *J. Geophys. Research*, Vol. 107, No. D24, 4774-4793 (2002).

[106] Zhang, Y., Guindon, B., and Cihlar, J., "An image transform to characterize and compensate for spatial variations in thin cloud contamination of Landsat images", *Remote Sensing of Environment*, Vol. 82, 173-187 (2002).